Fall 2016

An integrated multibody dynamics computational framework for design optimization of wind turbine drivetrains considering wind load uncertainty

Huaxia Li
University of Iowa

AN INTEGRATED MULTIBODY DYNAMICS COMPUTATIONAL FRAMEWORK FOR DESIGN OPTIMIZATION OF WIND TURBINE DRIVETRAINS CONSIDERING WIND LOAD UNCERTAINTY

by

Huaxia Li

A thesis submitted in partial fulfillment
of the requirements for the Doctor of
Philosophy degree in Mechanical Engineering
in the Graduate College of
The University of Iowa

December 2016

Thesis Supervisors: Associate Professor Hiroyuki Sugiyama
Professor Kyung K. Choi

Graduate College
The University of Iowa
Iowa City, Iowa

CERTIFICATE OF APPROVAL

_____

PH.D. THESIS

_____

This is to certify that the Ph.D. thesis of

Huaxia Li

has been approved by the Examining Committee
for the thesis requirement for the Doctor of Philosophy
degree in Mechanical Engineering at the December 2016 graduation.

Thesis Committee: _____
Hiroyuki Sugiyama, Thesis Supervisor

_____
Kyung K. Choi, Thesis Supervisor

_____
Patrick B. Butler

_____
Pablo M. Carrica

_____
Jia Lu

_____
Shaoping Xiao

ACKNOWLEDGMENTS

The overall study could not have been accomplished and well integrated into this thesis without the supervision from my advisor and co-advisor. I would like to express my gratitude to them for their help during my study. My deepest gratitude goes first to my advisor Professor Hiroyuki Sugiyama, for his rigorous research attitude, constant encouragement and invaluable guidance. He has walked me through all the stages of my Ph.D. research and the thesis writing. I could not have kept pursuing my research without his consistent support. Second, I would like to express my heartfelt gratitude to my co-advisor Professor Kyung K. Choi, who helped me in the field of design optimization and reliability and taught me how to find the best solution to solve problems. His continuous inspiration and illuminating advice helped me a lot during my research. I would like to thank Professor Patrick B. Butler, Professor Pablo M. Carrica, Professor Jia Lu and Professor Shaoping Xiao for serving on my thesis committee.

Special thanks go to Dr. Hyunkyoo Cho in Professor Kyung K. Choi's group who patiently provided so much help by sharing his great ideas for my research. Great thanks go to Dr. Weifei Hu in Professor Kyung K. Choi's group who helped me getting 249 sets of wind data and model uncertainty, and Dr. Nichoals Gaul for kindly providing me with various advice to my research.

I would also like to thank all my friends and colleagues who have encouraged me and provided insight into my research. In particular, I would like to thank, Hiroki Yamashita, Chris Feldmeier, Bryan Peterson, and Xiangkang Chen.

This research was supported by the National Science Foundation EPSC-1101284. The financial support is greatly acknowledged.

Finally I want to deeply thank my parents, who are always giving me support and love.

ABSTRACT

The objective of this study is to develop an integrated multibody dynamics computational framework for the deterministic and reliability-based design optimization of wind turbine drivetrains to obtain an optimal wind turbine gear design that ensures a target reliability under wind load and gear manufacturing uncertainties. Gears in wind turbine drivetrains are subjected to severe cyclic loading due to variable wind loads that are stochastic in nature. Thus, the failure rate of drivetrain systems is reported to be relatively higher than the other wind turbine components. It is known in wind energy industry that improving reliability of drivetrain designs is one of the key issues to make wind energy competitive as compared to fossil fuels. Furthermore, a wind turbine is a multi-physics system involving random wind loads, rotor blade aerodynamics, gear dynamics, electromagnetic generator and control systems. This makes an accurate prediction of product life of drivetrains challenging and very limited studies have been carried out regarding design optimization including the reliability-based design optimization (RBDO) of geared systems considering wind load and manufacturing uncertainties.

In order to address these essential and challenging issues on design optimization of wind turbine drivetrains under wind load and gear manufacturing uncertainties, the following issues are discussed in this study: (1) development of an efficient numerical procedure for gear dynamics simulation of complex multibody geared systems based on the multi-variable tabular contact search algorithm to account for detailed gear tooth contact geometry with profile modifications or surface imperfections; (2) development of an integrated multibody dynamics computational framework for deterministic and reliability-based design optimization of wind turbine drivetrains using the gear dynamics simulation software developed in (1) and RAMDO software by incorporating wide spatiotemporal wind load uncertainty model, pitting gear tooth contact fatigue model, and rotor blade aerodynamics model using NREL AeroDyn/FAST; and (3) deterministic and reliability-based design optimization of wind turbine drivetrain to minimize total weight of a drivetrain system while ensuring 20-year reliable service life with wind load and gear manufacturing uncertainties using the numerical procedure developed in this study.

To account for the wind load uncertainty, the joint probability density function (PDF) of 10-minute mean wind speed (V_{10}) and 10-minute turbulence intensity (I_{10}) is introduced for wind turbine drivetrain dynamics simulation. To consider wide spatiotemporal wind uncertainty (i.e., wind load uncertainty for different locations and in different years), uncertainties of all the joint PDF parameters of V_{10}, I_{10} and copula are considered, and PDF for each parameter is identified using 249 sets of wind data. This wind uncertainty model allows for the consideration of a wide range of probabilistic wind loads in the contact fatigue life prediction. For a given V_{10} and I_{10} obtained from the stochastic wind model, the random time-domain wind speed data is generated using NREL TurbSim, and then inputted into NREL FAST to perform the aerodynamic simulation of rotor blades to predict the transmitted torque and speed of the main shaft of the drivetrain that are sent to the multibody gear dynamics simulation as an input.

In order to predict gear contact fatigue life, a high-fidelity gear dynamics simulation model that considers the detailed gear contact geometry as well as the mesh stiffness variation needs to be developed to find the variability of maximum contact stresses under wind load uncertainty. This, however, leads to a computationally intensive procedure. To eliminate the computationally intensive iterative online collision detection algorithm, a numerical procedure for the multibody gear dynamics simulation based on the tabular contact search algorithm is proposed. Look-up contact tables are generated for a pair of gear tooth profiles by the contact geometry analysis prior to the dynamics simulation and the contact points that fulfill the non-conformal contact condition and mesh stiffness at each contact point are calculated for all pairs of gears in the drivetrain model.

This procedure allows for the detection of gear tooth contact in an efficient manner while retaining the precise contact geometry and mesh stiffness variation in the evaluation of mesh forces, thereby leading to a computationally efficient gear dynamics simulation suited for the design optimization procedure considering wind load uncertainty. Furthermore, the accuracy of mesh stiffness model introduced in this study and transmission error of gear tooth with tip relief are discussed, and a wind turbine drivetrain model developed using this approach is validated against test data provided in the literature.

The gear contact fatigue life is predicted based on the gear tooth pitting fatigue criteria and is defined by the sum of the number of stress cycles required for the fatigue

crack initiation and the number required for the crack to propagate from the initial to the critical crack length based on Paris-Erdogan equation for Mode II fracture. All the above procedures are integrated into the reliability-based design optimization software RAMDO for design optimization and reliability analysis of wind turbine drivetrains under wind load and manufacturing uncertainties.

A 750kW GRC wind turbine gearbox model is used to perform the design optimization and the reliability analysis. A deterministic design optimization (DDO) is performed first using an averaged joint PDF of wind load to ensure a 20-year service life. To this end, gear face width and tip relief (profile modification) are selected as design variables and optimized such that 20-year fatigue life is ensured while minimizing the total weight of drivetrains. It is important to notice here that an increase in face width leads to a decrease in the fatigue damage, but an increase in total weight. On the other hand, the tip relief has almost no effect on the total weight, but it has a major impact on the fatigue damage. It is shown in this study that the optimum tip relief allows for lowering the greatest maximum shear stresses on the tooth surface without relying heavily on face width widening to meet the 20-year fatigue life constraint and it leads to reduction of total drivetrain weight by 8.4%. However, if only face width is considered as design variable, total weight needs to be increased by 4.7% to meet the 20-year fatigue life constraint.

Furthermore, the reliability analysis at the DDO optimum design is carried out considering the large spatiotemporal wind load uncertainty and gear manufacturing uncertainty. Local surrogate models at DDO optimum design are generated using Dynamic Kriging method in RAMDO software to evaluate the gear contact fatigue damage. 49.5% reliability is obtained at the DDO optimum design, indicating that the probability of failure is 50.5%, which is as expected for the DDO design. RBDO is, therefore, necessary to further improve the reliability of the wind turbine drivetrain.

To this end, the sampling-based reliability analysis is carried out to evaluate the probability of failure for each design using the Monte Carlo Simulation (MCS) method. However, the use of a large number of MCS sample points leads to a large number of contact fatigue damage evaluation time using the 10-minute multibody drivetrain dynamics simulation, resulting in the RBDO calculation process being computational very intensive. In order to overcome the computational difficulty resulting from the use of high-fidelity

wind turbine drivetrain dynamics simulation, intermediate surrogate models are created prior to the RBDO process using the Dynamic Kriging method in RAMDO and used throughout the entire RBDO iteration process. It is demonstrated that the RBDO optimum obtained ensures the target 97.725 % reliability (two sigma quality level) with only 1.4 % increase in the total weight from the baseline design with 8.3 % reliability. This result clearly indicates the importance of incorporating the tip relief as a design variable that prevents larger increase in the face width causing an increase in weight. This, however, does not mean that a larger tip relief is always preferred since an optimum tip relief amount depends on stochastic wind loads and an optimum tip relief cannot be found deterministically. Furthermore, accuracy of the RBDO optimum obtained using the intermediate surrogate models is verified by the reliability analysis at the RBDO optimum using the local surrogate models. It is demonstrated that the integrated design optimization procedure developed in this study enables the cost effective and reliable design of wind turbine drivetrains.

PUBLIC ABSTRACT

This study aims to develop an integrated computational framework for the reliability-based design optimization (RBDO) of wind turbine drivetrains to ensure a target reliability under wind load and gear manufacturing uncertainties. Gears in wind turbine drivetrains are subjected to severe cyclic loading due to variable wind loads that are stochastic in nature. Thus, the failure rate of drivetrain systems is reported to be higher than the other wind turbine components, and improving drivetrain reliability while minimizing the cost (weight) is one of the key issues to make wind energy more competitive as compared to fossil fuels. In the numerical procedure developed in this study, a wide spatiotemporal variability for wind loads is considered using 249 sets of wind data to evaluate probabilistic contact fatigue life for the sampling-based RBDO. To address computational burdens resulting from multiple 10-minute gear contact dynamics simulations considering precise contact geometry, a tabular contact search algorithm using the combined nodal and non-conformal contact search approach is generalized to gear tooth contact. Using this simulation capability, an integrated computational framework for wind turbine drivetrain RBDO is developed by incorporating the wind load uncertainty model, the rotor blade aerodynamics model, drivetrain dynamics model, and the probabilistic contact fatigue failure model. It is demonstrated that the RBDO optimum obtained in this study for the 750kW GRC wind turbine drivetrain ensures the target 97.725 % reliability for 20-year service life by only 1.4 % increase in the total weight from the baseline design with 8.3 % reliability.

TABLE OF CONTENTS

LIST OF TABLES

LIST OF FIGURES

LIST OF ABBREVIATIONS AND SYMBOLS

a	Shape Parameter of Gamma Distribution
a_p	Half length of the crack
a_0	Half length of the initial crack
a_c	The critical crack length
$\mathbf{a}$	Random Vector Containing 20 Random Variables a
$\mathbf{A}^i$	Orientation Matrix of Body i
$\mathbf{A}_0^{ik}$	Orientation Matrix of The Tooth Profile Coordinate System Defined with Respect to The Body Coordinate System
$\mathbf{A}_T^{ij}$	Orientation Matrix of The Look-up Table Coordinate System of Bodies i and j
$\hat{\mathbf{A}}^i$	Orientation Matrix of Body i
$\bar{A}_i$	Mean Cross-section Area of Segment i
b	Scale Parameter of Gamma Distribution
b_0	Half Width of The Contact Patch
b_{eff}	Effective Face Width
$\mathbf{b}$	Random Vector Containing 20 Random Variables b
B	Tooth Face Width
B^0	Initial Design of Tooth Face Width
B^L	Lower Bound of Design Variable Face Width
B^U	Upper Bound of Design Variable Face Width
$\hat{B}^h$	Realizations of Random Face Width
c	Fatigue strength exponent
$c_{V\Sigma}(u,v;\theta)$	Copula Density Function
c_N^{ijk}	Damping Coefficient of Normal Contact Force Model
C	Scale Parameter of Weibull Distribution

C_p	Material Constant
$\mathbf{C}$	Random Vector Containing 20 Random Variables C
$\mathbf{C}^{ijk}$	Nonconformal Contact Constraint Equation
$\mathbf{C_q}$	Jacobian Matrix of The Constraint Equations
$\mathbf{d}$	Design Vector
$\mathbf{d}^L$	Lower Bound of Design Variable Vector $\mathbf{d}$
$\mathbf{d}^U$	Upper Bound of Design Variable Vector $\mathbf{d}$
$D_{10\text{min}}$	10-Minute Fatigue Damage
$D_{10\,\text{min}}^{ij}$	10-Minute Fatigue Damage Corresponding to a Wind Condition
$D_{1\text{year}}$	One-Year Fatigue Damage
$D_{20\text{year}}$	Twenty-Year Fatigue Damage
DDO	Deterministic Design Optimization
e	Accuracy of Contact Search Method
$\mathbf{e}$	Realization of The Stochastic Process in Surrogate Model Equation
E	Young's Modulus
E_{eff}	Effective Young's Modulus
E^{ik}, F^{ik}, G^{ik}	Coefficients of The First Fundamental Form
f_{V10}	Probability Density Function of 10-Minute Mean Wind Speed
$f_{\Sigma 10}$	Probability Density Function of 10-Minute Standard Deviation of Wind Speed
f_{VI}	Joint Probability Density Function of 10-Minute Mean Wind Speed and 10-Minute Turbulence Intensity
F_N^{ijk}	Normal Contact Force
$\bar{F}$	Contact force per unit length
$\mathbf{F}$	Model Matrix in Surrogate Model Equation
FAST	Fatigue, Aerodynamics, Structures, and Turbulence
FORM	First-Order Reliability Method

G	Shear Modulus of Rigidity
$G(\mathbf{X})$	Performance Measure
h_f	Ratio of The Radius of The Root Circle to The Inside Radius of The Gear Body
H_f	Effective Tooth Thickness
i_{10}	10-Minute Turbulence Intensity (Realization)
I_{10}	10-Minute Turbulence Intensity (Random Variable)
$\overline{I}_i$	Mean Second Moment Area of Segment i
$I_{\Omega_F}(\cdot)$	Indicator Function
J	Objective function of the optimization problem
k	Shape Parameter of Weibull Distribution
k_{N1}	Hertz's Contact Stiffness
k_{N2}	Tooth Bending Stiffness
k_{N3}	Gear Tooth Foundation Stiffness
k_N^{ijk}	Gear Mesh Stiffness
$\mathbf{k}$	Random Vector Containing 20 Random Variables k
ΔK	Stress Intensity Factor Range
ΔK_0	Threshold for The Crack Growth
K_t	Pore Shape Coefficient
L_i	Thickness of Tooth Segment i
L_f	Effective Tooth Length
L^{ik}, M^{ik}, N^{ik}	Coefficients of The Second Fundamental Form
m	Material Constant in The Paris Equation
M_{ring}^0	Mass of Ring Gear at Initial Design
M_{sun}^0	Mass of Sun Gear at Initial Design
M_{planet}^0	Mass of Planet Gear at Initial Design
$\mathbf{M}$	System Mass Matrix

MCS	Monte Carlo Simulation
$N_{a,p}$, $M_{b,q}$	p-th and q-th Order B-Spline Basis Functions
n	The Exponent of The Equivalent Maximum Contact Pressure for 10-minute Wind Load Scenario
n_s	Number of Slice for Sliced Helical Gear Tooth
n_{10}^{ij}	Number of Load Cycles of The Gear Tooth under Certain Wind Load Condition in The 10-Minute Simulation
n_v	Number of Discretized 10-Minute Mean Wind Speed
n_i	Number of Discretized 10-Minute Turbulence Intensity
$\bar{n}^{ik}$	Unit Normal Vector to The Tangent Plane Defined in The Profile Coordinate System
$\mathbf{n}^{ik}$	Normal Vector on The Tooth Surface
N	Total Number of Load Cycles Required for Contact Fatigue Failure
N_i	Number of Load Cycles Required to Initiate The Subsurface Crack
N_p	Number of Load Cycles Required for The Crack to Propagate to The Surface
N^{ijk}	Number of Load Cycles to Failure for Each Meshing Cycle k
N^{ij}	Number of Load Cycles to Failure as A Function of Equivalent Maximum Contact Pressure
N_s	Number of The Discretized Tooth Segments for Mesh Stiffness Calculation
N_{VI}	Number of MCS Points for Averaged Wind Load PDF Generation
$NMCS$	Number of MCS Points
p_{max}	Maximum Contact Pressure
$\bar{p}_{\max}^{ij}$	Equivalent Maximum Contact Pressure for 10-Minute Wind Load Scenario
P_F	Probability of Failure

P_H	Hydrostatic Stress
P_F^{Tar}	Target Probability of Failure
$\mathbf{P}_{a,b}$	Control Points Vector
PDF	Probability Density Function
PSD	Power Spectral Density
$\mathbf{q}^i$	Generalized Coordinate Vector of Body *i*
$\mathbf{Q}_e$	Generalized External Force Vector
$\mathbf{Q}_v$	Vector of Inertia Forces
Q_{ti}	Gear Tooth Compliance Associated with The Transverse Normal Deformation
Q_{si}	Gear Tooth Compliance Associated with The Transverse Shearing
Q_{mi}	Gear Tooth Compliance Associated with The Pure Bending
r_a	Radius That The Tip Relief Ends
r_s	Radius That The Tip Relief Starts
r_b	Gear Base Radius
$\mathbf{r}^{ik}$	Global Position Vector at Contact Point *k* on Body *i*
$\dot{\mathbf{r}}^{ijk}$	Relative Velocity Vector Gear Bodies *i* And *j* at Contact Point *k*
R_1, R_2	Radius of Curvature at Tooth Contact Point
$\bar{R}$	Equivalent Radius Evaluated by The Principal Radii of Curvature at Contact Point
$\mathbf{R}^i$	Global Position Vector of The Origin of The Body Coordinate System
$\hat{\mathbf{R}}^i$	Global Position Vector of The Origin of The Body Coordinate System Defined with Respect to The Look-Up Table Coordinate System
RBDO	Reliability Based Design Optimization
s	Crack Growth Driving Force
$\mathbf{s}^{ik}$	Surface Parameter Vector of Tooth *k* of Body *i*
S_i	Distance Between The Segment *i* And The Contact Point

S_u	Ultimate Tensile Strength
SORM	Second Order Reliability Method
SQP	Sequential Quadratic Programming
$\bar{\mathbf{t}}_l^{ik}$	Tangent Vector Defined in The Profile Coordinate System
u	Marginal Cumulative Distribution Function of 10-Minute Mean Wind Speed
$\bar{\mathbf{u}}^{ik}$	Local Position Vector Defined with Respect to The Body Coordinate System
$\bar{\mathbf{u}}_0^{ik}$	Local Position Vector of The Origin of The Tooth Profile Coordinate System
$\bar{\mathbf{u}}_p^{ik}$	Local Position Vector Defined with Respect to The Profile Coordinate System
U	A Factor Considering The Crack Closure As a Function of Crack Length
$\mathbf{U}^{ij}$	Time-Domain 10-Minute Random Wind Speed Vector (u^{ij}(t) v^{ij}(t) w^{ij}(t))
v	Marginal Cumulative Distribution Function of Standard Deviation of 10-Minute Wind Speed
v_{10}	10-Minute Mean Wind Speed (Realization)
$\mathbf{v}_T^{ijk}$	Unit Relative Velocity Vector Along The Tangent Plane of Contact
V_{10}	10-Minute Mean Wind Speed (Random Variable)
$\mathbf{x}_s$	Sample Points for Surrogate Model Generation
$\hat{\mathbf{y}}^h$	Realization Vector of Random Wind Load Parameters
$\mathbf{y}$	Random Vector for Probability Density Function Parameters (C k a b τ)
$\mathbf{y}_s$	Responses of The Sample Points for Surrogate Model Generation
$\mathbf{Y}$	Random Vector for Parameters (C k a b τ) for 20 Years Wind Load
z_0	The Sub-Surface Depth That Greatest Value of The Maximum Shear Stress Occurs
α	The Direction That The Subsurface Crack Grows

α_t	Transverse Pressure Angle
β	Pressure Angle at The Contact Point
β_h	Helix Angle
$\boldsymbol{\beta}$	Vector of Regression Coefficients in Surrogate Model Equation
δ_K	Material Constant That Accounts for Notch Effects
δ_a	Amount of Tip Relief at Tooth Tip
$\delta(r)$	Amount of Tip Relief as A Function of Gear Radius
δ_a^0	Initial Design of Tip Relief
δ_a^L	Lower Bound of Design Variable Tip Relief
δ_a^U	Upper Bound of Design Variable Tip Relief
δ^{ijk}	Penetration Between Tooth Surfaces
$\dot{\delta}^{ijk}$	Penetration Rate
κ_l^{ik}	Principle Curvature
μ^{ijk}	Coefficient of Friction
μ_B	Mean of The Random Face Width
μ_{δ_a}	Mean of The Random Tip Relief
θ	Correlation Coefficient for Copula
$\Delta\theta$	Rotation Angle of Look-Up Coordinate System Defined on Sliced Tooth
$\boldsymbol{\theta}$	Process Correlation Parameter Vector in Surrogate Model Equation
$\boldsymbol{\theta}^i$	$Z^i X^i Y^i$ -Type Euler Angles $(\psi^i, \phi^i, \theta^i)$ of Body *i* with Respect to The Body Coordinate System
$\hat{\boldsymbol{\theta}}^i$	$Z^i X^i Y^i$ -Type Euler Angles $(\psi^i, \phi^i, \theta^i)$ of Body *i* Defined with Respect to The Look-Up Table Coordinate System $(\hat{\psi}^i, \hat{\phi}^i, \hat{\theta}^i)$
ν	Poisson's Ratio
ρ_i, σ_j	Weight Coefficients for Smoothing
σ_{10}	10-Minute Standard Deviation of Wind Speed (Realization)
σ_f'	Fatigue Strength Coefficient

Σ_{10}	10-Minute Standard Deviation of Wind Speed (Random Variable)
τ_{max}	Maximum Shear Stress
τ_f'	Fatigue Strength Coefficient
τ	Kendall's Tau of Correlated Random Variables
$\boldsymbol{\tau}$	Random Vector Containing 20 Random Variables τ
η	Material Constant That Accounts for Matrix Microstructure
ψ	Represents The Reduction in Load Section Due to Porosity
ε	Porosity Fraction
$\hat{\varepsilon}$	Error in Percentage in Probability of Failure Calculation
Ω_F	Failure Domain

CHAPTER 1
INTRODUCTION

This study is aimed to develop an integrated multibody dynamics computational framework for the reliability-based design optimization of wind turbine drivetrains considering wind load and manufacturing uncertainties. In this chapter, background and motivation of this study are provided. In particular, failure modes of wind turbine drivetrains and existing approaches for failure prediction of wind turbine drivetrains are overviewed and then existing gear contact analysis models used in general multibody dynamics simulation are discussed in order to highlight important features and drawbacks of various approaches that are currently in use. Furthermore, the deterministic and reliability-based design optimization procedures for gears are briefly overviewed and the need for profile optimization are discussed for complex multi-stage wind turbine drivetrains. Finally, the objectives and organization of this thesis are provided.

1.1 Background and Motivation

1.1.1 Wind Turbine Drivetrain Failure

An accurate prediction of the product life of drivetrains is crucial for safe and reliable operation of wind turbines. It is reported that the failure rate of gearboxes is higher than other wind turbine components [1-3]. Failures of gear components stop wind turbine operation, and pecuniary loss due to turbine downtime and maintenance increases dramatically, resulting in wind energy being less competitive when compared to existing fossil fuels [2]. For this reason, establishing a reliable and cost-effective design procedure for wind turbine components is of crucial importance.

According to the National Renewable Energy Laboratory (NREL) report [4], wind turbine drivetrain failure modes are classified as follows: (a) bending fatigue, (b) contact fatigue, (c) wear, (d) scuffing, (e) grinding cracks, and (f) case-core separation cracks. Main cause of bending fatigue is an inadequate material cleanliness or incomplete hardening on the tooth root. Wear is due to the tearing of asperities and it can be alleviated by sufficient lubrication on tooth surfaces. Scuffing also called as severe adhesion occurs when lubricant dries out accidently. It is known that grinding cracks and case-core

separation cracks are caused by improper heat treatment of gear materials. These failures can be prevented by the use of appropriate materials and careful surface treatments. On the other hand, more careful consideration needs to be given to rolling contact fatigue in gear design [5]. Since a gear tooth experiences severe cyclic rolling and sliding contact resulting from highly variable wind loads which are stochastic in nature, prediction of fatigue failure is not straightforward, thus contact fatigue becomes one of the major causes of unintended gearbox failure that would prevent wind turbines from achieving the expected service life [6, 7]. Furthermore, the gear shaft misalignment, which can be classified into a parallel misalignment and angular misalignment due to the manufacturing assembly error and/or the driveshaft defection caused by an overhanging load of the wind turbine rotor blades, alters gear tooth contact stress distribution and can have significant impact on the gear contact fatigue damage [8-10].

The gear tooth contact fatigue is caused by either surface-initiated cracking or subsurface-initiated cracking [11]. Overheating of tooth surfaces due to insufficient lubrication leads to the surface-initiated failure, while the subsurface crack is initiated for properly lubricated gears in most cases. It is widely agreed that the contact fatigue failure process due to the subsurface-initiated crack can be divided into two stages: [12, 13] (1) crack initiation period, and (2) crack propagation period. Contact fatigue life is estimated by the sum of total number of load cycles required for the crack initiation and that required for the crack to propagate to the surface [11]. The crack initiation process can be modeled by the multi-axial high cycle fatigue criteria [14-16], which is influenced by contact stress and material fatigue parameters. The crack propagation process is modeled by the Paris equation using mode II stress intensity factor [17, 18]. For case-hardened materials, it is observed that the crack propagation under rolling contact is influenced by the ratio of the maximum shear stress to the material hardness [19, 20]. In other words, to estimate the contact fatigue life of wind turbine drivetrain gear teeth, the maximum shear stress needs to be predicted accurately under various dynamic load conditions. The use of a deterministic single domain simulation may, however, lead to an unrealistic load prediction due to high variability of wind loads, thereby resulting in underestimation or overestimation of the gear tooth fatigue life. A probabilistic pitting fatigue life prediction procedure is proposed in the literature [21], in which the wind load uncertainty is defined

solely by the probability density function (PDF) of the mean wind speed using the generalized gamma function and the random maximum contact pressure, obtained using the probabilistic analysis of the multibody drivetrain dynamics, is used to find the pitting fatigue life, considering the effect of wind load variability.

1.1.2 Multibody Dynamics Simulation of Geared Systems

Multibody dynamics simulation is widely used to predict the dynamic mesh force variation as well as transmission error of complex gear trains. Lumped torsional mass-spring models that account for the effect of variable stiffness associated with the gear tooth contact are widely used in the vibration analysis of gear systems [22-24]. While the lumped vibration models are computationally efficient and provide an important insight into the dynamic response of gear trains, they are, in general, used for the analysis of steady-state response in the frequency domain and the three-dimensional gear tooth geometry is not fully considered in the model.

To perform the time-domain transient analysis of gear systems, multibody dynamics models have been used for various engineering applications [25-28]. The tangential and bending deformation of the gear tooth can be considered by introducing discrete translational and rotational springs defined between the rigid tooth and rigid gear body [29, 30]. Flexibility of the entire gear body can be incorporated into multibody dynamics simulation using the floating frame of reference formulation with modal reduction techniques, allowing for prediction of accurate tooth impact force influenced by the tooth and gear wheel deformation [31]. Since flexible multibody models, in general, lead to large dimensionality to ensure accuracy, the computational cost is high and application to the gear train dynamics simulation would be impractical. To reduce the computational cost for the full finite element gear model, the surface integral solution for the tooth contact is integrated into the finite element model, thereby allowing for the use of coarse finite element meshes while retaining the precise gear tooth contact calculation [32, 33]. For wind turbine applications, various drivetrain models are developed using either rigid or flexible multibody dynamics approaches [34-37], some of which are validated against test bench results [38]. Furthermore, the probabilistic flexible multibody gear dynamics

simulation has been advocated for wind turbine gearboxes to account for uncertainties associated with wind loads and manufacturing errors [39].

In gear dynamics simulation, precise tooth surface geometry description and accurate prediction of the location of the contact point are crucial to the mesh force and transmission error evaluation of gear trains [40]. In particular, contact search for the tooth surface geometry obtained by CAD and/or direct tooth measurement leads to extensive computation efforts in the dynamic simulation. In the constraint contact formulation, the non-conformal contact condition between tooth surfaces in contact is imposed on the equations of motion as constraint equations and the normal contact forces are evaluated by Lagrange multipliers associated with the contact constraint. This formulation leads to an accurate and efficient prediction of the contact point on the continuous smooth surface [41].

However, intermittent contact of multiple gear teeth is involved in the time-domain dynamic analysis, thus use of the constraint contact formulation necessitates ad hoc numerical procedures for modeling the gear tooth impact as well as loss of contact due to changes in the system degrees of freedom. Furthermore, a rigid contact assumption used in the formulation prevents consideration of the effect of variable mesh stiffness. For this reason, the elastic (penalty) contact approach has been widely used in the analysis of multibody gear contact dynamics and the normal contact force is defined as a compliant force function of the penetration between two surfaces in contact. The contact point can be determined online by either solving nonlinear contact search equations iteratively to ensure the tangency condition or searching a pair of nodes that have the maximum penetration on the discretized surfaces. The nodal search method, however, is not recommended due to the discrete surface representation which causes numerical noise in mesh forces. In the use of contact search equations, on the other hand, nonlinear equations need to be solved iteratively at every time step, leading to extensive computational time for the entire gear train model. Furthermore, a special technique is required for treating a discontinuous contact event such as impact, loss, or jump in contact point that can occur when gear geometry imperfections are involved. To address these fundamental and essential issues in the contact search algorithm for gear tooth surfaces with geometric imperfection, a combined nodal and non-conformal contact search algorithm is introduced and generalized to the gear tooth contact problem in this study.

1.1.3 Gear Design Optimization

Gear design is a complicated iterative process, involving many design variables, requirements, and constraints [42]. Many gear design optimizations have been carried out using deterministic design variables and loads. In most literature, optimization of the contact ratio, face width, and tooth tip and root profiles is explored to meet the fatigue life constraint associated with gear tooth bending and surface pitting failures [43-45]. Minimization of gear transmission error, which is the main source of gearbox noise and vibration, is also explored by modifying the gear tooth profile through lead crowning and tip/root relief [46-48]. Since tooth profile modification is on an order of microns and it is in the same order of manufacturing variance, a robust design optimization using Taguchi Method is adopted in the literature [49-51] to make the gear profile design insensitive to the manufacturing variance.

It is suggested in the literature [49] that a gear tooth profile optimization process consists of two steps: (1) generation of a candidate design that meets design requirements (e.g., the center distance, gear ratio, etc.) and constraints (e.g., maximum face width, maximum bending and contact stresses, etc.); and (2) tooth profile optimization. That is, the candidate design is found at the first stage and then further refinement is made by the profile modification at the second stage such that the transmission error can be minimized and insensitive to the manufacturing variance [49].

It is also shown that the maximum contact pressure due to the cyclical contact loading can be lowered by tooth profile modification (tip relief) [18], thereby allowing for the lowering of the maximum shear stress beneath the contact surface, which is a major driving force for the crack growth due to pitting fatigue. It is important to notice here that, for the evaluation of the effect of profile modification on the contact fatigue life, precise gear tooth contact geometry as well as the mesh stiffness variation need to be incorporated into the multibody gear dynamics simulation model to account for the contact pressure variation associated with the gear tooth microgeometry.

Furthermore, to meet a target reliability for gear tooth contact failure, reliability-based design optimization (RBDO) of an automobile gearbox is discussed in the literature [52], in which gear face width is selected as design variable. RBDO has proven to be an effective approach that enables reliable and cost-effective design for a wide variety of

engineering applications under uncertainties [53-56]. In structural design problems, RBDO is usually utilized such that the design cost function can be minimized while ensuring a target probability of failure under uncertainty, associated with design variables as well as system parameters including material properties, geometry, loads, etc [57].

In the RBDO process, reliability analysis is carried out for different values of the design variables in the iterative solution process, and sensitivity based or sampling based methods are employed to evaluate the reliability. In the sensitivity based approach, the first order reliability method (FORM) [58] or the second order reliability method (SORM) [59] are commonly used to approximate the constraint performance functions. However, for many engineering problems, the gradient of constraint performance functions required to calculate the probability of failure [58] is difficult to obtain. Thus, sampling based methods are utilized and the probability of failure is evaluated by Monte Carlo simulation (MCS) instead. This, however, requires a large number of evaluations of constraint performance functions, making the sampling based approach computationally intensive.

To overcome the computational burden introduced by MCS method, surrogate models are created and used to evaluate the constraint performance functions for various selections of design variables [60]. There are many types of surrogate models proposed in the literature [61-65]. Among others, polynomial response surfaces [61]; support vector repressors and classifiers (SVR, SVC) [62]; neural networks [63]; radial basis functions [64]; and kriging methods [65] are widely used due to their capability of dealing with highly nonlinear problems. The dynamic kriging method [57], suited for highly nonlinear problems, is successfully applied to RBDO of wind turbine composite blades under wind load uncertainty [66].

1.2 Objective of the Study

Despite many studies on the gear contact and failure analysis of wind turbine drivetrains, limited studies have been carried out regarding reliability-based design optimization (RBDO) of geared systems considering wind load and manufacturing uncertainties. Furthermore, a wind turbine is a multi-physics system involving mechanical and aerodynamics simulations, thus an integrated simulation framework is required such that the wind load uncertainty, random wind field generation, rotor blade aerodynamics, drivetrain dynamics considering the gear tooth contact geometry including the profile

modification effect, and contact fatigue failure models can be integrated into the design optimization framework. It is, therefore, the objective of this study to develop an integrated multibody dynamics computational framework for the deterministic and reliability-based design optimization of wind turbine drivetrains considering wind load and manufacturing uncertainties to meet the target reliability for 20-year service life. To this end, the following issues are addressed in this thesis:

(1) Develop an efficient numerical procedure for gear dynamics simulation of complex multibody geared systems based on the multi-variable tabular contact search algorithm to account for detailed gear tooth contact geometry with surface modifications or imperfections.

(2) Develop an integrated multibody dynamics computational framework for deterministic and reliability-based design optimization of wind turbine drivetrains using the gear dynamics simulation software developed in (1) and RAMDO software by incorporating a wide spatiotemporal wind load uncertainty model, pitting gear tooth contact fatigue models, and rotor blade aerodynamics models using NREL AeroDyn/FAST.

(3) Conduct the deterministic and reliability-based design optimization of wind turbine drivetrains using the numerical procedure developed. To this end, gear tooth width and tip relief (profile modification) are selected as design variables to minimize the total weight of a drivetrain system while ensuring 20-year service life under uncertainties associated with wind loads and gear tooth manufacturing.

1.3 Organization of Thesis

This thesis is organized as follows: a numerical procedure for gear dynamics simulation of general multibody systems is developed based on the multi-variable tabular contact search algorithm to account for detailed gear tooth contact geometry with surface modifications or imperfections in Chapter 2. Several numerical examples are presented to demonstrate the numerical procedure developed for gear dynamic simulation, and validation against test results for NREL wind turbine drivetrains is presented in Chapter 3. In Chapter 4, the pitting contact fatigue model considering both gear subsurface crack initiation and crack propagation is introduced to evaluate gear contact fatigue damage and integrated into the multibody gear dynamics simulation framework presented in Chapter 2.

Furthermore, an integrated computational framework for design optimization of wind turbine drivetrains is developed using the gear dynamics simulation capability developed in this study and RAMDO software by incorporating a wide spatiotemporal wind load uncertainty model, pitting gear tooth contact fatigue model, and rotor blade aerodynamics model using NREL AeroDyn/FAST. Deterministic design optimization (DDO) of a wind turbine drivetrain using averaged PDF of wind uncertainty model is discussed. In Chapter 5, the reliability analysis is discussed considering a wide spatiotemporal wind load uncertainty and gear manufacturing variance associated with gear face width and profile modification (i.e., tip relief). In Chapter 6, a numerical procedure for RBDO of wind turbine drivetrains is developed to meet the target probability of failure for 20-year service life while minimizing the total weight. The intermediate surrogate model is introduced using the dynamics kriging method to address the large computational cost required for the RBDO process. Summary, conclusions, and future work are provided in Chapter 7.

CHAPTER 2
GEAR DYNAMICS SIMULATION

2.1 Introduction

In this chapter, a numerical procedure for gear dynamics simulation of multibody systems is developed using the tabular contact search method. Existing online contact search algorithms, which are widely used in multibody dynamics simulation, lead to a computational intensive procedure if detailed tooth surface geometry described by CAD or measured data points are considered with geometric imperfections. In the numerical procedure developed in this chapter, the contact geometry analysis based on the non-conformal contact condition is performed using the detailed tooth surface description prior to the dynamic simulation, and then the contact point as well as the tooth geometry at the contact point stored in the look-up contact tables are used to determine mesh forces in the multibody gear dynamics simulation. This allows for detecting multi-point contact without any iterative procedures and the contact point on the back side of the tooth can also be considered by switching look-up contact tables in a straightforward manner.

2.2 Parameterization of Gear Tooth Surface

As shown in Fig. 2.1, the global position vector of a contact point on the tooth *k* of rigid gear body *i* can be expressed as

$$\mathbf{r}^{ik} = \mathbf{R}^i + \mathbf{A}^i \bar{\mathbf{u}}^{ik} \tag{2.1}$$

where $\mathbf{R}^i = [R_X^i \quad R_Y^i \quad R_Z^i]^T$ is the global position vector of the origin of the body coordinate system attached to the center of gear body; $\mathbf{A}^i$ is the orientation matrix parameterized by the three Euler angles $\boldsymbol{\theta}^i = [\psi^i \quad \phi^i \quad \theta^i]^T$ (successive rotations about the Z^i, X^i and Y^i axes of the body coordinate system); and $\bar{\mathbf{u}}^{ik}$ defines the location of the contact point defined with respect to the body coordinate system. The gear tooth geometry is parameterized by two surface parameters s_1^{ik} and s_2^{ik}, and the local position vector $\bar{\mathbf{u}}^{ik}$ can be expressed as

$$\bar{\mathbf{u}}^{ik}(s_1^{ik}, s_2^{ik}) = \bar{\mathbf{u}}_0^{ik} + \mathbf{A}_0^{ik} \bar{\mathbf{u}}_p^{ik}(s_1^{ik}, s_2^{ik}) \tag{2.2}$$

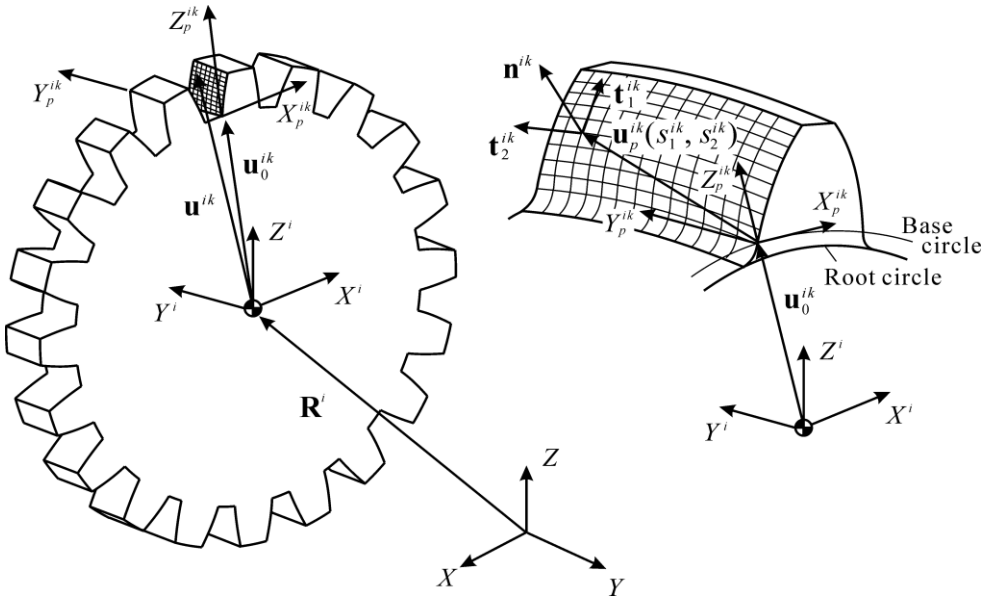

Fig 2.1. Gear coordinate systems

In the preceding equation, $\bar{\mathbf{u}}_0^{ik}$ and $\mathbf{A}_0^{ik}$ define the location and orientation of the tooth profile coordinate system with respect to the body coordinate system, respectively. The location of the contact point on the tooth profile is defined by $\bar{\mathbf{u}}_p^{ik}(s_1^{ik}, s_2^{ik})$ with respect to the profile coordinate system using the surface parameters in either analytical [40] or numerical form [67, 68]. In the B-spline computational surface geometry representation, the tooth surface can be described with respect to the profile coordinate system as follows [67]:

$$\bar{\mathbf{u}}_p(s_1, s_2) = \sum_{a=1}^{n}\sum_{b=1}^{m} N_{a,p}(s_1) M_{b,q}(s_2) \mathbf{P}_{a,b} \tag{2.3}$$

For simplicity, the superscripts *ik* that denote the body and contact numbers are omitted. In the preceding equation, *p* and *q* are orders of polynomials, *n* and *m* are the numbers of basis functions $N_{a,p}(s_1)$ and $M_{b,q}(s_2)$, respectively, and $\mathbf{P}_{a,b}$ $(a = 1, \cdots, n; \quad b = 1, \cdots, m)$ is a vector of control points. The surface parameters in Eq. 2.3 are defined as knots in the entire parametric B-spline domain.

On the other hand, in the case of tooth surface obtained from the direct measurement, smoothing of the original data points $(\bar{\mathbf{u}}_p)_{ij} = [x_i \quad y_j \quad z_{ij}]^T$

$(i=1,...,n_x;\ j=1,...,n_y)$ needs to be performed to remove undesirable irregularities associated with the measurement noise that causes numerical convergence problems in the contact analysis. To this end, smoothing spline function $f(x,y)$ is generated from the data points such that the following functional J can be minimized [68]:

$$J(f)=\int_{y_a}^{y_b}\int_{x_a}^{x_a}\left(\frac{\partial^4 f(x,y)}{\partial x^2\partial y^2}\right)^2 dxdy+\sum_{i=1}^{n_x}\frac{1}{\rho_i}\int_{y_a}^{y_a}\left(\frac{\partial^2 f(x_i,y)}{\partial y^2}\right)^2 dy$$
$$+\sum_{j=1}^{n_y}\frac{1}{\sigma_j}\int_{x_a}^{x_b}\left(\frac{\partial^2 f(x,y_j)}{\partial x^2}\right)^2 dx+\sum_{i=1}^{n_x}\sum_{j=1}^{n_y}\frac{1}{\rho_i\sigma_j}\left(f(x_i,y_j)-z_{ij}\right)^2 \tag{2.4}$$

where $[x_a, x_b]$ and $[y_a, y_b]$ are the data domain and $\rho_i \geq 0$ and $\sigma_j \geq 0$ are weight coefficients for smoothing. Furthermore, to ensure the continuity of the derivatives of the generated surface, the three-layer smoothing spline technique is employed [41]. If the tooth profile is assumed to be constant along the width, the smoothing spline curve can be used instead to parameterize the tooth surface.

Using the local position vector defined by Eq. 2.3, a unit normal vector to the tangent plane can be defined in the profile coordinate system as

$$\bar{\mathbf{n}}^{ik}=\frac{\bar{\mathbf{t}}_1^{ik}\times\bar{\mathbf{t}}_2^{ik}}{\left|\bar{\mathbf{t}}_1^{ik}\times\bar{\mathbf{t}}_2^{ik}\right|} \tag{2.5}$$

where $\bar{\mathbf{t}}_1^{ik}=\partial\bar{\mathbf{u}}_p^{ik}/\partial s_1^{ik}$ and $\bar{\mathbf{t}}_2^{ik}=\partial\bar{\mathbf{u}}_p^{ik}/\partial s_2^{ik}$ are the tangent vectors. The principal curvature κ_l^{ik} can then be obtained as the eigenvalues from the following generalized eigenvalue problem [40]:

$$\left(\mathbf{B}^{ik}-\kappa_l^{ik}\mathbf{A}^{ik}\right)\mathbf{X}_l^{ik}=\mathbf{0},\quad l=1,2 \tag{2.6}$$

where

$$\mathbf{A}^{ik}=\begin{bmatrix}E^{ik} & F^{ik}\\ F^{ik} & G^{ik}\end{bmatrix}\quad\text{and}\quad\mathbf{B}^{ik}=\begin{bmatrix}L^{ik} & M^{ik}\\ M^{ik} & N^{ik}\end{bmatrix} \tag{2.7}$$

In the preceding matrices, E^{ik}, F^{ik}, and G^{ik} are coefficients of the first fundamental form defined by

$$E^{ik}=\bar{\mathbf{t}}_1^{ik}\cdot\bar{\mathbf{t}}_1^{ik},\quad F^{ik}=\bar{\mathbf{t}}_1^{ik}\cdot\bar{\mathbf{t}}_2^{ik},\quad G^{ik}=\bar{\mathbf{t}}_2^{ik}\cdot\bar{\mathbf{t}}_2^{ik} \tag{2.8}$$

and L^{ik}, M^{ik} and N^{ik} are coefficients of the second fundamental form defined as follows:

$$\left.\begin{aligned} L^{ik} &= -\bar{\mathbf{t}}_1^{ik} \cdot \left(\frac{\partial \bar{\mathbf{n}}^{ik}}{\partial s_1^{ik}} \right) \\ M^{ik} &= -\frac{1}{2}\left(\bar{\mathbf{t}}_1^{ik} \cdot \left(\frac{\partial \bar{\mathbf{n}}^{ik}}{\partial s_2^{ik}} \right) + \bar{\mathbf{t}}_2^{ik} \cdot \left(\frac{\partial \bar{\mathbf{n}}^{ik}}{\partial s_1^{ik}} \right) \right) \\ N^{ik} &= -\bar{\mathbf{t}}_2^{ik} \cdot \left(\frac{\partial \bar{\mathbf{n}}^{ik}}{\partial s_2^{ik}} \right) \end{aligned}\right\} \tag{2.9}$$

The principal directions of the principal curvatures κ_1^{ik} and κ_2^{ik} can be defined by the eigenvectors associated with them and they are used to evaluate the Hertzian contact patch between the tooth surfaces in contact.

2.3 Gear Contact Formulation

2.3.1 Tabular Contact Search for Gear Tooth Contact

With the detailed tooth surface description discussed in the previous section, the contact search is performed in the multibody dynamics simulation. Use of online contact search algorithms, which are widely used in general multibody dynamics computer formulations, lead to extensive computational time if general CAD or measured tooth profiles [69,70] are considered together with various gear geometry imperfections. For this reason, a contact search algorithm based on look-up contact tables is generalized in this study to the gear dynamics simulation of multibody systems. The tabular contact search method has been successfully used for solving wheel and rail contact problems in multibody railroad vehicle dynamics simulation, in which the contact geometry between wheel and rail surfaces is essential to the evaluation of normal and tangential contact forces [41]. This procedure allows for incorporating measured wear profiles with plastic material flows [71] and complex rail geometries in switching and crossing described in computational geometry representation [72] while retaining the detailed contact geometry in multibody dynamics simulation.

Since the gear tooth contact is periodic, solution to the contact geometry problem of a one-tooth contact model can be repeatedly used for detecting the contact of all the teeth in the gear body. In other words, the contact geometry analysis for a one-tooth model is performed *a priori* for various rotation angles and the contact point as well as the tooth

geometry at the contact point, that includes tangents, normal, and principal curvatures, are stored at various configurations in the look-up table. The look-up table obtained for the one-tooth model is then interpolated as a function of rotation of gear bodies to determine the location of the contact point online. One can also include the in-plane and out-of-plane relative displacement between centers of the gear bodies as an input to the look-up contact tables to consider the effect of the shaft deflection and the bearing compliance on the change in the contact point on the tooth surfaces. Furthermore, use of look-up contact tables allows for the detection of a jump in contact point in a straightforward manner for measured tooth profiles with tooth surface imperfections [73]. While look-up contact tables of all pairs of gears in the gear train under consideration need to be prepared in advance, the gear tooth contact search can be performed efficiently without any iterative solution procedures in the dynamic simulation while retaining the detailed gear contact geometry in calculation of the mesh forces.

2.3.2 Contact Geometry Analysis Using Non-conformal Contact Constraints

In order to generate the look-up contact tables, the contact geometry analysis of a one-tooth model is carried out. The method is based on the non-conformal contact condition imposed on gear teeth in contact. That is, two points on the two surfaces must coincide and the two surfaces must have the same tangent planes at the contact point. These two conditions are described by the following five constraint equations for contact k between surface i and j [41, 74]:

$$\mathbf{C}^{ijk}(\mathbf{q}^i,\mathbf{q}^j,\mathbf{s}^{ik},\mathbf{s}^{jk}) = \begin{bmatrix} \mathbf{t}_1^{jk}\cdot(\mathbf{r}^{ik}-\mathbf{r}^{jk}) \\ \mathbf{t}_2^{jk}\cdot(\mathbf{r}^{ik}-\mathbf{r}^{jk}) \\ \mathbf{n}^{jk}\cdot(\mathbf{r}^{ik}-\mathbf{r}^{jk}) \\ \mathbf{t}_1^{ik}\cdot\mathbf{n}^{jk} \\ \mathbf{t}_2^{ik}\cdot\mathbf{n}^{jk} \end{bmatrix} = \mathbf{0} \tag{2.10}$$

The preceding equations are defined for sixteen unknowns (i.e., six generalized coordinates $\mathbf{q}^i = [(\mathbf{R}^i)^T \quad (\boldsymbol{\theta}^i)^T]^T$ and two surface parameters $\mathbf{s}^{ik} = [s_1^{ik} \quad s_2^{ik}]^T$ for each body). To determine all the sixteen unknowns, the three translational coordinates and two rotations about the axes perpendicular to the gear rotation axis of gear j are constrained first. This leads to the following five constraint equations:

$$\mathbf{R}^j - \mathbf{R}_0^j = \mathbf{0}, \quad \psi^j - \psi_0^j = 0, \quad \phi^j - \phi_0^j = 0 \tag{2.11}$$

where the gear spin axis is defined by the Y^j-axis of the body coordinate system as shown in Figs. 2.1 and 2.2; ψ^j and ϕ^j are Euler angles about the Z^j and X^j axes of the body coordinate system, respectively. The subscript 0 in the preceding equations denotes coordinates at the initial configuration. By imposing the non-conformal contact constraint equations given by Eq. 2.10, the location of the contact point (i.e., surface parameters $\mathbf{s}^i$ and $\mathbf{s}^j$) and the spin angle θ^j of gear *j* are determined for prescribed position and orientation of gear *i*. In the simplest case, only spin rotation angle θ^i is selected as a variable and it leads to the following six equations:

$$\mathbf{R}^i - \mathbf{R}_0^i = \mathbf{0}, \quad \psi^i - \psi_0^i = 0, \quad \phi^i - \phi_0^i = 0, \quad \theta^i - \delta_\theta^{i(n)} = 0 \tag{2.12}$$

where $\delta_\theta^{i(n)}$ defines the prescribed spin angle at incremental step *n* and the spin angle is defined in the range that the two teeth are in contact. The effect of the axial, radial and angular misalignments of gear shaft can also be considered by prescribing the relative deviations between gear body *i* and *j*. A total of sixteen equations given by Eqs. 2.10, 2.11and 2.12 are solved iteratively using Newton-Raphson method for sixteen unknowns at every step *n* and the results are stored in the look-up contact table. The look-up table contains not only the generalized coordinates and surface parameters of both bodies at each configuration, but also the tangent vectors ($\bar{\mathbf{t}}_1^{ik}$ and $\bar{\mathbf{t}}_2^{ik}$), unit normal ($\bar{\mathbf{n}}^{ik}$), principal curvatures (κ_1^{ik} and κ_2^{ik}) at the contact point evaluated by Eqs. 2.5 and 2.6.

2.3.3 Combined Nodal and Non-Conformal Contact Search

For ideal involute profiles, use of the non-conformal equations lead to efficient solutions in the contact geometry analysis of gear teeth. On the other hand, in the case of measured tooth profiles with tooth surface imperfections [69,70], undesirable jumps in the contact point occur on the surface and use of the non-conformal contact search leads to a difficulty in finding the correct contact point. Since the solution of the iterative solution procedure is obtained around the initial estimate provided, it fails to detect the discontinuous jump in contact point if the initial estimate is far from the solution sought. For this reason, in this study, the nodal search is employed as a global search to provide a *rough* estimate of the contact point (i.e., surface parameters) and then the contact point

obtained is used as the initial estimate for the non-conformal contact search equations as shown in Fig. 2.2. Such a two-stage procedure leads to a robust algorithm, which allows for detecting an appropriate initial estimate for non-conformal contact search for tooth surfaces with tooth surface imperfections.

To determine the contact point between two arbitrary surfaces in the three-dimensional space using the nodal search method, each tooth surface is discretized into nodal points first and the nodal coordinates, defined with respect to its profile coordinate system, are stored in a tabular form together with the surface parameters associated with them. For a given configuration of two gear teeth, the global position of the discretized nodal points are evaluated using Eq. 2.1. The gear surfaces in the three-dimensional space are then sliced into a number of two-dimensional plane along the *Z*-axis as shown in Fig. 2.2.

The cut planes that contain both tooth profile curves are extracted for further consideration. Having obtained the multiple two-dimensional profile curves discretized by a number of nodal points in the *XY* cut planes, the relative distances between the two curves along the *X*-axis are calculated and the minimum distance is identified for each plane. If

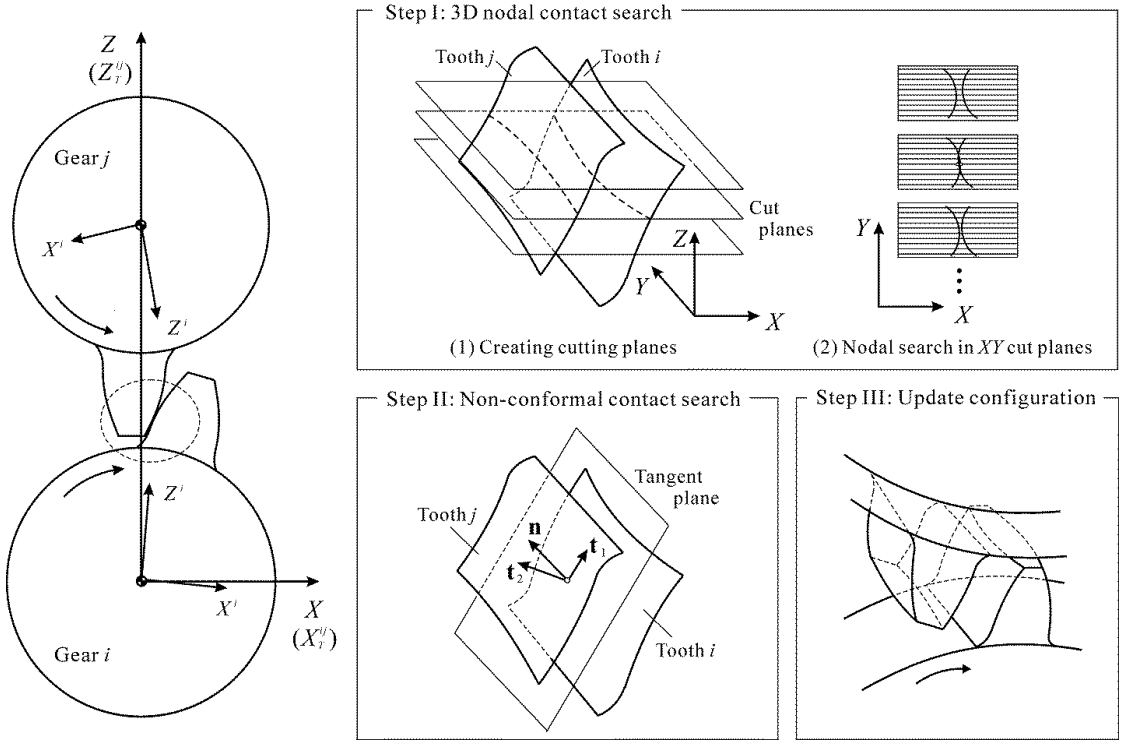

Fig 2.2 Combined nodal and non-conformal contact search for gear tooth

the distance is negative, the two surfaces at the nodal points are penetrated. If none of the minimum distances is negative, the pitch angle θ^j of gear *j* is incremented until the contact nodes with penetration are detected. Recall here that the pitch angle θ^i of gear *i* is prescribed by Eq. 2.12 at every step. Having determined the contact point (i.e., a pair of nodes in contact on body *i* and *j*), the surface parameters associated with these nodes are obtained and used as initial estimates for the interactive solution procedure for the non-conformal contact search equations given by Eqs. 2.10, 2.11 and 2.12. The accuracy of the contact point and the computational effort in the nodal search stage depends on the resolution of the nodal surface discretization. However, the contact point obtained by the nodal search is not used as the final solution, but rather used as the initial estimates for the iterative solution procedure, thus one can use relatively coarse mesh.

2.4 Numerical Procedure in Dynamic Simulation

2.4.1 Tabular Contact Search in Dynamic Simulation

In the contact geometry analysis discussed in the previous section, the global coordinate system is defined such that: (1) the origin of the coordinate system is attached to the center of the gear body *i*; (2) the global *Y*-axis is parallel to the axis of spin rotation of gear body *i*; and (3) the global *Z*-axis passes through the center of gear body *j* as shown in Fig. 2.2. In other words, the generalized coordinates stored in the look-up contact tables are defined with respect to this coordinate system introduced in the contact geometry analysis. For this reason, the generalized coordinates of gear bodies defined in the dynamic simulation need to be transformed to those consistent with the contact geometry analysis and then the look-up contact table needs to be utilized with the transformed generalized coordinates. Hereinafter, this coordinate system is called the look-up table coordinate system. The orientation of the look-up table coordinate system $\mathbf{A}_T^{ij} = [\mathbf{i}_T^{ij} \quad \mathbf{j}_T^{ij} \quad \mathbf{k}_T^{ij}]$ for gear body *i* and *j* is defined by the following three unit vectors:

$$\mathbf{i}_T^{ij} = \mathbf{j}_T^{ij} \times \mathbf{k}_T^{ij}, \quad \mathbf{j}_T^{ij} = \mathbf{j}^i, \quad \mathbf{k}_T^{ij} = \frac{\mathbf{R}^j - \mathbf{R}^i}{\left|\mathbf{R}^j - \mathbf{R}^i\right|} \tag{2.13}$$

where $\mathbf{j}^i$ is the unit vector along the *Y*-axis (spin axis) of the body coordinate system of gear body *i*. The orientation matrices of gear *i* and *j* defined with respect to the look-up table coordinate system are defined as

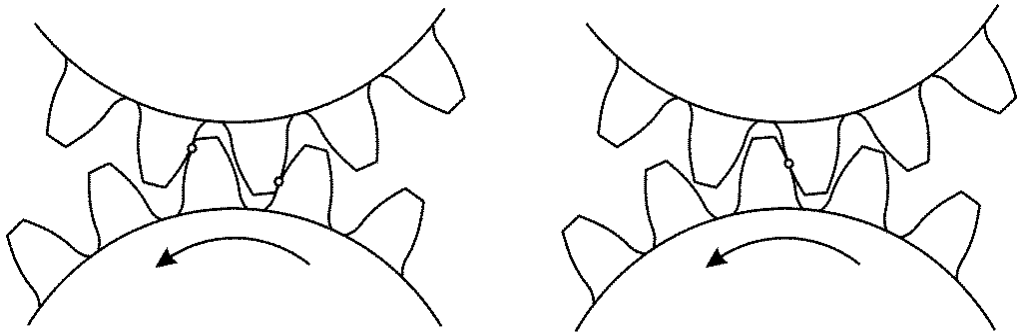

(a) Multi-point contact (b) Back-side contact

Fig 2.3. Contact scenario

$$\hat{\mathbf{A}}^i = (\mathbf{A}_T^{ij})^T \mathbf{A}^i \quad \text{and} \quad \hat{\mathbf{A}}^j = (\mathbf{A}_T^{ij})^T \mathbf{A}^j \tag{2.14}$$

from which, one can extract Euler angels $\hat{\boldsymbol{\theta}}^i = [\hat{\psi}^i \quad \hat{\phi}^i \quad \hat{\theta}^i]^T$ and $\hat{\boldsymbol{\theta}}^j = [\hat{\psi}^j \quad \hat{\phi}^j \quad \hat{\theta}^j]^T$ defined with respect to the table coordinate system used for the tabular interpolation. The three translational coordinates that defines the origin of the body coordinate system can also be defined in the look-up table coordinate system as follows:

$$\hat{\mathbf{R}}^i = \mathbf{0} \quad \text{and} \quad \hat{\mathbf{R}}^j = \mathbf{R}^j - \mathbf{R}^i \tag{2.15}$$

from which, the six coordinates of gear body *i* and *j* used for the tabular contact search in the dynamic simulation are defined as follows:

$$\hat{\mathbf{q}}^i = [(\hat{\mathbf{R}}^i)^T \quad (\hat{\boldsymbol{\theta}}^i)^T]^T \quad \text{and} \quad \hat{\mathbf{q}}^j = [(\hat{\mathbf{R}}^j)^T \quad (\hat{\boldsymbol{\theta}}^j)^T]^T \tag{2.16}$$

The preceding sets of coordinates are consistent with the generalized coordinates stored in the look-up contact tables. The tabular contact search is then carried out for all the gear teeth positioned in the searching range given in the look-up table tooth by tooth. This allows for detecting multi-point contact as shown in Fig. 2.3(a) without ad hoc procedures. The contact point on the back side of the tooth as shown in Fig. 2.3(b) can also be considered by switching the look-up table with that of the back-side contact in a straightforward manner.

2.4.2 Numerical Procedure for Planetary Gear System

To demonstrate the use of the tabular contact search method for complex geared systems, the numerical procedure for a planetary gear model that consists of three planet gears (bodies 1 through 3), one ring gear (body 4), one sun gear (body 5) and one carrier (body 6) shown in Fig. 2.4 is discussed in this sub-section. The ring gear is fixed to the ground and the carrier is connected to the centers of the three planet gears by revolute joints. The carrier is assumed to rotate at a constant speed by imposing a driving constraint.

In this planetary gear model, look-up tables for (1) the ring and planet gear teeth; and (2) the planet and sun gear teeth are prepared prior to the dynamic simulation. For each gear tooth contact, a contact table for the back-side tooth surface contact is also prepared if the backlash effect is considered in the dynamic simulation. To determine contact points using look-up contact tables at every time step, the look-up table coordinate system is defined as shown in Fig. 2.4 for each pair of gears in a way described in Section 2.4.1. As shown in Fig. 2.4, the look-up table coordinate systems defined for the planet and ring gears and the planet and sun gears coincide since centers of the ring and sun gears coincide. The look-up table coordinate system rotates about its *Y*-axis as the planet gear rotates around the sun gear.

In what follows, the numerical procedure in the dynamic simulation is summarized.

Step 1: For each pair of gears, the look-up table coordinate system is defined at the current configuration and the generalized coordinates of gear bodies defined with respect to the look-up table coordinate system $\hat{\mathbf{q}}$ are calculated.

Step 2: Using the rotational coordinates defined with respect to the look-up table coordinate system, the angular position of the gear tooth profile coordinate system positioned in the tabular search range is determined with respect to the look-up table coordinate system at the current configuration. In Fig. 2.5, the three teeth, *k*, *k*+1, and *k*+2 are positioned in the tabular search range, and the rotation angles $\theta_p^{14,k}$, $\theta_p^{14,k+1}$, and $\theta_p^{14,k+2}$ of the tooth profile coordinate systems are defined, where the superscript 1 indicates the body number of the planet gear, while superscript 4 indicates that of the ring gear.

Step 3: Using the rotation angle of the tooth profile coordinate system *k* defined with respect to the look-up table coordinate system, the tabular contact search is performed to determine the location of the contact point (i.e., surface parameters) and the geometric

properties at the contact point. The same procedure is repeated for all the teeth in the tabular search range (i.e., tooth *k*+1 and *k*+2 in the model shown in Fig. 2.5).

Step 4: If the tooth under consideration has a tooth geometry imperfection, the look-up table is switched to that accounts for the tooth geometry imperfection.

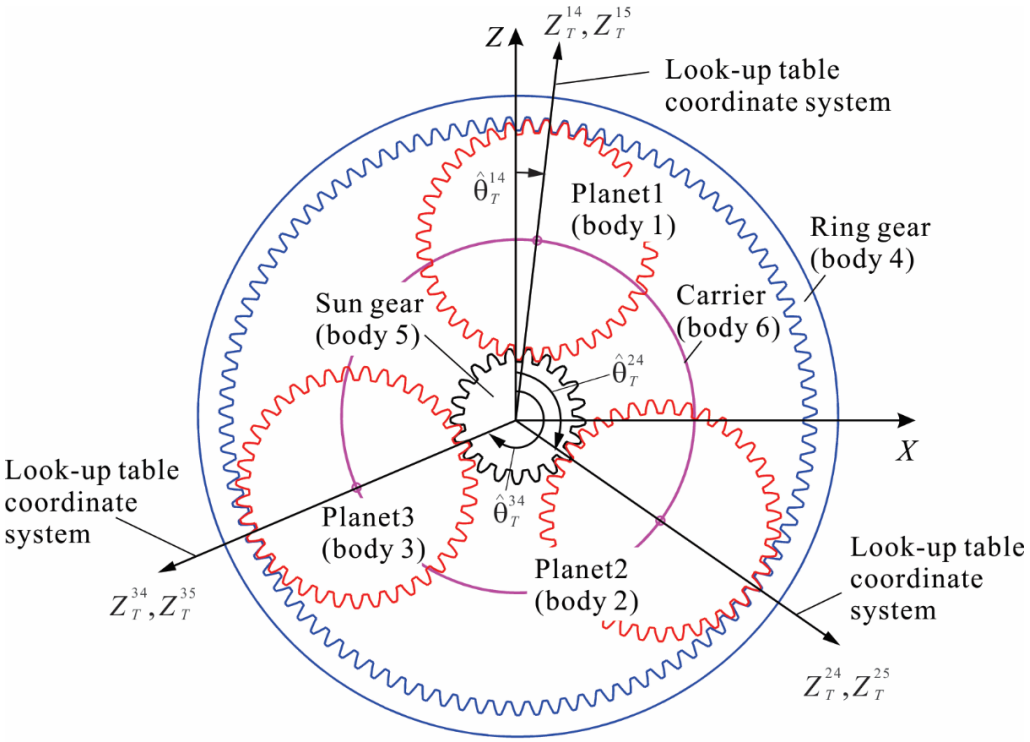

Fig 2.4. Look-up table coordinate systems of planetary gear

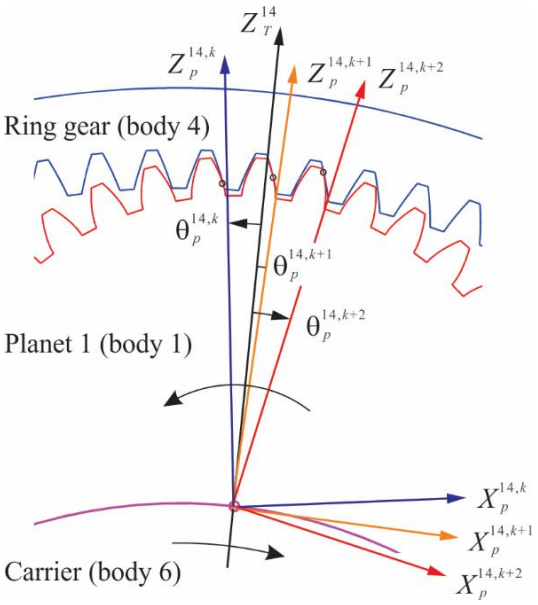

Fig 2.5. Tooth profile coordinate system of planet and ring gears

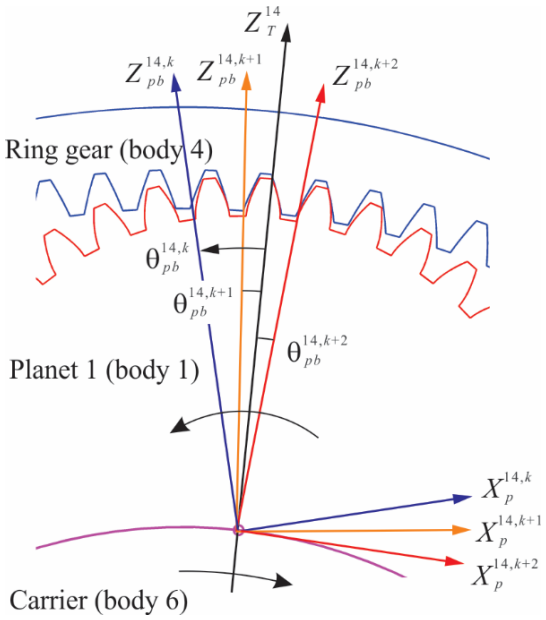

Fig 2.6. Back-side tooth profile coordinate system of planet and ring gears

Step 5: If the back-side tooth surface contact is considered, the angular position of the back-side tooth profile coordinate systems positioned in the tabular search range is determined (i.e., $\theta_{pb}^{14,k}$, $\theta_{pb}^{14,k+1}$, and $\theta_{pb}^{14,k+2}$ in the model shown in Fig. 2.6). These rotation angles are used to determine whether the back-side tooth surface contact occurs or not. The look-up contact tables for the back-side contact are used to determine the location of the contact point and the geometric properties at the contact point. That is, the backlash effect can be considered by simply switching the look-up contact tables.

Step 6: The normal and tangential contact forces are calculated using the procedure presented in Section 2.5 with the variable mesh stiffness model, and then the generalized mesh force vectors are evaluated.

Step 7: The same procedure from Step 1 to 6 is repeated for all the other pairs of gears in the system.

Step 8: The generalized mesh force vectors of all of the gear bodies under consideration are added to the generalized external force vector $\mathbf{Q}_e$ in the equations of motion of the multibody gear system defined as

$$\left.\begin{aligned} \mathbf{M}\ddot{\mathbf{q}} + \mathbf{C}_{\mathbf{q}}^{T}\boldsymbol{\lambda} &= \mathbf{Q}_{v} + \mathbf{Q}_{e} \\ \mathbf{C}(\mathbf{q}, t) &= \mathbf{0} \end{aligned}\right\} \tag{2.17}$$

where $\mathbf{C}$ is the vector of the system constraint equations that describe mechanical joints and/or specified motion trajectories, and $\mathbf{q}$ is the vector of the system generalized coordinates. $\mathbf{M}$ is the system mass matrix; $\mathbf{Q}_v$ is the vector of inertia forces that are quadratic in velocity; $\mathbf{Q}_e$ is the vector of the generalized external forces. $\mathbf{C}_{\mathbf{q}}$ is the Jacobian matrix of the constraint equations, and $\boldsymbol{\lambda}$ is the vector of Lagrange multipliers that are used to define the generalized constraint forces.

Step 9: The system equations of motion are integrated forward in time to determine the generalized coordinates and velocities using a time integration scheme for differential algebraic equations. Steps 1 to 9 are repeated until the simulation time is exceeded.

2.5 Gear Mesh Stiffness and Contact Forces

The normal contact force between two tooth surfaces is defined as

$$F_N^{ijk} = -k_N^{ijk}\delta^{ijk} - c_N^{ijk}\dot{\delta}^{ijk}\left|\delta^{ijk}\right| \tag{2.18}$$

where k_N^{ijk} is the mesh stiffness; c_N^{ijk} is the damping coefficient; δ^{ijk} is the penetration defined by $\delta^{ijk} = (\mathbf{r}^{ik} - \mathbf{r}^{jk}) \cdot \mathbf{n}^{jk}$; $\dot{\delta}^{ijk}$ is its velocity; and $\mathbf{n}^{jk}$ is the unit normal at the contact point defined in the global coordinate system. For an accurate prediction of the transmission error, which is the main source of noise and vibration of gear trains, the mesh stiffness needs to account for the effect of the contact stiffness, tooth bending stiffness, and gear body (foundation) stiffness [75]. Due to the non-uniform gear tooth thickness, tooth bending stiffness varies as the contact point move along its length. The compliance of gear tooth *i* can be modeled with the following series spring model

$$\frac{1}{k_N^{ik}} = \frac{1}{k_{N1}^{ik}} + \frac{1}{k_{N2}^{ik}} + \frac{1}{k_{N3}^{ik}} \tag{2.19}$$

In the preceding equation, the contact compliance is defined based on the semi-empirical Hertz contact model as [76]

$$\frac{1}{k_{N1}} = \frac{1.37}{(E_{eff})^{0.9}(b_{eff})^{0.8}(F_N)^{0.1}} \tag{2.20}$$

For simplicity, the superscripts *ik* that denote the body and contact numbers are omitted. In the preceding equation, b_{eff} is the effective face width; F_N is the normal load acting on the tooth face, E_{eff} is the effective Young's modulus determined by Young's modulus and the tooth width to thickness ratio [76].

The tooth bending stiffness is approximated by the non-uniform cantilevered beam of an effective length L_e discretized by transverse segments of rectangular cross section as shown in Fig. 2.7. The tooth bending compliance is expressed as [76]

$$\frac{1}{k_{N2}} = \sum_{i=1}^{Ns} (Q_{ti} + Q_{si} + Q_{mi}) \cos\beta \tag{2.21}$$

where *Ns* is the number of the discretized segments and β is the pressure angle at the contact point. The tooth stiffness associated with the transverse normal, transverse shear and bending deformations are considered in the preceding expression by the compliance Q_{ti}, Q_{si} and Q_{mi} for segment *i*, respectively. These compliances are defined as [76]:

$$Q_{ti} = \frac{\cos\beta}{6E_{eff}\bar{I}_i}(2(L_i)^3 + 3(L_i)^2 S_i) \tag{2.22}$$

$$Q_{si} = \frac{1.2L_i \cos\beta}{G\bar{A}_i} \tag{2.23}$$

$$Q_{mi} = \frac{(S_i \cos\beta - Y \sin\beta)}{2E_{eff}\bar{I}_i}((L_i)^2 + 2L_i S_i) \tag{2.24}$$

where L_i, $\bar{I}_i$ and $\bar{A}_i$ are the thickness, the mean second moment of area, the mean cross-section area of segment *i*, respectively. S_i is the distance between the segment *i* and the contact point, *G* is the shear modulus of rigidity.

The third factor that contributes to the mesh stiffness is the foundation stiffness of the gear tooth. The foundation compliance is defined as follows [75]:

$$\frac{1}{k_{N3}} = \frac{\cos^2\beta}{bE}\left(L\left(\frac{L_f}{H_f}\right)^2 + M\left(\frac{L_f}{H_f}\right) + P(1 + Q\tan^2\beta)\right) \tag{2.25}$$

where *b* is the tooth face width, *E* is Young's modulus, L_f is the effective tooth length, and H_f is the effective tooth thickens. The coefficients *L*, *M*, *P* and *Q* in the preceding

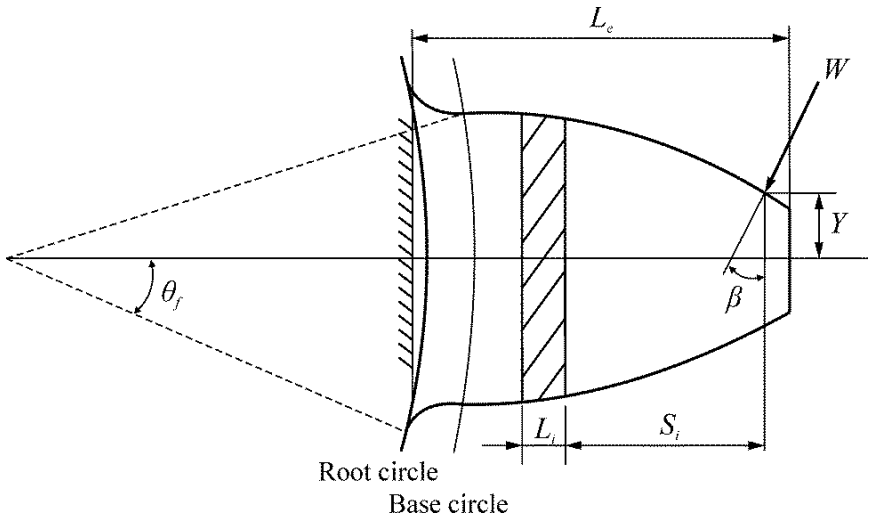

Fig 2.7. Tooth compliance model

equation, based on the semi-infinite elastic plane assumption, are given in Table 2.1 [75].The semi-analytical formula for the gear body rotational stiffness for an elastic ring model, on the other hand, is derived in the literature [77]. In this case, the four coefficients *L*, *M*, *P* and *Q* in Eq. 2.25 are defined by the following polynomial in terms of angle θ_f as shown in Fig. 2.7:

$$X(\theta_f, h_f) = a_1 \frac{1}{(\theta_f)^2} + a_2 (h_f)^2 + a_3 \frac{h_f}{\theta_f} + a_4 \frac{1}{\theta_f} + a_5 h_f + a_6 \tag{2.26}$$

where the polynomial coefficients a_i $(i = 1, \cdots, 6)$ defined for *L*, *M*, *P* and *Q* are given in Table 2.2 [77], and h_f is the ratio of the radius of the root circle to the inside radius of the gear body.

Table 2.1 Coefficients *L*, *M*, *P* and *Q* for semi-infinite elastic plane assumption model [75]

	Narrow tooth ($R > 5$)	Wide tooth ($R < 5$)
L	5.306	$5.306(1-\nu^2)$
M	$2(1-\nu)$	$2(1-\nu-2\nu^2)$
P	1.534	$1.534(1-\nu^2)$
Q	$0.4167/(1+\nu)$	$0.4167/(1+\nu)$

* $R = b / H_p$ (*b*: tooth width, H_p: tooth thickness at the pitch point)

Table 2.2 Polynomial coefficients *L*, *M*, *P* and *Q* for an elastic ring model [77]

	a_1	a_2	a_3	a_4	a_5	a_6
L	-5.574×10^{-5}	-1.9986×10^{-3}	-2.3015×10^{-4}	4.7702×10^{-3}	0.0271	6.8045
M	60.111×10^{-5}	28.100×10^{-3}	-83.431×10^{-4}	-9.9256×10^{-3}	0.1624	0.9086
P	-50.952×10^{-5}	185.50×10^{-3}	0.0538×10^{-4}	53.300×10^{-3}	0.2895	0.9236
Q	-6.2042×10^{-5}	9.0889×10^{-3}	-4.0964×10^{-4}	7.829×10^{-3}	-0.1472	0.6904

Using Eq. 2.20, 2.21 and 2.25, one can define the tooth compliance and then the total mesh stiffness at contact *k* between tooth *i* and *j* is defined as:

$$k_N^{ijk} = \frac{k_N^{ik} k_N^{jk}}{k_N^{ik} + k_N^{jk}} \tag{2.27}$$

from which, the normal contact force vector defined by Eq. 2.18 is expressed in the global coordinate system as follows:

$$\mathbf{F}_N^{ijk} = F_N^{ijk} \mathbf{n}^{jk} \tag{2.28}$$

In order to account for the effect of friction, the unit relative velocity vector along the tangent plane of contact can be determined as:

$$\mathbf{v}_T^{ijk} = \frac{\dot{\mathbf{r}}^{ijk} - (\dot{\mathbf{r}}^{ijk} \cdot \mathbf{n}^{jk})\mathbf{n}^{jk}}{\left|\dot{\mathbf{r}}^{ijk} - (\dot{\mathbf{r}}^{ijk} \cdot \mathbf{n}^{jk})\mathbf{n}^{jk}\right|} \tag{2.29}$$

where $\dot{\mathbf{r}}^{ijk}$ is the relative velocity vector at the contact point. Using an assumption of Coulomb friction, the friction force vector at the contact point can be defined as:

$$\mathbf{F}_F^{ijk} = -\text{sign}(\mathbf{v}_T^{ijk})\, \mu^{ijk} F_N^{ijk}\, \mathbf{v}_T^{ijk} \tag{2.30}$$

where μ^{ijk} is a coefficient of friction. For a more accurate prediction of tangential contact forces on lubricated tooth surfaces, one can use models based on elasto-hydrodynamic lubrication theory [78,79].

CHAPTER 3
NUMERICAL EXAMPLES OF GEAR DYNAMICS SIMULATION

3.1 Introduction

In this chapter, several numerical examples are presented in order to evaluate the accuracy and validity of the numerical procedure proposed for the gear dynamics simulation of multibody systems. In particular, an accuracy of mesh stiffness model introduced in this study and transmission error of a gear tooth with tip relief are discussed first. A planetary gear model is then introduced to discuss the effect of tooth surface irregularity on mesh force variation. A wind turbine drivetrain model is presented in the last example and is validated against test data provided in the literature.

3.2 Mesh Stiffness Model

In the first numerical example, the accuracy of the mesh stiffness model presented in Section 2.5 is discussed. The specification of the spur gear and pinion models considered in this example is summarized in Table 3.1 [80]. The tooth and mesh stiffness evaluated using Eqs. 2.18 and 2.26 are presented in Fig. 3.1 as a function of the pinion rotation angle. In this figure, the rotational gear body stiffness based on the semi-infinite elastic plane assumption, defined as Model 1 (see Table 2.1), and the elastic ring model, defined as Model 2 (see Table 2.2), are used for comparison. The tooth and mesh stiffness obtained using the finite element model created by ANSYS^{TM} are also presented in this figure. The eight-node hexahedral and six-node pentahedron elements are used with the augmented Lagrangian method for modeling gear tooth contact. The element is carefully refined around the contact region to ensure the accuracy as shown in Fig.3.2. The external torque of 3500 Nm is assumed.

It is observed from Fig.3.1 that use of the elastic ring rotational stiffness model (Model 2) leads to good agreement with the finite element solution, while Model 1 with the semi-infinite elastic plane assumption overestimates the tooth stiffness. In particular, error in the gear tooth is larger than that of the pinion gear due to the larger ratio of the root circle to the inside radii of the gear body.

Table 3.1 Specification of the spur gear model

	Gear	Pinion
Number of teeth	82	23
Module (mm)	8.5	
Tooth width (mm)	170	186
Inside diameter (mm)	240	100
Root diameter (mm)	675.75	174.25
Applied torque (Nm)	3500	

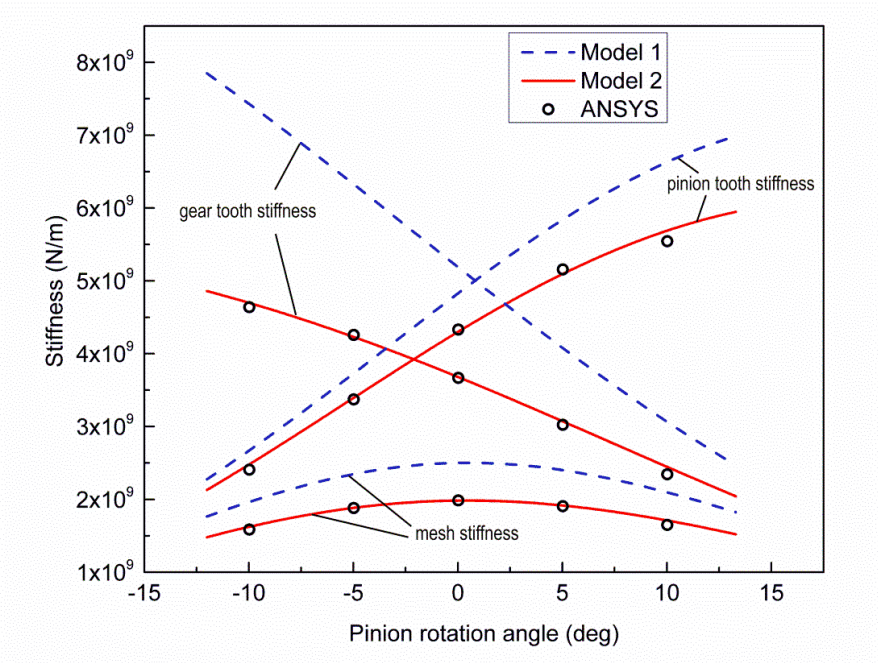

Fig 3.1. Tooth and mesh stiffness

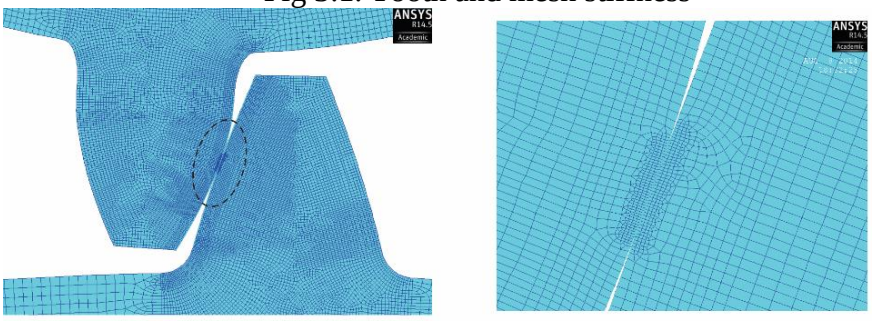

(a) Gear tooth mesh (b) Mesh around contact region

Fig 3.2. Finite element tooth contact model

3.3 Transmission Error of Spur Gear Teeth with Tip Relief

In this example, the transmission error of the gear tooth with tip relief is evaluated using the procedure developed in this study. The transmission error is defined by the deviation of the theoretical angular position of a pair of gears from its actual position at a constant steady rotation and is the main source of gear noise and vibration. To reduce the transmission error at an operating torque, the tip relief is introduced. The linear tip relief, as shown in Fig. 3.3, is defined by the following equation:

$$\delta(r) = \delta_a \frac{r - r_s}{r_a - r_s} \tag{3.1}$$

where r_s is the point that the tip relief starts and its end point is defined by r_a. The amount of tip relief at the end point is defined by δ_a.

To evaluate the transmission error with the linear tip relief, the specification of the spur gear and pinion in Houser et al. [81] is used in this study and summarized in Table 3.2, where the linear tip reliefs of the pinion and gear are assumed to be 12.7 μm and 10.16 μm, starting at the pitch point [81]. The peak to peak transmission errors (PPTEs) with and without the tip relief are compared in the Fig. 3.4. It is observed from this figure that V-pattern of the transmission error versus torque curve is predicted as presented in Houser et al. [81]. If the tip relief is not considered, the PPTE increases as the torque increases. In Fig.3.4, the lowest PPTE of 36.07 μin (0.9163 μm) is obtained for the external torque of 1550 lbs-in (175 Nm), which are in good agreement with that of Houser et al. [81].

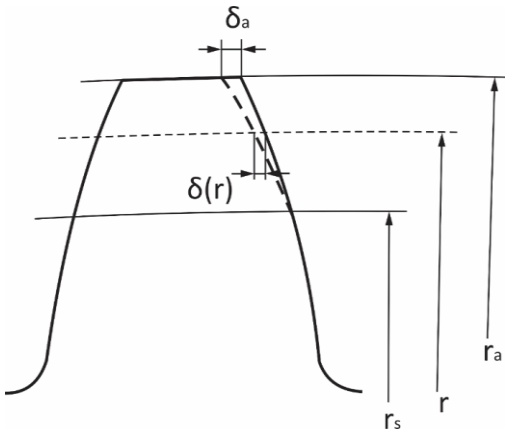

Fig 3.3. Tooth tip relief

Table 3.2 Specification of the spur gear model with tip relief

Number of teeth	50	Outside diameter	156 mm
Gear ratio	1:1	Root diameter	141 mm
Center Distance	150 mm	Pitch diameter	150 mm
module	3 mm	Pinion tip relief *	12.7 μm
Pressure angle	20 deg	Gear tip relief *	10.16 μm

* The tip relief starts at the tooth pitch point (r = 75mm)

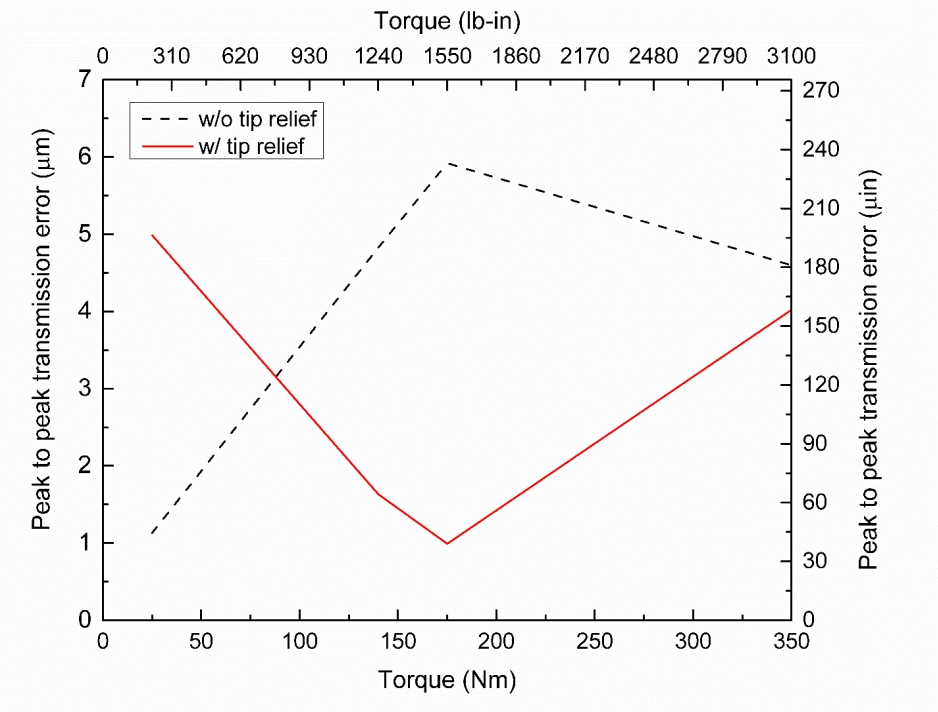

Fig 3.4. Peak to peak transmission error with and without tip relief

3.4 Dynamic Simulation for Planetary Gear with Tooth Surface Imperfection

In this example, a planetary gear model, which consists of three planet gears, is considered as shown in Fig. 3.5, and the specification is given in Table 3.3. In this model, a small tooth surface imperfection is considered in one of the planet gear teeth as shown in Fig.3.5 with H = 0.288 mm and W = 1.492 mm. All the look-up contact tables for the planet/ring gear teeth contact and planet/sun gear teeth contact are generated first using the

procedure discussed in Section 2.3, and these contact tables are used to predict the contact points in the planetary gear in the dynamic simulation. The change in the location of contact point between the planet gear tooth with the imperfection and the internal ring gear tooth is shown in Figs. 3.6 and 3.7. It is observed from these figures that the contact point moves along the line of action and then it deviates from the line of action after the contact point reaches the edge of the groove. A jump in contact point occurs from one edge to the other (see points A and B). This behavior is clearly observed in the surface parameter presented in Fig. 3.8 as a function of the planet gear rotation.

Table 3.3 Specification of the planetary gear model

Component	# of teeth	Pressure angle (deg)	Pitch diameter (mm)	Tooth width (mm)	Circular crowning (mm)
Sun	21	20	214.2	220	0.5
Planet	39	20	397.8	227.5	0.5
Ring	99	20	1009.8	230	0.5

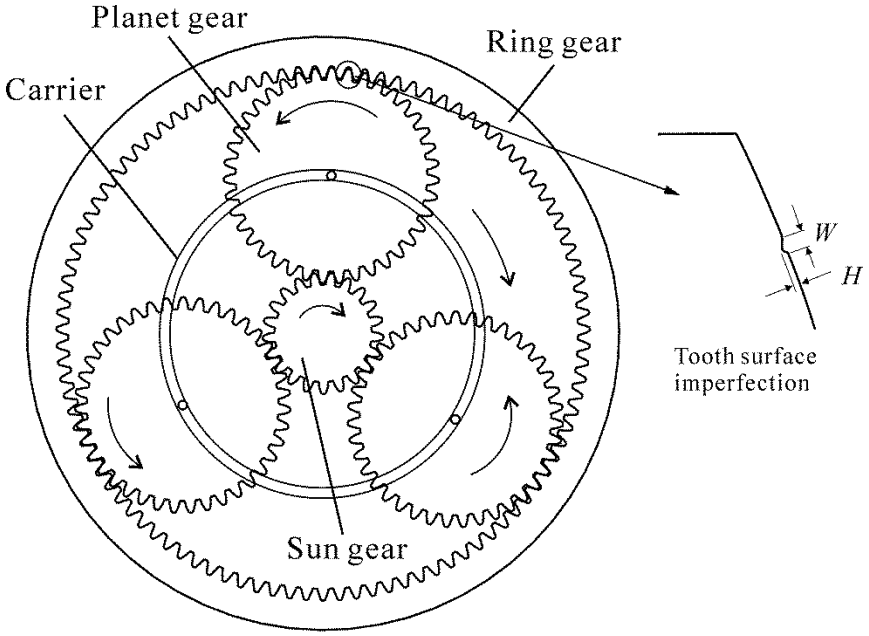

Fig 3.5. Planetary gear model with tooth surface imperfection

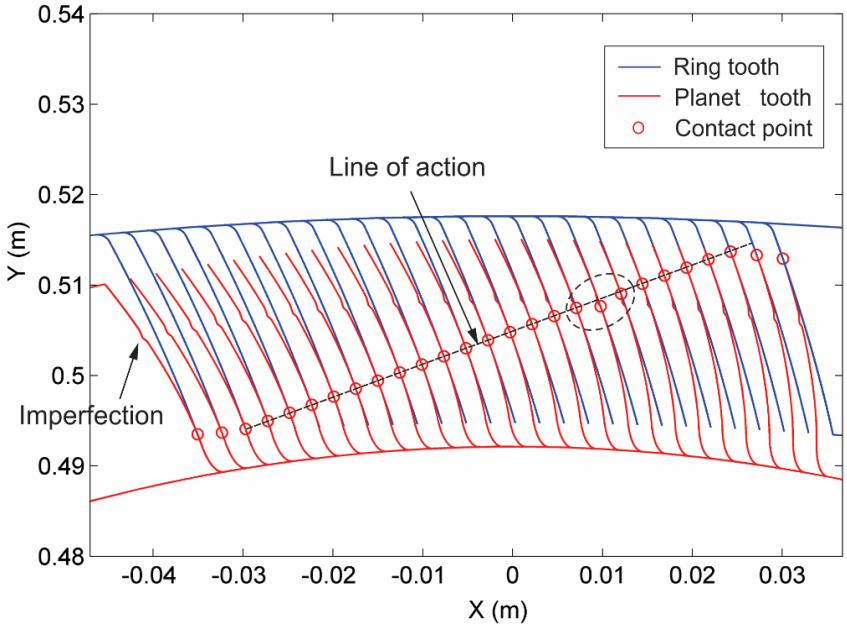

Fig 3.6. Location of contact point

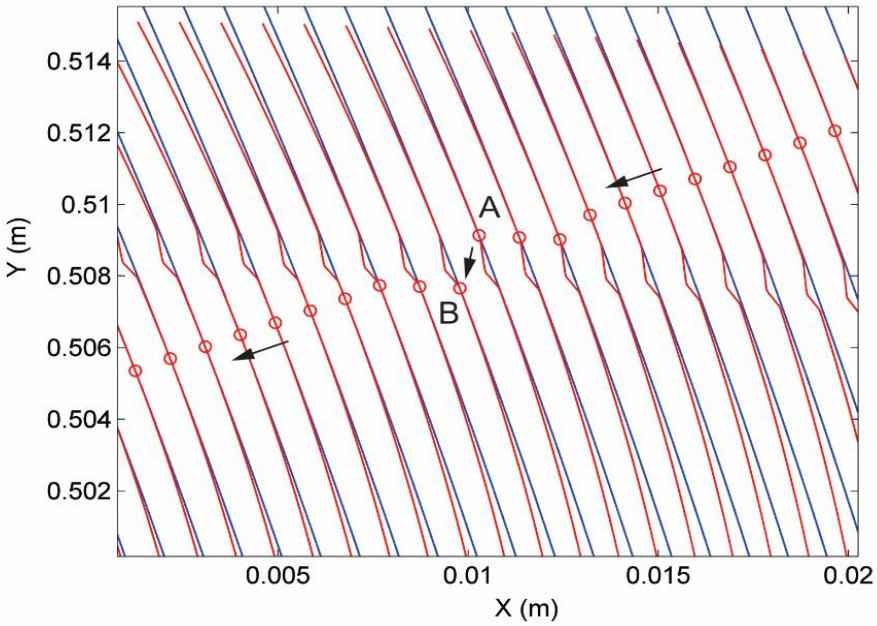

Fig 3.7. Jump in contact point around the surface imperfection

In order to discuss the performance of different contact search methods used in the contact geometry analysis, the accuracy and CPU time are compared and summarized in Table 3.4. The accuracy is measured by the norm of the non-conformal contact constraint violation for solutions obtained by each method and is defined by the following equation:

$$e = \left| \mathbf{C}^{ijk}(\mathbf{q}^i, \mathbf{q}^j, \mathbf{s}^{ik}, \mathbf{s}^{jk}) \right| \tag{3.2}$$

It is observed from this table that use of the nodal search method leads to extensive computational burden and violation of the non-conformal contact condition is noticeable, despite the fact that a very fine nodal discretization (10 μm) is used. Furthermore, the use of the nodal search method leads to discontinuous change in the contact point on the entire surface as shown in Fig. 3.8 and is not suited for an accurate prediction of mesh forces. On the other hand, the non-conformal contact search method failed to reach the convergent solution in the vicinity of the groove on the gear tooth surface, where a jump in contact point is supposed to occur.

The combined nodal and non-conformal contact search proposed in this study leads to accurate solutions with significantly less CPU time. This is attributed to the fact that the nodal search used in the vicinity of the groove allows for detecting the discontinuous change in the contact point, while the non-conformal contact search used in the region where the tooth surface is smooth and continuous leads to fast and accurate solutions. The contact point estimated by the nodal search method is refined using the non-conformal contact equation, thereby enforcing the non-conformal contact condition strictly at every configuration considered in the simulation scenario. It is important to notice here that use of relatively coarse nodal discretization (250 μm) leads to less CPU time while keeping the same order of accuracy, leading to a robust contact detection algorithm which allows for not only detecting the discontinuous change in the contact point, but also the smooth change in the contact point before/after the jump in contact point as shown in Fig. 3.8.

Using the multiple look-up contact tables prepared prior to the dynamic simulation that include the one considering the planet/ring teeth contact with the imperfection, the dynamic simulation is performed. The look-up table needs to be switched when the non-ideal planet tooth enter into the contact search region to consider the effect of the tooth surface imperfection in the mesh force calculation. It is important to notice here that the non-ideal planet gear tooth surface shown in Fig. 3.5 does not come into contact with the

sun gear since the other side of the ideal tooth surface comes into contact with the sun gear. The carrier is rotated at a constant angular speed of 25 deg/s and the mesh forces of all the planet/ring teeth contact as well as the planet/sun teeth contact are shown in Figs. 3.9 to 3.11. The results in Fig. 3.9 involve the tooth with the imperfection in one of the planet gear teeth. It is observed from Fig. 3.9 that the impulsive change in the mesh force occurs in the planet/ring gear teeth contact when the tooth with the surface imperfection comes into contact.

Table 3.4 Comparison of contact search methods

Contact search method	Nodal search	Non-conformal contact search	Combined nodal & non-conformal contact search (proposed)	
Distance between nodes (m)	1.00×10^{-5}	-	1.00×10^{-5}	2.50×10^{-4}
Maximum error (m)	5.85×10^{-4}	Not converged	4.36×10^{-12}	5.65×10^{-12}
CPU time (s)	20,520	Not converged	2,222	97

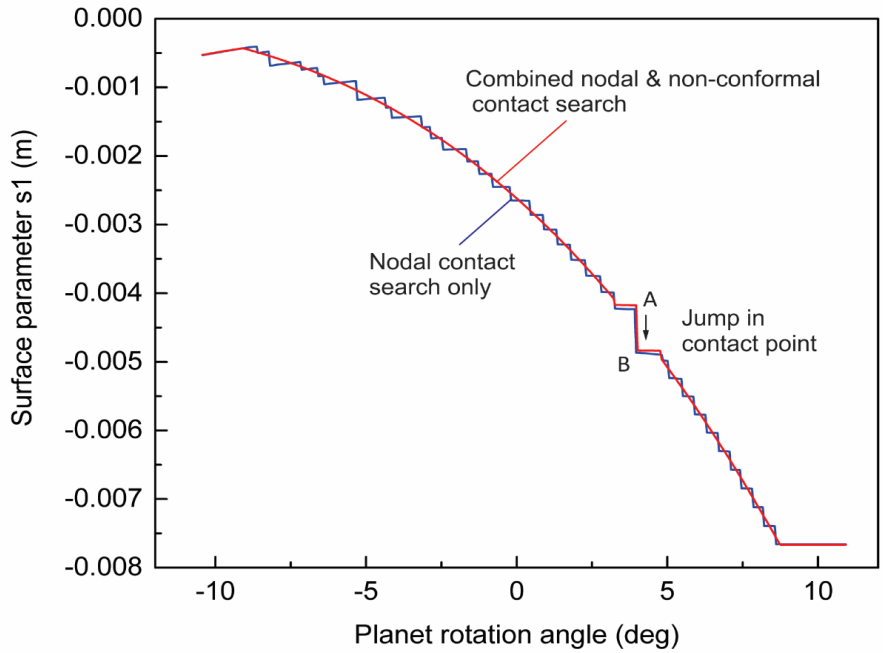

Fig 3.8. Location of contact point (s_1) as a function of rotation angle

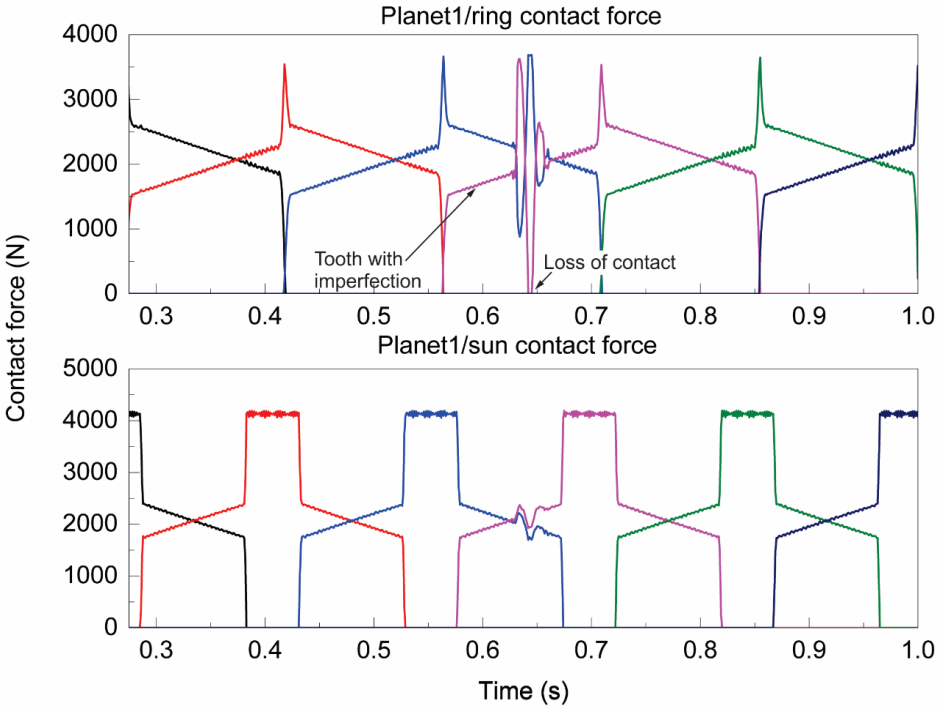

Fig 3.9. Mesh forces of planet-1/ring and planet-1/sun teeth contact with surface imperfection

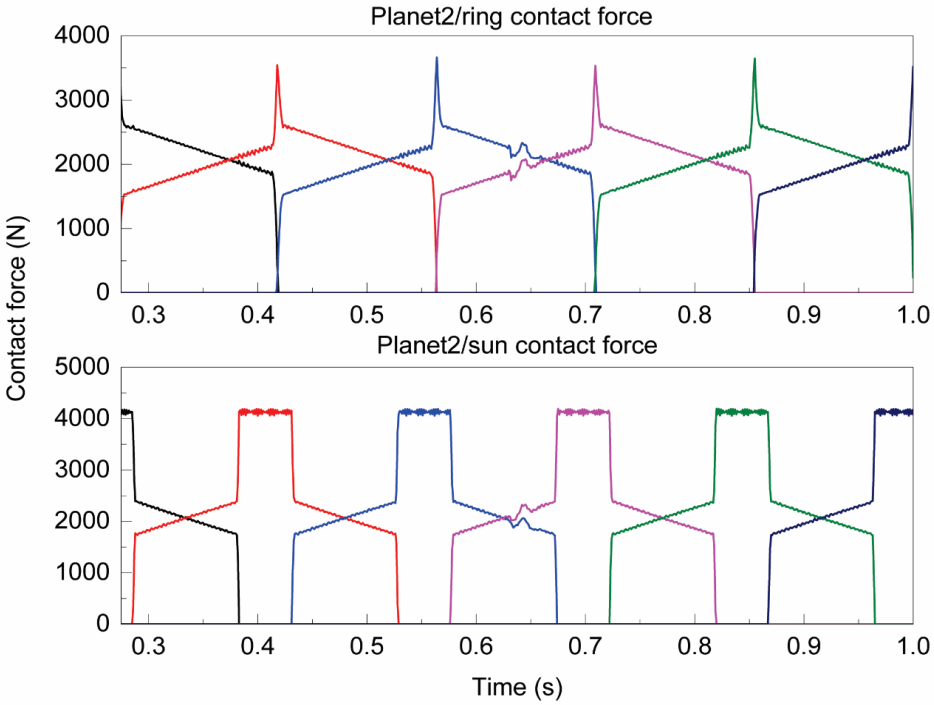

Fig 3.10. Mesh forces of planet-2/ring and planet-2/sun teeth contact

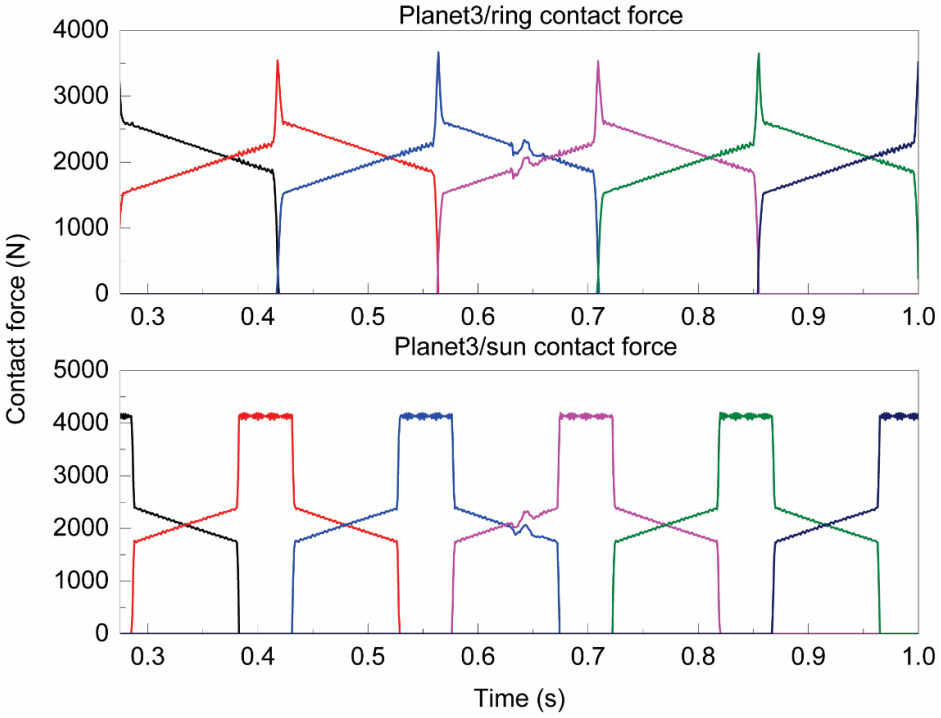

Fig 3.11. Mesh forces of planet-3/ring and planet-3/sun teeth contact

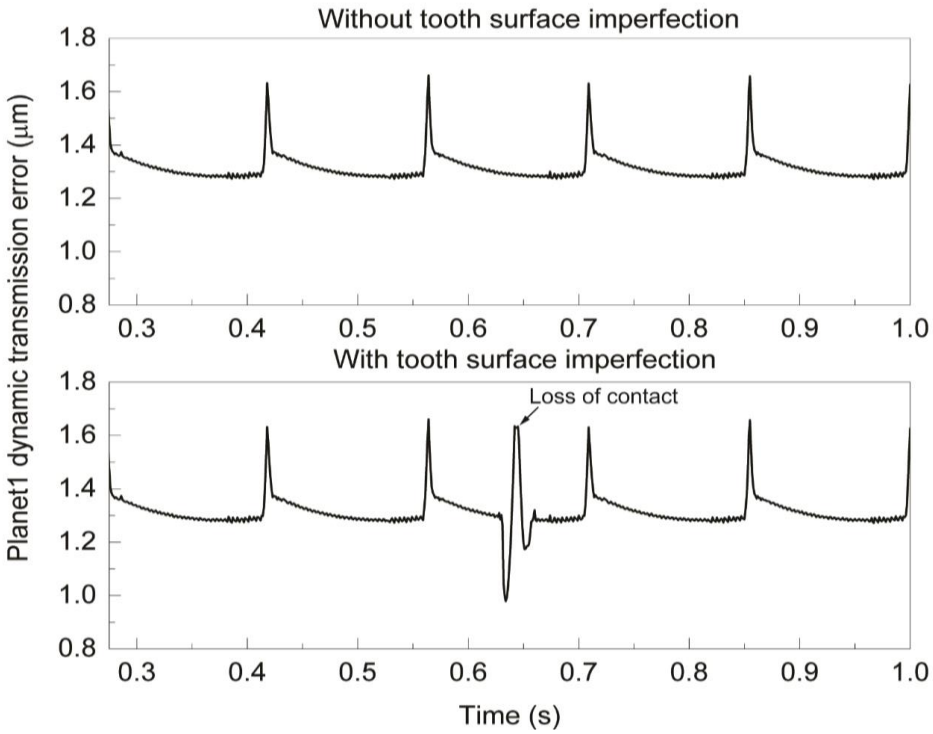

Fig 3.12. Dynamic transmission error of planet-1/ring teeth contact

In particular, a loss of the contact force is observed when the jump in contact point occurs, and it leads to an increase in the mesh force of the tooth next to the one with imperfection. The similar result is observed in the dynamic transmission error (DTE) presented in Fig. 3.12. In this figure, the dynamic transmission errors between the ring and planet gears with and without the tooth surface imperfection are compared. It is observed from this figure that the transmission error increases and its magnitude becomes same as that of the single point contact when the loss of contact due to the imperfection occurs. This is attributed to the fact that the double tooth contact is changed to the single tooth contact while the contact is lost. Furthermore, the change in the transmission error due to the mesh stiffness variation is also captured in both results. It is also important to notice here that the abrupt change in mesh force caused by the tooth surface imperfection influences the mesh force with the sun gear and a change in the mesh force is transmitted to the other two planet gears without tooth surface imperfections through the contact with sun gear as observed in Figs. 3.10 and 3.11.

3.5 Helical Gear Modeling and Verification

To model helical gear tooth contact in the gear dynamic simulation, the gear tooth is cut into a number of slices across the face width to describe the helix curve as shown in Fig. 3.13 and a point contact is defined on each sliced surface of a helical gear. By doing so, the load distribution across the face width of helical gears can be described as a collection of forces acting on the sliced tooth surfaces in a straightforward manner using a look-up contact table. The transverse module and transverse pressure angle for a helical gear are considered. Since the tooth surface is cut into a number of slices, tabular contact search is repeated for all the slices for one tooth surface in a way described in Section 2.4.2. It is important to notice here that the look-up coordinate system defined on sliced tooth needs to be rotated by $\Delta\theta$ from the one side to the other incrementally to account for the helix curve and $\Delta\theta$ is given by

$$\Delta\theta = \frac{B \cdot \cos\alpha_t \cdot \tan\beta_h}{n_s \cdot r_b} \tag{3.3}$$

where B is the face width, α_t is the transverse pressure angle, β_h is the helix angle, r_b is the base radius, and n_s is the number of slices. The helical gear mesh force distribution obtained using 21 slices is shown in Fig. 3.14.

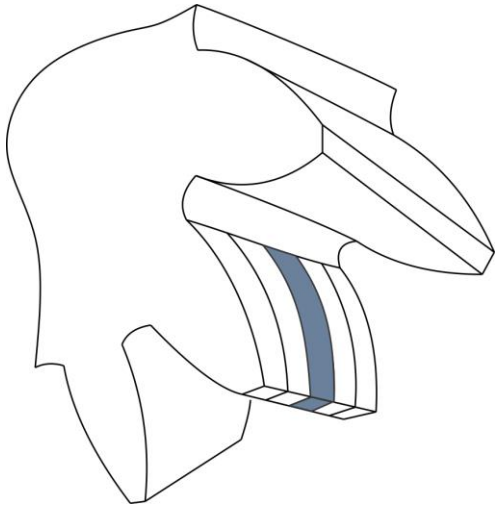

Fig. 3.13. Sliced helical gear tooth

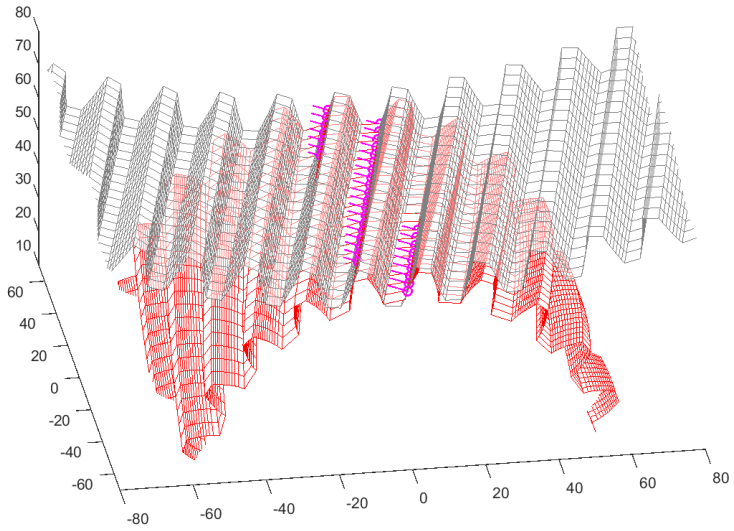

Fig. 3.14. Example of helical gear tooth mesh force distribution with 21 slices

Table 3.5 Basic gear geometry parameters

	No. of teeth	Normal module	Root diameter	Pressure angle	Helix angle	Face width	Center distance
Gear	39	10	372 mm	20°	7.5° L	220 mm	308 mm
Pinion	21	10	186 mm	20°	7.5° R	220 mm	

Table 3.6 Gear material properties

Young's modulus	210 GPa
Poisson ratio	0.3
Density	7850 kg/m^3

To verify the helical gear mesh model in the gear dynamics simulation, the mesh forces obtained using the present approach and the finite element model using ABAQUS are compared. The gear geometry parameters and material properties of the model under consideration are shown in Table 3.5 and 3.6, respectively. The CAD model of four-tooth gear and pinion as shown in Fig. 3.15 is generated using PTC-Creo and then imported into ABAQUS for the quasi-static contact analysis between the gear and pinon for various angular positions. The center of the pinion is rigidly fixed to the ground for a given pinion angle in each analysis, while the gear is allowed to rotate about the spin axis, about which a constant torque of 5122 Nm is applied to evaluate the mesh forces on the gear and pinion tooth surfaces. The mesh size of the finite element model is approximately 2.6 mm. The pinion rotational angle is incrementally changed from -16 deg to 16 deg with 2 deg increment as shown in Fig. 3.16. The resultant mesh force of one of the teeth in the pinion

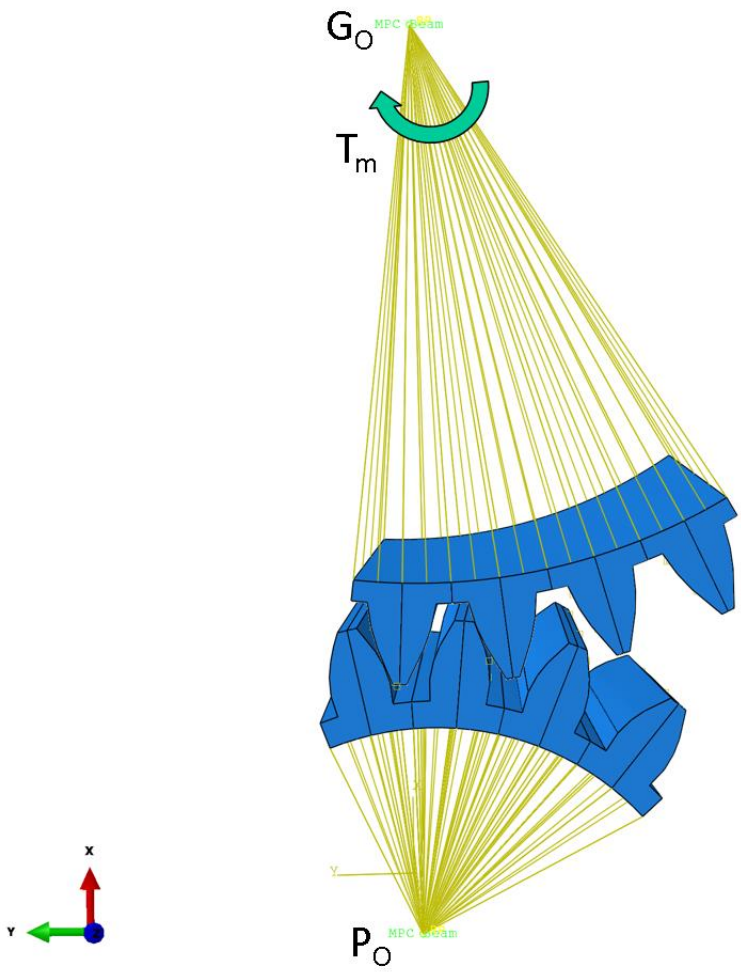

Fig. 3.15. Static gear teeth contact model

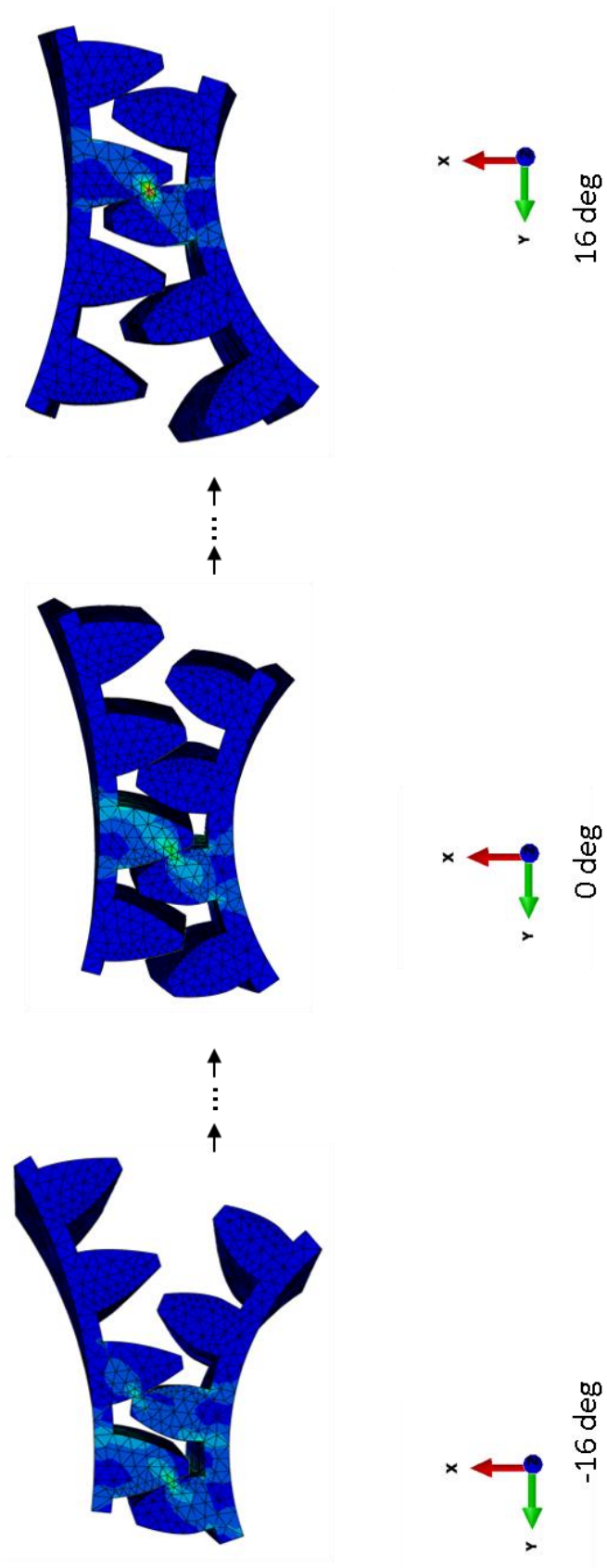

Fig. 3.16. ABAQUS FE model in different configurations

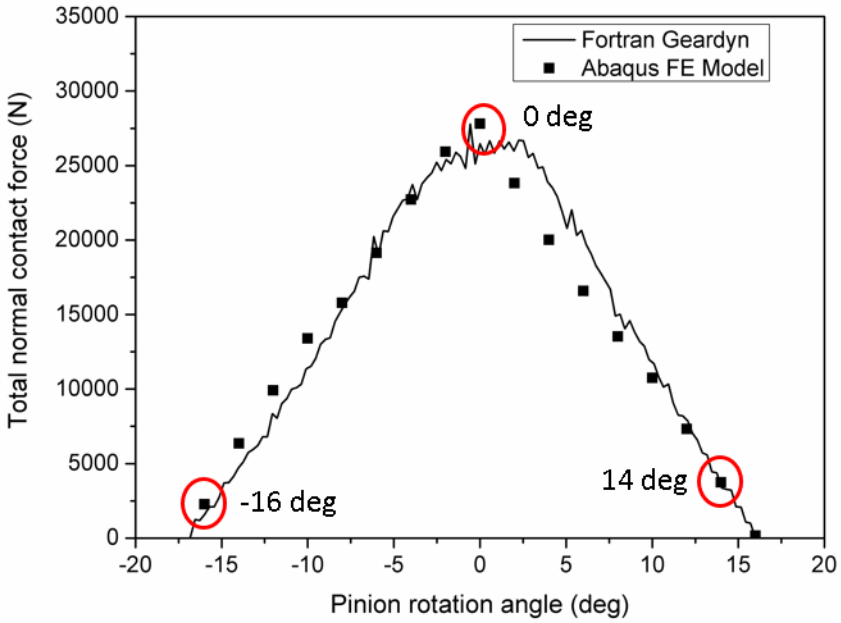

Fig. 3.17. Total contact force variation on pinion second tooth

at each configuration is presented in Fig. 3.17 and compared with the result obtained using the sliced helical gear model implemented in the gear dynamics simulation code. In the gear dynamics simulation, the pinion is rotated very slowly with the same driving torque as the finite element model. The gear and pinion teeth are cut into 21 slices. It is observed from Fig. 3.17 that the gear dynamics simulation results agree well with those of the ABAQUS model for various pinion angles. In order to compare the contact force distribution for different pinion angels, the mesh force distribution at -16, 0, and +14 degrees are compared with ABAQUS results in Fig. 3.18, Fig. 3.19, and Fig. 3.20, respectively. While only a single tooth is in contact at the pinion angle of 0 degree, two teeth are in contact at the pinon angle of -16 and +14 degrees. The similar mesh force distributions are obtained in both models for the three pinon angels.

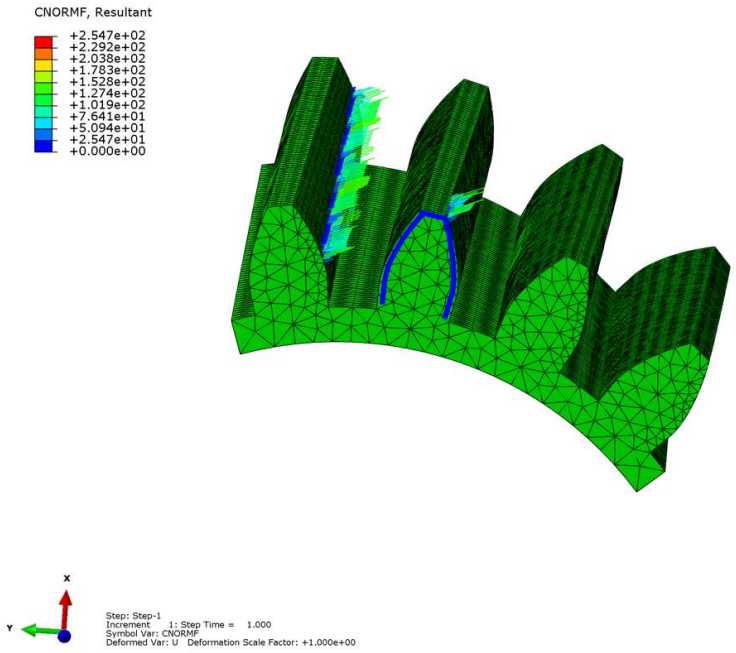

(a) ABAQUS FE model result

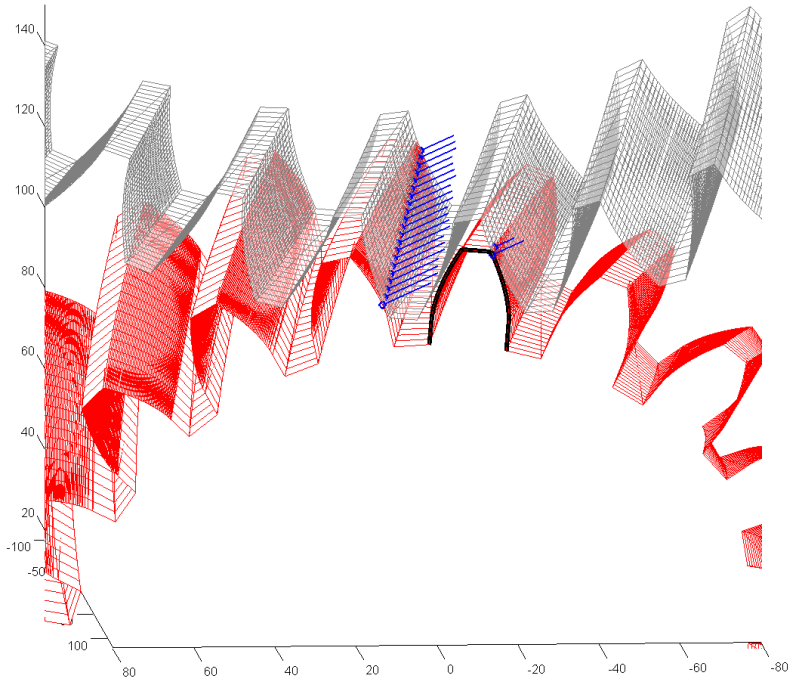

(b) FORTRAN Geardyn model result

Fig. 3.18.Contact force distribution at pinion configuration: -16 deg

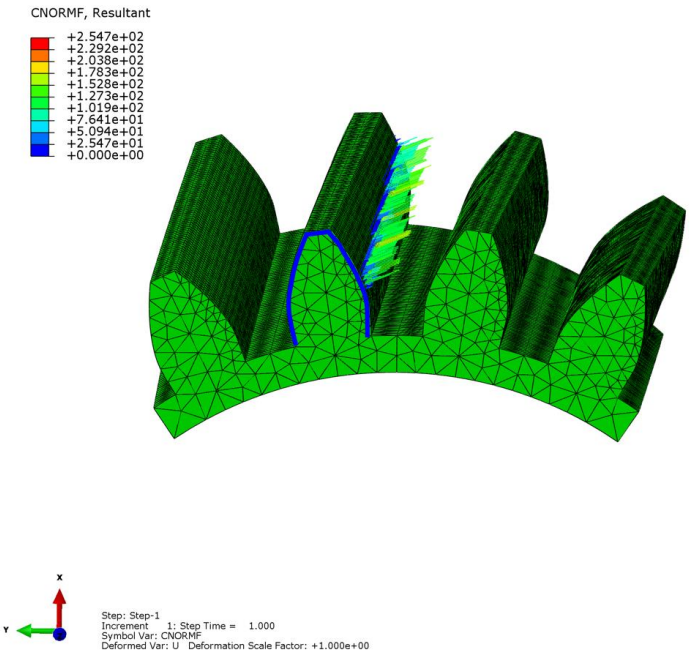

(a) ABAQUS FE model result

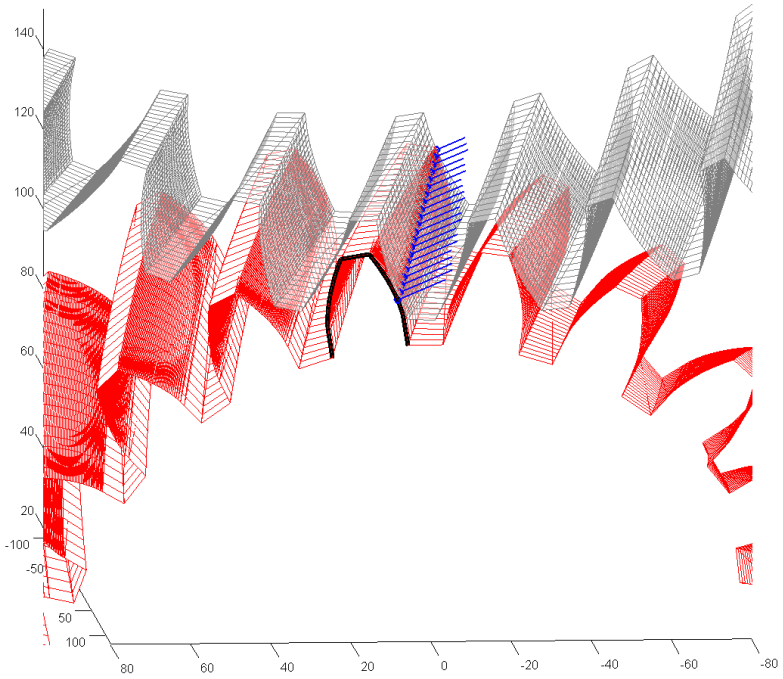

(b) FORTRAN Geardyn model result

Fig. 3.19.Contact force distribution at pinion configuration: 0 deg

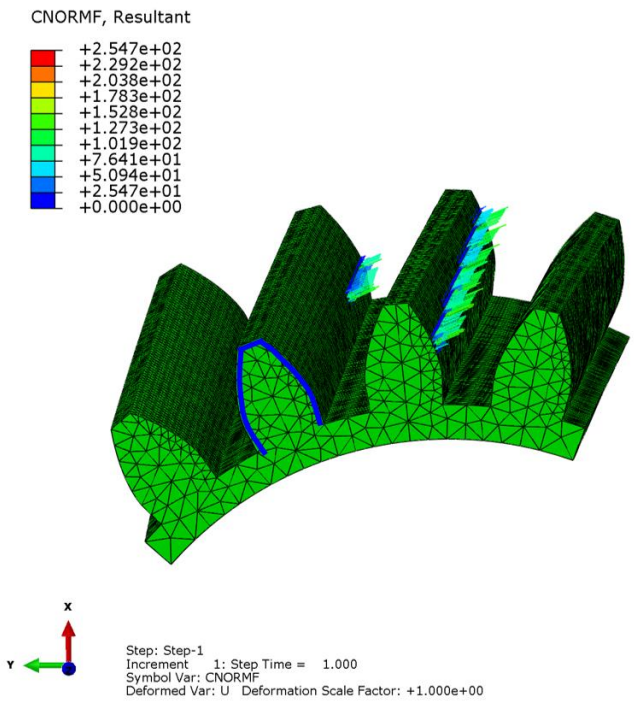

(a) ABAQUS FE model result

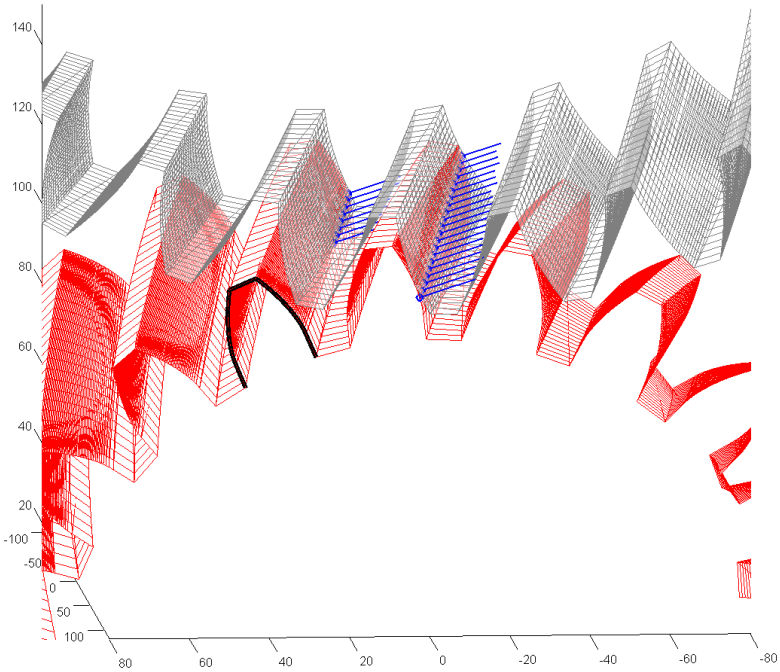

(b) FORTRAN Geardyn model result

Fig. 3.20.Contact force distribution at pinion configuration: 14 deg

3.6 Wind Turbine Drivetrain Model and Dynamic Simulation

In this section, a wind turbine drivetrain model utilized in the Gearbox Reliability Collaborative (GRC) project led by National Renewable Energy Laboratory (NREL) is developed, and the gear dynamics simulation capability developed for reliability-based design optimization of wind turbine drivetrains is demonstrated.

3.6.1 Wind Turbine Drivetrain Model and Specification

In the 750kW GRC wind turbine as summarized in Tables 3.7 [80], the drivetrain consists of one planetary gear at the low-speed stage and two parallel axis gears at the intermediate and high-speed stages as shown in Fig. 3.21. Planetary gear systems are commonly used in wind turbine drivetrains to provide high power density that can be achieved by sharing the large input torque by multiple planet-ring and planet-sun gear contact loads. In the low-speed stage of the GRC drivetrain, there are three planet gears framed on the carrier, which carries the input load from wind turbine rotor. The ring gear is fixed to the gear train housing. The sun gear is connected to the input shaft of the intermediate-speed stage parallel axis gear. The overall gear ratio of the GRC gear train is 81.49 [80]. Considering a lubricated gear toot surface condition, the coefficient of friction is assumed to be 0.04. The gear geometry parameters are summarized in Table 3.8 [80, 82]. The mass and inertia properties of the gears are presented in Table 3.9 [82] and the bearing stiffness are shown in Table 3.10 [82].

Table 3.7 General description of the wind turbine [80]

Type	Three blade up wind
Power rating	750 KW
Rotor diameter	48.2 m
Rated rotor speed	22 rpm
Power regulation	Stall
Aerodynamic brake	Pitchable tips
Tower	Welded tubular steel
Nominal hub height	55 m
Blade length	23.5 m

Table 3.7 Continued

Gearbox ratio	1:81.491
Gear teeth contact friction coefficient	0.04
Generator rotational speed at rated power	1809 rpm
Rated wind speed	16 m/s
Design life	20 years

Table 3.8 Basic wind turbine gear geometry parameters [80,82]

Components		No. of teeth	Normal module	Root diameter	Pressure angle	Helix angle	Face width
Low-speed stage	Ring gear	99	10	1047 mm	20°	7.5° L	230 mm
	Planet gear	39	10	372 mm	20°	7.5° L	227.5 mm
	Sun pinion	21	10	186 mm	20°	7.5° R	220 mm
Intermediate-speed stage	Gear	82	8.25	678 mm	20°	14° R	170 mm
	Pinion	23	8.25	174 mm	20°	14° L	186 mm
High-speed stage	Gear	88	5	440 mm	20°	14° L	110 mm
	Pinion	22	5	100 mm	20°	14° R	120 mm

Table 3.9 Mass and inertia properties of the planetary gears [82]

	Sun	Carrier	Planet	Ring	Housing
Mass (kg)	181.6	756.9	104.0	480.0	1213.0
I_{xx} (kgm^2)	1.26	59.1	3.20	144.2	340.0
I_{yy} (kgm^2)	24.0	60.3	2.04	75.4	554.4
I_{zz} (kgm^2)	24.0	60.3	2.04	75.4	424.8

Table 3.10 Bearing stiffness of the planetary gears [82]

	Carrier (Up)	Carrier (Down)	Planet
K_x (N/m)	1.0×10^{13}	1.0×10^{13}	1.0×10^{13}
K_y (N/m)	1.8×10^{9}	1.4×10^{9}	3.4×10^{9}
K_z (N/m)	1.8×10^{9}	1.4×10^{9}	3.4×10^{9}
$K_{\theta x}$ (Nm/rad)	0	0	0
$K_{\theta y}$ (Nm/rad)	5.5×10^{4}	2.7×10^{4}	5.3×10^{5}
$K_{\theta z}$ (Nm/rad)	5.5×10^{4}	2.7×10^{4}	5.3×10^{5}

NREL conducted field and dynamometer tests for the GRC wind turbine drivetrain [83] and the test data was used to evaluate the accuracy and computation efficiency of the gear train numerical models with different levels of fidelity. In the experimental test setup, the proximity and strain measurement sensors are placed on the planet rim and planet bearings to measure the planet gear motion and its bearing loads, respectively. More details on the test instrumentation can be found in the literature [83]. The test data was compared with simulation results obtained using drivetrain models with different fidelity. Those computational models include P1 and P2 models created by NREL's partners in industry and academia as well as M1A, M1B, M3B models created by NREL. The P1 model is a planetary stage multibody model and the gear face width is divided into nine force elements. The planet carrier and pins are modeled as flexible bodies. The P2 model is a quasi-static fully flexible model created using a software called RomaxWIND. The M1A and M1B models are rigid gear train models created by SIMPACK, where bearing clearance is considered in M1B model. The M3B model is a fully flexible multibody drivetrain model and the housing and carrier deformations are modeled using finite element software ABAQUS and then the reduced order modal models are imported into SIMPACK. Further details on the model description can be found in literature [83].

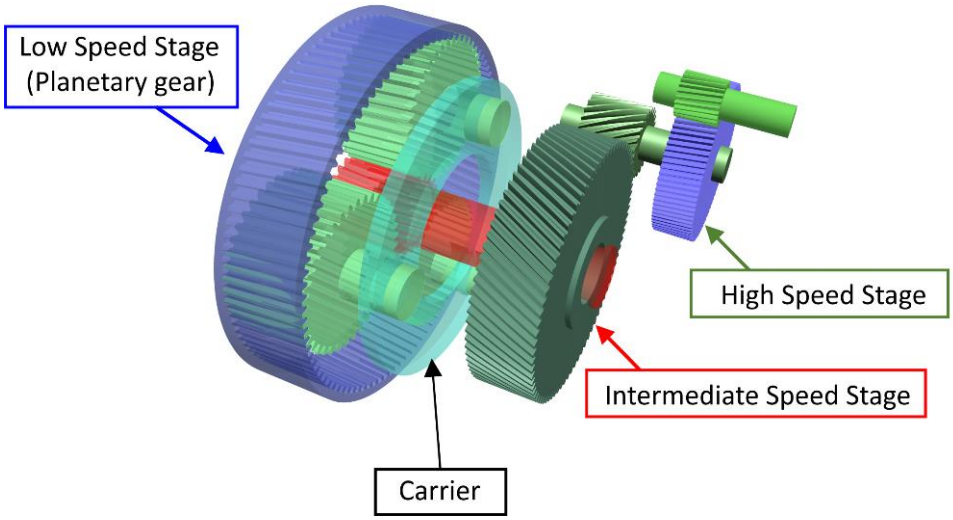

(a) Drivetrain components

(b) Drivetrain for dynamometer testing [82]

Fig. 3.21. GRC wind turbine drivetrain

3.6.2 Numerical Result and Validation against Test Data

To demonstrate the capability of the gear dynamic simulation program developed in this study using the tabular contact search method for complex multibody geared systems, some numerical examples are presented. The carrier is assumed to rotate at either a constant or variable speed by imposing a driving constraint and effect of gravity is considered in the dynamics simulation. To describe contact geometry of gear teeth in contact in the GRC drivetrain model, the following four look-up tables are generated prior to the gear dynamics simulation using the contact geometry analysis described in Section 2.3:

(1) ring-planet gear tooth contact;

(2) planet-sun gear tooth contact;

(3) pinion-gear tooth contact at the intermediate-speed stage;

(4) pinion-gear tooth contact at the high-speed stage.

In the first numerical example for the GRC wind turbine drivetrain, a rated constant angular velocity of 22 rpm is applied to the carrier of planetary gear at the low-speed stage, and the rotational resistance of the output shaft connected to the generator is modeled by a torsional damping (16.92 Nm/rad) at the high speed stage. There is no gear tooth profile modification (i.e., tip relief). A two-second simulation is carried out to discuss the mesh force variation. The contact forces between the planet and sun gears at time 0.99 s are shown in Fig. 3.22, where the length and direction of the arrow indicate the magnitude and direction of each contact force on the sliced tooth surface, respectively. The gear tooth is cut into 21 slices in this example. It is observed from this figure that the contact forces are distributed along the straight contact line across the face width and the angle between the contact line and spin axis corresponds to the helix angle.

Since the tooth surface is sliced to model gradual engagement between helical gears, the number of contact points on a tooth surface increases gradually from zero to the maximum number of slices, and then gradually decreases to zero for one mesh cycle. The total contact forces on the planet and sun gear tooth contact is shown in Fig. 3.23. It can be seen from this figure that two or three teeth are in contact alternately at the same time. Since the sun-planet gear contact ratio is 2.15, 2 or 3 pairs of teeth are always in contact as demonstrated in Fig. 3.23.

To discuss effect of the number of slices on the helical gear mesh force accuracy, the 21-slice model and the 11-slice model are compared. The contact forces acting on all of the slices on one tooth are shown in Fig. 3.24(a) for 21-slice model and in Fig. 3.25(a) for 11-slice model. It is observed from these figures that contact force taken by one slice is almost doubled in the 11-slice model, despite the fact that total mesh force are in good agreement as shown in Figs. 3.24(b) and 3.25(b). However, the contact force of 21-slice model is smoother than that of the 11-slice model as expected. The computational time of the 21-slice model is increased by 80 % as compared to the 11-slice model.

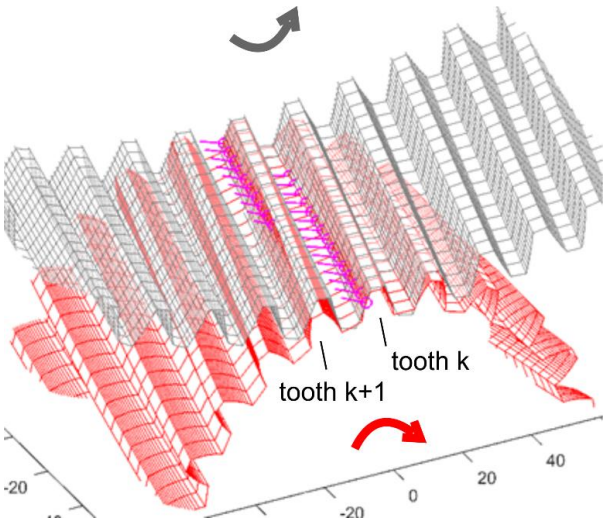

Fig. 3.22. Helical gear mesh force distribution

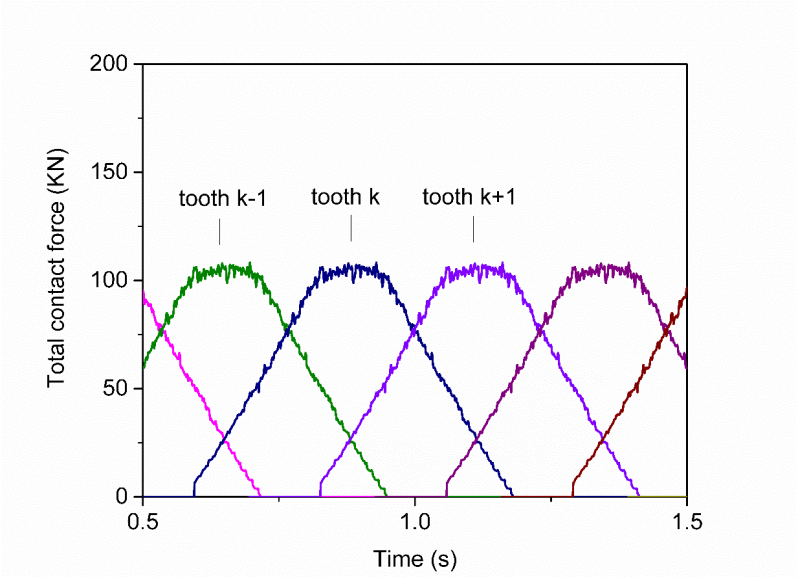

Fig. 3.23. Total contact force on planet and sun gear teeth

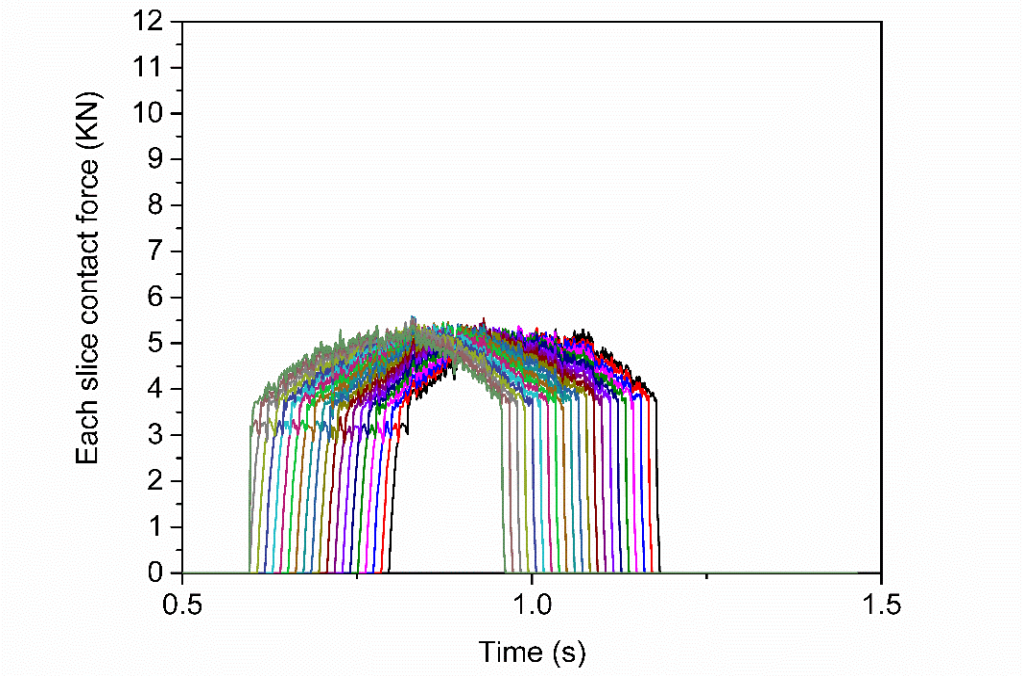

(a) Contact forces of 21-slice model on planet and sun gear tooth

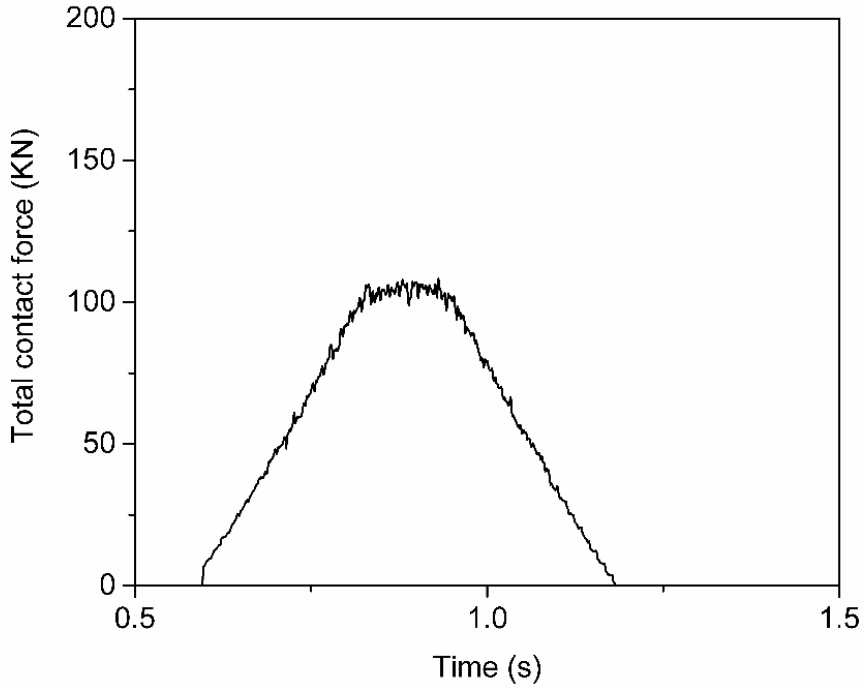

(b) Total contact force on planet and sun gear tooth for 21-slice model

Fig. 3.24. Contact force on planet and sun gear tooth for 21-slice model

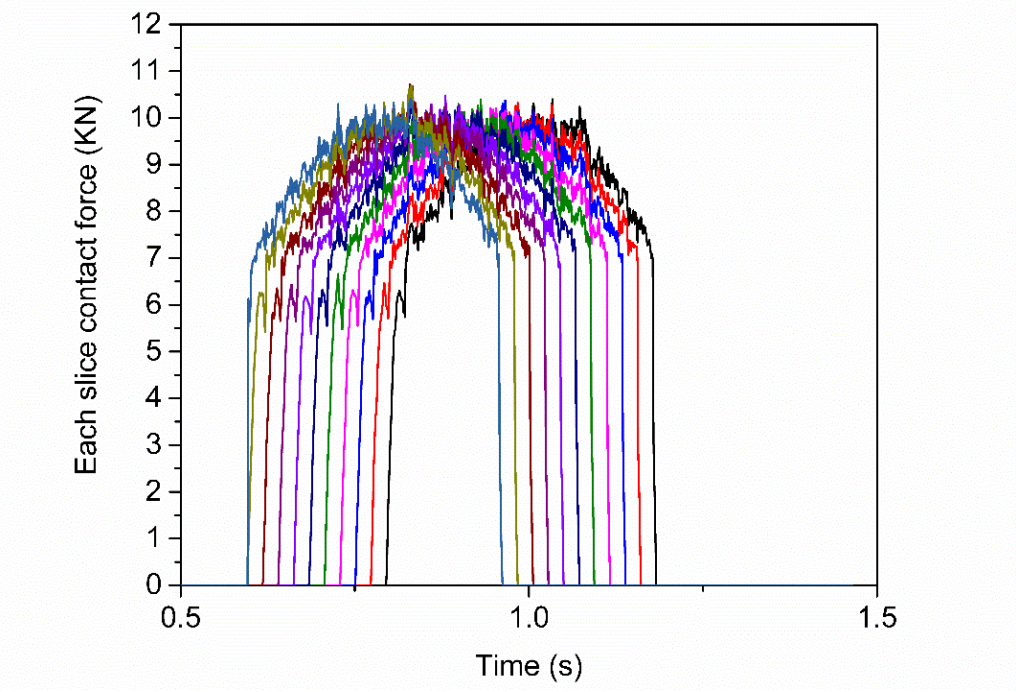

(a) Contact forces of 11-slice model on planet and sun gear tooth

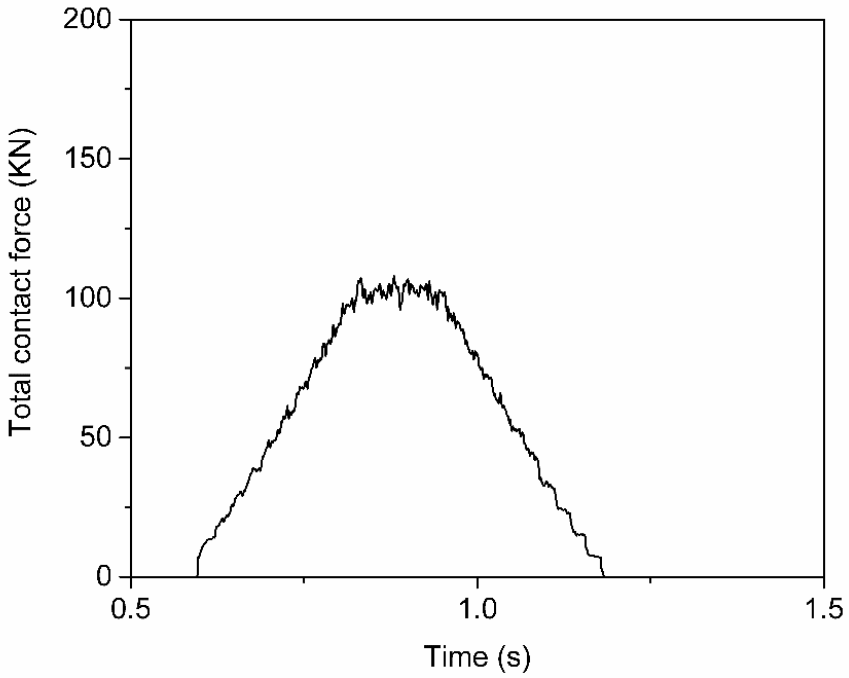

(b) Total contact force on planet and sun gear tooth for 11-slice model

Fig. 3.25. Contact force on planet and sun gear tooth for 11-slice model

To validate the drivetrain model developed in this study against test data, the planet gear bearing loads calculated in the multibody drivetrain dynamic simulation are compared with test data of NREL dynamometer test [83]. The sinusoidal torque as shown in Fig. 3.26 (a) is applied to the carrier of the drivetrain simulation model to describe the input torque data of NREL dynamometer test. There are two bearings mounted on each side of the planet gear shaft. The one on the front side is called upwind bearing, while that on the rear side is called downwind bearing. The bearing stiffness listed in Table 3.10 are used for the spring/damper force element. The gravitational force is applied to the geometrical center of each drivetrain component. The upwind bearing forces are compared with NREL test results in Figs. 3.26(b) and (c), showing good agreement in magnitude and frequency with the NREL test results. Furthermore, it is also observed that the simulation results are close to the NREL M1A simulation model results [83], which is a rigid multibody drivetrain model developed using SIMPACK.

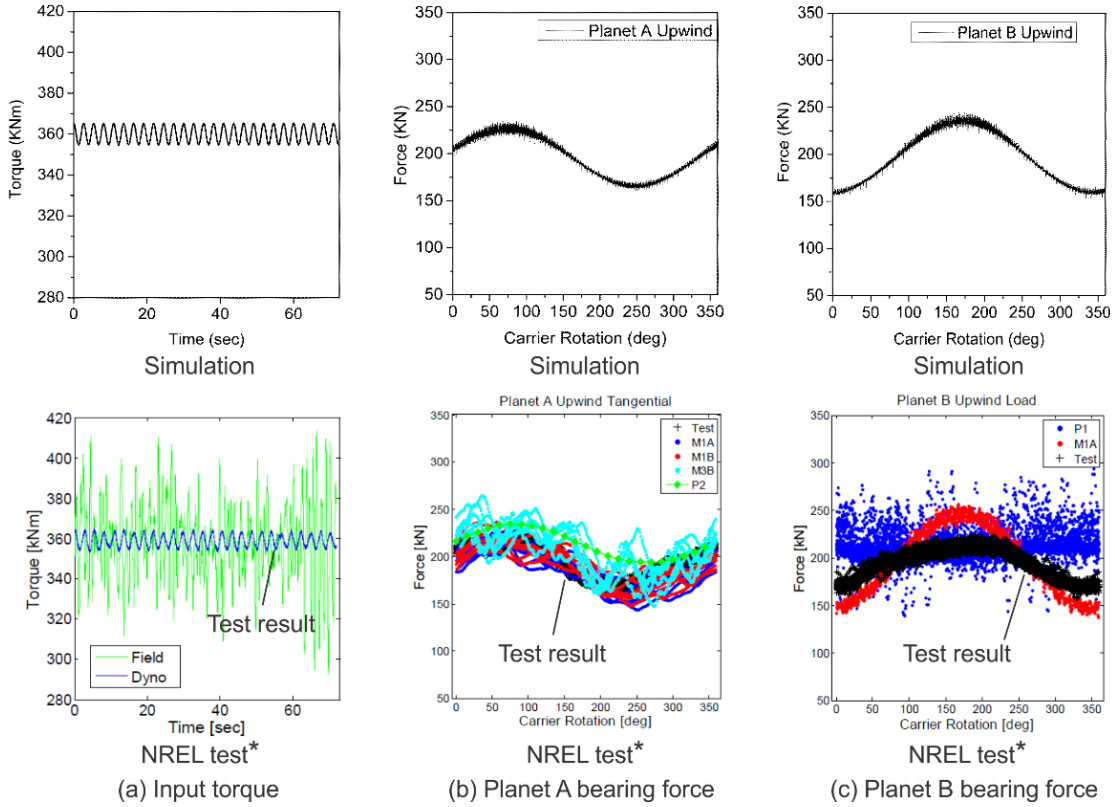

Fig. 3.26. Planetary gear bearing load comparison between simulation results and NREL test results [83]

It is important to notice there that the non-torque loads caused by the wind turbine rotor overhang weight and aerodynamic forces are not considered in the bench test. In the original GRC wind turbine design, as shown in Fig. 3.21 (b), the widely used three point suspension (one main bearing on the rotor shaft and two mounts for the gearbox trunnion) can transfer significant bending loads of the main shaft to the drivetrain, which is approximately 60% of wind turbine rated torque. This main shaft deflection can cause the carrier angular misalignment in the planetary stage of the drivetrain. Despite the micron level deflection of the main shaft, the contact stress distribution, the planetary gear load sharing factor and the gear teeth mesh phasing can be altered. The resulting unequal loads have an adverse impact on the drivetrain contact fatigue life. The non-torque loads are the combination of rotor weight and complex aerodynamic loads which have uncertainty. Thus, the non-torque loads raise a reliability issue for the three-point suspension drivetrains.

To address this issue, Alstom designed a new hub support configuration. In this design, the non-torque loads are transferred directly to the tower rather than through gearbox as in original design. It's called Alstom's Pure Torque drivetrain. A significate reduction of carrier misalignment as well as main shaft bending load is demonstrated using the newly designed drivetrain [10].

CHAPTER 4
WIND TURBINE GEAR TRAIN DESIGN OPTIMIZATION

4.1 Introduction

In this chapter, the multibody gear dynamics simulation procedure presented in the previous chapters is integrated into design optimization procedure for the wind turbine drivetrain design optimization considering wind load uncertainty. To this end, the wind load uncertainty model using the joint probability density function of the ten-minute mean wind speed and turbulence intensity, rotor blade aerodynamics, drivetrain dynamics considering the detailed gear tooth contact geometry including the profile modification, and probabilistic contact fatigue failure model is integrated for use in the gear tooth design optimization of wind turbine drivetrains to ensure the expected design life.

4.2 Wind Load Uncertainty Model

For evaluation of fatigue life of wind turbine systems, 10-minute wind data is widely used to characterize the short-term wind load variability at a specific location [84]. In this study, the joint probability density function (PDF) of 10-minute mean wind speed (V_{10}) and 10-minute turbulence intensity (I_{10}) is introduced to characterize the wind load uncertainty [85]. The turbulence intensity accounts for the severity of the wind speed fluctuation and is defined by

$$I_{10} = \frac{\Sigma_{10}}{V_{10}} \tag{4.1}$$

where Σ_{10} is the standard deviation of the wind speed for the 10-minute wind data.

Because of the preceding mathematical relation, the joint PDF of V_{10} and I_{10} is derived through the 10-minute joint PDF of V_{10} and Σ_{10} using the copula density function $c_{V\Sigma}$ for wind data measured for one year as [85]

$$f_{VI}(v_{10}, i_{10}) = c_{V\Sigma}(v_{10}, \sigma_{10}) \cdot f_{V10}(v_{10}) \cdot f_{\Sigma 10}(\sigma_{10}) \cdot v_{10} \tag{4.2}$$

where v_{10}, i_{10} and $\sigma_{10} = v_{10} \cdot i_{10}$ are realizations of random variables V_{10}, I_{10} and Σ_{10}, respectively. In the preceding equation, f_{V10} and $f_{\Sigma 10}$ are, respectively, PDFs for V_{10} and Σ_{10}, and they are identified by the measured wind data using Weibull and Gamma distributions as

$$f_{V10}(v_{10};C,k)=\frac{k}{C}\left(\frac{v_{10}}{C}\right)^{k-1}\exp\left[-\left(\frac{v_{10}}{C}\right)^{k}\right] \tag{4.3}$$

and

$$f_{\Sigma 10}(\sigma_{10};a,b)=\frac{1}{b^{a}\Gamma(a)}\sigma_{10}^{a-1}\exp\left(-\frac{\sigma_{10}}{b}\right) \tag{4.4}$$

where C and k are the scale and shape parameters for the Weibull distribution for V_{10}, respectively. In the gamma distribution for Σ_{10}, a and b are the shape and scale parameters, respectively, and $\Gamma(a)$ is a Gamma function of the parameter a. The Gumbel copula density function is chosen as

$$c_{V\Sigma}(u,v;\theta)=\frac{(-\ln u)^{\theta-1}(-\ln v)^{\theta-1}(\theta+w^{1/\theta}-1)w^{1/\theta-2}\exp(-w^{1/\theta})}{uv} \tag{4.5}$$

where u and v are marginal cumulative distribution functions (CDFs) of V_{10} and Σ_{10}, respectively. w is given by $w=(-\ln u)^{\theta}+(-\ln v)^{\theta}$, where θ is defined by the copula parameter τ as $\theta=1/(1-\tau)$. To define the joint PDF of V_{10} and I_{10}, the following five parameters need to be identified:

$$\mathbf{y}=[C \quad k \quad a \quad b \quad \tau]^{T} \tag{4.6}$$

It is important to notice here that one joint PDF characterizes the wind uncertainty measured at one location during one year only. However, the wind load distribution varies at different locations (i.e., wind farms) in different years and such a spatiotemporal variability needs to be considered in the wind uncertainty model [86]. To this end, using 249 groups of wind data collected from different sites in different years, 249 sets of C, k, a, b, τ parameters are identified and each set of parameters represents the annual wind load variation at specific location in specific year. Using the maximum likelihood estimate method, the distribution types for C, k, a, b, τ parameters are identified as the log-logistic, normal, generalized extreme value, Weibull, and extreme value distributions, respectively [86]. It is important to notice here that wind speeds are measured at a different height above the ground for each set of data, thus the measured wind speeds need to be converted to those at the hub height of the wind turbine under consideration using the normal wind profile model [87]. This wind uncertainty model allows for considering wide range of

probabilistic wind loads for evaluation of the contact fatigue life of wind turbine drivetrains.

For gear design optimization, the averaged wind load probability model is developed using Monte Carlo simulation of the joint PDFs for V_{10} and I_{10} considering the spatiotemporal wind load variability. To this end, one million joint PDFs defined by one millions sets of $\mathbf{y}^l = [C^l \quad k^l \quad a^l \quad b^l \quad \tau^l]^T$ ($l = 1, \cdots, N_{VI}$) are defined as

$$f_{VI}^{ijl}(v_{10}^i, i_{10}^j; \mathbf{y}^l) = c_{V\Sigma}(v_{10}^i, \sigma_{10}^{ij}; \tau^l) \cdot f_{V10}(v_{10}^i; C^l, k^l) \cdot f_{\Sigma 10}(\sigma_{10}^{ij}; a^l, b^l) \cdot v_{10}^i \tag{4.7}$$

where $N_{VI} = 1 \times 10^6$ and the PDF is evaluated for v_{10}^i and i_{10}^j. Using the resulting one million joint PDFs, the mean of the PDF evaluated for each v_{10}^i and i_{10}^j are calculated to develop the averaged wind load PDF model used for the design optimization as

$$\overline{f}_{VI}^{ij}(v_{10}^i, i_{10}^j) = \frac{\sum_{l=1}^{N_{VI}} f_{VI}^{ijl}(v_{10}^i, i_{10}^j; \mathbf{y}^l)}{N_{VI}} \tag{4.8}$$

where the lower bound of the mean wind speed is selected as the cut-in wind speed, while the upper bound is the cut-out wind speed for the wind turbine under consideration.

In this study, the speed range is defined from 5 m/s to 25 m/s with an increment of 2 m/s (i.e., $i = 1, \cdots, 12$), while the turbulence intensity range is assumed from 0.02 (2 %) to 1 (100 %) with 0.02 (2 %) increment (i.e., $j = 1, \cdots, 50$). The averaged joint PDF obtained for the measured wind data is presented in Fig. 4.1 at the hub height of 55 m and PDFs for *C*, *k*, *a*, *b* and τ at this height used to obtain the joint PDF are summarized in Appendix. The volume of each bar gives an averaged probability for one scenario defined for V_{10} and I_{10} considering the wind load variation in a wide spatiotemporal range. It is observed from this figure that the probability for wind condition in the range of V_{10} < 13 m/s and I_{10} < 0.3 is relatively high, while the probability of the extreme wind condition given in the range of 20 < V_{10} < 25 m/s and 0.5 < I_{10} < 1 is low. The highest probability density of 0.576 occurs at V_{10} = 7 m/s and I_{10} = 0.1.

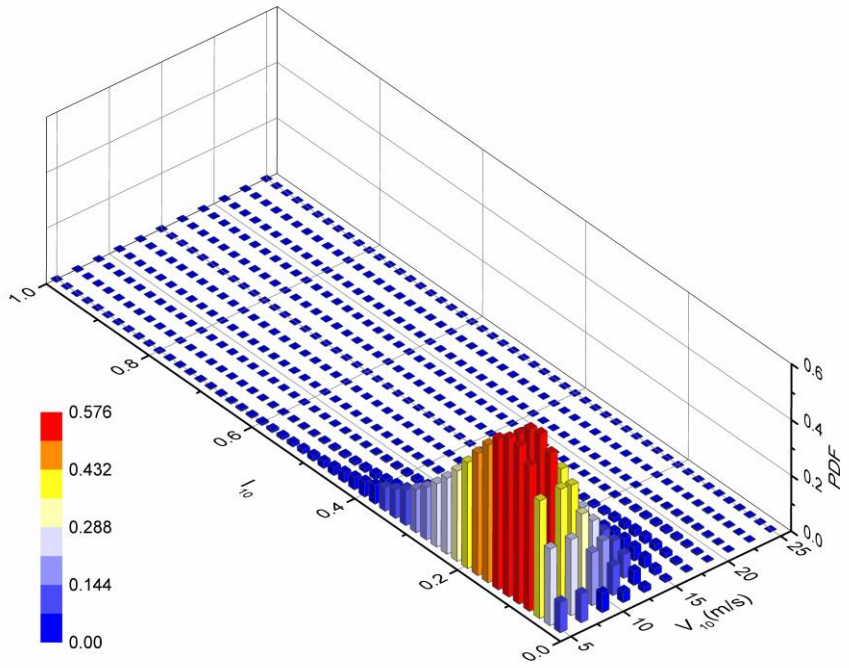

Fig. 4.1 Averaged joint probability density function for V_{10} and I_{10}

4.3 Contact Fatigue Prediction Using Multibody Gear Dynamics Simulation

4.3.1 Pitting Contact Fatigue Model

Using the wide spatiotemporal wind uncertainty model introduced in the previous section, a numerical procedure for predicting the pitting fatigue life is discussed in this section. The pitting fatigue is a typical failure mode exhibited in properly lubricated gears and is classified as the subsurface-initiated failure [11]. That is, the total fatigue life is defined by the sum of the number of load cycles required to initiate the subsurface crack N_i and that required for the crack to propagate to the surface N_p as [11,18]

$$N = N_i + N_p \tag{4.9}$$

Using the Dang Van's assumption that the fatigue micro-crack appears when the mono-crystal reaches the elastic shakedown due to shearing, the number of cycles for crack initiation is defined by [18]:

$$N_i = \frac{1}{2}\left(\frac{\tau_{\max} + 3\left(\tau_f' / \sigma_f' - 0.5\right) p_H}{\tau_f'} \right)^{1/c} \tag{4.10}$$

where $\tau_{\max}$ and p_H are, respectively, the maximum shear stress and hydrostatic stress in the subsurface; σ_f' and τ_f' are fatigue strength coefficients for tension/compression and shearing, respectively; and c is a fatigue strength exponent. It is assumed that the crack is initiated at a point where the ratio of the maximum shear contact stress to the hardness is maximal and the initial crack is parallel to the surface [11].

Assuming the Hertzian contact between two cylinders has the radius of curvature of R_1 and R_2, the maximum contact pressure is obtained by $p_{\max} = 2\bar{F} / \pi b_0$ as shown in Fig. 4.2(a) [87], where $\bar{F}$ is the contact force per unit length along the cylinder axis and b_0 is the half width of the contact patch defined by $b_0 = 2\sqrt{\bar{F}\bar{R} / \pi \bar{E}}$. Note that $\bar{E}$ is an equivalent Young's modulus of two materials in contact defined by $1/\bar{E} = (1-\nu_1^2)/E_1 + (1-\nu_2^2)/E_2$; and $\bar{R}$ is an equivalent radius evaluated by the principal radii of curvature at the contact point on surfaces in contact and is defined by $1/\bar{R} = 1/R_1 + 1/R_2$. The greatest value of the maximum shear stress occurs at $z_0 = 0.786 b_0$ measured from the contact surface with a value of $\tau_{\max} = 0.3 p_{\max}$ [87] and it is assumed that the subsurface crack parallel to the surface is initiated at this point when the number of load cycles reaches N_i as illustrated in Fig. 4.2(a).

After the subsurface crack is initiated, the crack propagates under cyclical contact loads to the surface. Using the Paris equation, the crack propagation is modeled by [18]

$$\frac{da_p}{dN} = C_p \left((\Delta K)^m - (\Delta K_0)^m \right) \tag{4.11}$$

where a_p is the half length of the crack; N is the number of load cycles; C_p and m are constants; and ΔK is the model II stress intensity factor range. ΔK_0 is the threshold for the crack growth given by the empirical formula $\Delta K_0 = 2.45 + 3.41 \times 10^{-3} HV$ for the Vickers hardness HV [88]. That is, the crack grows only if ΔK is greater than ΔK_0. The stress intensity factor ΔK is defined by [11,18]

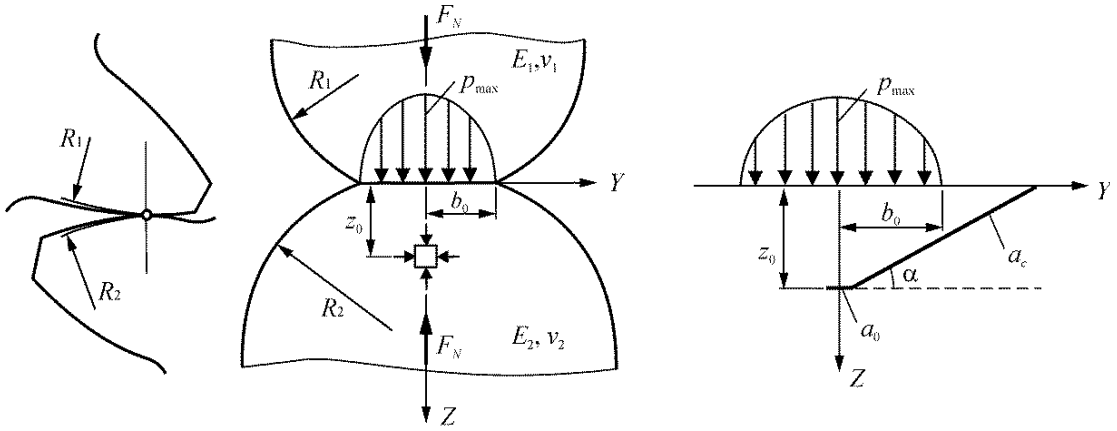

(a) Contact stresses (b) Subsurface-initiated crack

Fig. 4.2 Contact stresses and crack and subsurface-initiated crack

$$\Delta K = s\sqrt{\pi a_p}\,U(a_p) \tag{4.12}$$

where $U(a_p)$ is a factor considering the crack closure given by the empirical formula of Newman $U(a_p) = 0.89(1 + 0.11\exp(-0.1a_p))$ [89], while s is the crack growth driving force. It is shown in the literature [20] that growth of the subsurface crack under rolling contact loads is driven by the value defined by a ratio of the maximum shear stress to the hardness and the following expression for s is suggested by considering the effect of porosity and notch effects [18,20]:

$$s = \left(\frac{\tau_{\max}\delta_K}{\psi}\right)^2 \frac{1}{HV} \tag{4.13}$$

where $\delta_K = (K_t - 1)\eta + 1$ and $\psi = e^{-4.3\varepsilon}$ for empirically identified parameters K_t, η and ε [90]. Using Eq. 4.11, the number of cycles that causes the initial crack, parallel to the surface, to reach the surface is calculated as

$$N_p = \int_{a_0}^{a_c} \frac{1}{C_p\left((\Delta K)^m - (\Delta K_0)^m\right)} da_p \tag{4.14}$$

where a_0 is the half length of the initial crack assumed by [18]

$$a_0 = \frac{1}{8\pi}\left(\frac{\Delta K_0}{0.475 S_u}\right)^2 \tag{4.15}$$

and S_u is the ultimate tensile strength. a_c in Eq. 4.14 is a half of the critical crack length and is defined by $a_c = z_0 / \sin\alpha$ as shown in Fig. 4.2(b), where α defines the direction that the subsurface crack grows and z_0 is the depth from the surface at which the crack is initiated, i.e., a point where the maximum shear stress occurs. Accordingly, the total number of load cycles to pitting failure can be predicted by a sum of Eqs. 4.10 and 4.14 as a function of the maximum shear stress under a cyclic rolling contact load.

4.3.2 Use of Gear Dynamics Simulation for Prediction of Maximum Contact Pressure

As shown in the previous subsection, the crack growth is driven by the maximum shear contact stress $\tau_{\max}$ due to the contact load and, therefore, an accurate prediction of the maximum contact pressure $p_{\max}$ during gear meshing is of crucial importance in predicting the pitting fatigue life. Furthermore, to account for the wind load uncertainty characterized by the averaged joint PDF of the 10-minute mean wind speed (V_{10}) and turbulence intensity (I_{10}) introduced in Section 4.2, multiple 10-minute drivetrain dynamics simulations need to be performed for various choices of v_{10} and i_{10}, thus the multibody drivetrain dynamics simulation becomes a computational burden in the entire design optimization process. In addition, since the tooth contact pressure is sensitive to the gear tooth profile, an accurate description of the tooth profile geometry and precise contact geometry calculation are required and use of a simplified gear contact dynamics model is not suited. For example, profile modification called tip relief is widely used to lower the transmission error that is a cause of gear noise and vibration [40,76] and a slight modification of the tooth profile geometry on the order of microns alters the contact pressure on the profile surface, thereby influencing the pitting fatigue damage (i.e., crack growth). For this reason, the amount of tip relief is one of the important design parameters, together with the tooth face width [49] and the effect of micro geometry needs to be precisely evaluated using the gear dynamics simulation.

For this reason, a numerical procedure for the multibody gear dynamics simulation based on the tabular contact search algorithm presented in Chapter 2 is introduced and integrated into the gear design optimization procedure considering the wind load

uncertainty in this study. This procedure allows for the detection of the gear tooth contact in an efficient manner by introducing the look-up contact tables while retaining the precise contact geometry and mesh stiffness variation in the evaluation of mesh forces, thereby leading to a computationally efficient gear dynamics simulation suited for the design optimization procedure considering wind load uncertainty.

4.4 Numerical Procedure for Wind Turbine Drivetrain Design Optimization

4.4.1 Formulation of Optimization Problem

For gear design optimization to ensure the expected service life under the wind load uncertainty, an integrated numerical procedure is developed using the wind uncertainty model, the pitting fatigue prediction model, and multibody gear dynamics simulation procedure discussed in previous sections [91]. For given design variables **d**, including gear tooth geometry parameters such as face width and tip relief, the random time-domain wind speed data is generated for given 10-minute mean wind speed v_{10} and turbulence intensity i_{10} characterized by the averaged joint PDF using NREL TurbSim [92].TurbSim is used to generate the three-dimensional time-domain wind field using a prescribed power spectral density function (PSD) and a coherence function using Veer's method [92]. The PSD function is given as a function of both v_{10} and i_{10}, while the coherence function is given as a function of v_{10} only. The Veer's method is based on a general random process to a generate time series of wind speed at discrete points. The wind speed data is then inputted into NREL FAST [93] to perform the time-domain coupled nonlinear aero-hydro-servo-elastic simulation of a wind turbine considering the pitch control of the rotor blade. The input data of FAST that includes the wind turbine structure and aerodynamic properties are summarized in Appendix B. The wind turbine blade pitch control is considered using the subroutine "PitchCntrl" in FAST with the control region 3 (speed control). The pitch control parameters used in this design optimization problem are summarized in Table 4.1. The transmitted torque and speed of the rotor hub are predicted and used as input to the high-fidelity multibody gear dynamic simulation for calculating the 10-minute mesh force variation.

Since the probability of v_{10} and i_{10} is defined by the averaged joint probability density function $\bar{f}_{VI}(v_{10}, i_{10})$, the 10-minute fatigue damage can be defined as follows:

$$D_{10\min}(\mathbf{d}) = \int_{I_L}^{I_U}\int_{V_L}^{V_U} \overline{f}_{VI}(v_{10}, i_{10}) D_{10\min}(\mathbf{d}, v_{10}, i_{10}) dv_{10} di_{10} \tag{4.16}$$

where $D_{10\min}(\mathbf{d}, v_{10}, i_{10})$ is the 10-minute fatigue damage evaluated for v_{10} and i_{10}; V_L and V_U indicate the lower and upper bounds of the mean wind speed under consideration, and I_L and I_U are those of the turbulence intensity. By numerically integrating Eq. 4.16 using Riemann integral, one-year fatigue damage can be obtained as

$$D_{1\text{year}} = 6 \times 3000 \sum_{i=1}^{n_v}\sum_{j=1}^{n_i} \overline{f}_{VI}^{ij}(v_{10}^i, i_{10}^j) D_{10\min}^{ij}(\mathbf{d}, v_{10}^i, i_{10}^j) \Delta v_{10} \Delta i_{10} \tag{4.17}$$

where $D_{10\min}^{ij}(\mathbf{d}, v_{10}^i, i_{10}^j)$ is evaluated for $i = 1, \cdots, n_v$ and $j = 1, \cdots, n_i$. It is assumed that a wind turbine is operated for 3000 hours per year [94]. It is important to notice here that the gear teeth do not experience cyclical loading during the maintenance period and when the wind speed is lower than the cut-in wind speed or higher than the cut-out speed. To evaluate the one-year fatigue damage for given design variable **d**, the 10-minute damage $D_{10\min}^{ij}(\mathbf{d}, v_{10}^i, i_{10}^j)$ needs to be calculated at $n_v \times n_i$ sampling points for v_{10}^i ($i = 1, \cdots, n_v$) and i_{10}^j ($j = 1, \cdots, n_i$) using the 10-minute gear-train dynamics simulation. It is important to notice here that the input rotational speed varies as a function of time, thus the maximum contact pressure used for the pitting fatigue life calculation varies at each load cycle.

Table 4.1 Control parameters for blade pitch control

Name	Value
Gain on TF 1	-1.0
Rotor speed set point	20.463 rpm
Integrator anti-windup gain	0.3
Minimum pitch angle	2.6 deg
Maximum pitch angle	90.0 deg
Time interval for pitch control	0.025 s
Pitch angle at start of gain scheduling	0.0454 rad
Pitch angle at end of gain scheduling	0.5 rad
Power law gain sched. coefficient	0.213
Power law gain sched. exponent	-0.500

To account for the contact load variation, the pitting fatigue damage is evaluated by Miner's rule as [95]

$$D_{10\min}^{ij}(\mathbf{d}, v_{10}^{i}, i_{10}^{j}) = \sum_{k=1}^{n_{10}^{ij}} \frac{1}{N^{ijk}(p_{\max}^{ijk})} \tag{4.18}$$

where N^{ijk} is the number of load cycles to failure for each meshing cycle k and n_{10}^{ij} is the number of load cycles of the gear tooth under consideration in the 10-minute simulation. That is, N^{ijk} is defined using the maximum contact pressure $p_{\max}^{ijk}$ at load cycle k for the wind scenario defined by v_{10}^{i} and i_{10}^{j}. As an alternative to Miner's rule, one can determine the 10-minute damage as

$$D_{10\min}^{ij}(\mathbf{d}, v_{10}^{i}, i_{10}^{j}) = \frac{n_{10}^{ij}}{N^{ij}(\bar{p}_{\max}^{ij})} \tag{4.19}$$

where $\bar{p}_{\max}^{ij}$ is the equivalent maximum contact pressure for the 10-minute wind load scenario as [21]

$$\bar{p}_{\max}^{ij} = \left(\int_0^{\infty} (p_{\max}^{ij})^n f_{p_{\max}}^{ij}(p_{\max}^{ij}) dp_{\max}^{ij} \right)^{1/n} \tag{4.20}$$

where $f_{p_{\max}}^{ij}(p_{\max}^{ij})$ is a probability density function of the maximum contact pressure for the 10-minute simulation for v_{10}^{i} and i_{10}^{j}. The exponent n is selected to be the exponent of the Paris equation given in Eq. 4.11, i.e., $n = m$ [21], while $n = 1$ leads to a mean value of the maximum contact pressures in the 10-minute simulation.

The expected service life of wind turbines is 20 years, thus the constraint for the optimization problem is defined by $G(\mathbf{d}) = 20D_{1\text{year}} - 1 < 0$ for $\mathbf{d}^L < \mathbf{d} < \mathbf{d}^U$, where $\mathbf{d}^L$ and $\mathbf{d}^U$ are lower and upper bounds of the design variable $\mathbf{d}$. Accordingly, the following optimization problem is posed:

$$\begin{aligned} &\text{Minimize } J(\mathbf{d}) \\ &\text{subject to } G(\mathbf{d}) = 20D_{1\text{year}} - 1 < 0 \\ &\text{for } \quad \mathbf{d}^L < \mathbf{d} < \mathbf{d}^U \end{aligned} \tag{4.21}$$

where the objective function $J(\mathbf{d})$ is defined by a total weight of the drivetrain, while gear tooth geometry parameters such as gear face width and tip relief are selected as the design variable **d**. The optimization problem is solved using a multidisciplinary reliability-based design optimization software RAMDO [96].

4.4.2 Summary of Numerical Procedure

In what follows, the entire numerical procedure is summarized as shown in Fig. 4.3.

Step 1: For given measured wind data at different locations (i.e., wind farms) in different years, the joint probability density functions for V_{10} and I_{10} are identified as $f_{VI}(v_{10}, i_{10}; \mathbf{y})$ and then PDFs of $\mathbf{y} = [C \quad k \quad a \quad b \quad \tau]^T$ are identified to account for the wide spatiotemporal wind load uncertainty. The averaged joint PDF $\bar{f}_{VI}^{ij}(v_{10}^i, i_{10}^j)$ is generated using the 10^6 samples for $n_v \times n_i$ points of v_{10}^i ($i = 1, \cdots, n_v$) and i_{10}^j ($j = 1, \cdots, n_i$).

Step 2: For $n_v \times n_i$ points of v_{10}^i and i_{10}^j in the range of the averaged joint PDF, the time-domain 10-minute random wind data $\mathbf{U}^{ij}(v_{10}^i, i_{10}^j) = [u^{ij}(t) \quad v^{ij}(t) \quad w^{ij}(t)]^T$ is generated using the wind field simulation software TurbSim.

Step 3: Using the 10-minute wind data obtained at Step 2, the time-domain coupled nonlinear aero-hydro-servo-elastic simulation of a wind turbine is performed using FAST software to predict rotor angular velocity variation for each wind scenario v_{10}^i and i_{10}^j. The elastic deformation of rotor blades and its interaction with aerodynamics are considered with a simplified pitch control algorithm.

Step 4: For all the pairs of gears in the drivetrain model under consideration for design variables **d**, the contact geometry analysis for a one-tooth model considering profile modification is performed using the combined non-conformal and nodal contact search method for various rotation angles and then the contact point as well as the tooth geometry at each contact point including the tangents, normal, and principal curvatures are stored in the look-up contact tables.

Step 5: Using the multiple look-up contact tables generated for design variable **d**, multibody gear train dynamics simulation is performed for the 10-minute input rotor angular velocity data obtained at Step 3 for each wind scenario v_{10}^{i} and i_{10}^{j} . The tabular contact search is performed to determine the contact point for all the pair of gears using multiple look-up contact tables and the contact forces are calculated using the variable mesh stiffness model that accounts for the effect of the contact stiffness, tooth bending stiffness, and gear body (foundation) stiffness. The mesh force time-history data for each tooth are stored as output for contact fatigue prediction. Notice that the 10-minute multibody drivetrain simulation is performed for all the $n_v \times n_i$ wind scenarios and the simulation for each scenario runs in parallel using parallel computing technique.

Step 6: Using the mesh force time-history data obtained at Step 5, the 10-minute damage $D_{10\min}^{ij}(\mathbf{d}, v_{10}^{i}, i_{10}^{j})$ is calculated and then the critical tooth with the largest damage is selected. The $D_{10\min}^{ij}$ is evaluated by either Miner's rule (Eq. 4.18) or the equivalent maximum contact pressure method (Eq. 4.19) for all the $n_v \times n_i$ wind scenarios and then the one-year fatigue damage $D_{1\text{year}}$ for the current design **d** is evaluated by Riemann integral as Eq. 4.17.

Step 7: Using the one-year fatigue damage evaluated, the constraint is defined such that contact fatigue life is longer than 20 years as given by Eq. 4.21 and the cost function is evaluated for the current design **d**.

Step 8: Step 4 through 7 are repeated by updating the design variables **d** until the cost function is minimized while meeting the fatigue failure constraint using the optimization solver.

4.5 Deterministic Design Optimization under Mean Wind Load

In this Section, the 750KW GRC wind turbine [97-99] as shown in Fig. 4.4 is used to demonstrate the integrated multibody gear dynamics simulation capability for design optimization of wind turbines considering wind load uncertainty [91]. As shown in Fig. 4.4, the gearbox consists of one planetary gear at the high-speed stage and two parallel axis

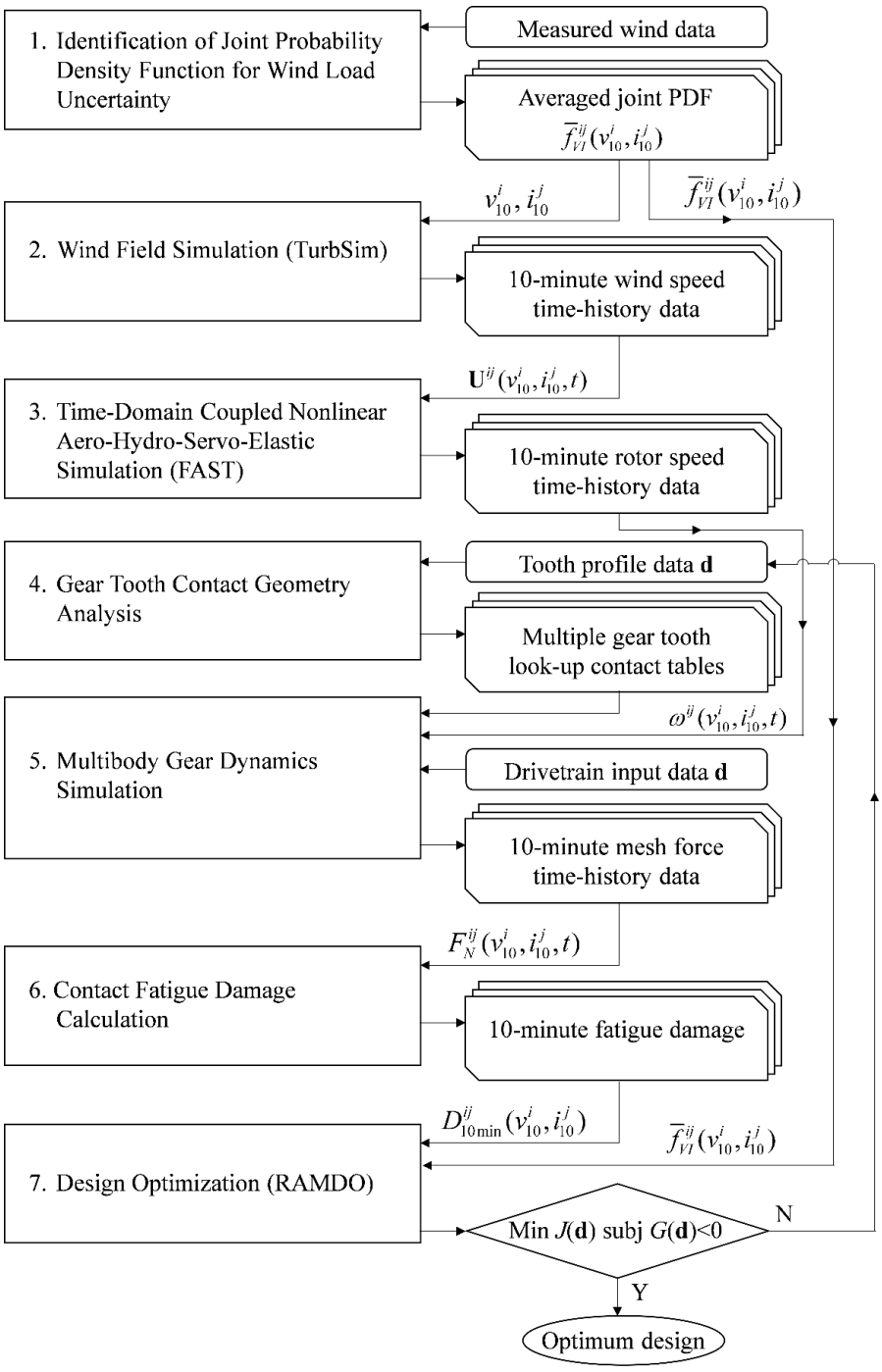

Fig. 4.3 Numerical procedure of integrated gear dynamics simulation

gears at the intermediate and high-speed stages as presented in Section 3.5. The overall gear ratio is 81.49 [80]. The basic gear geometric parameters are summarized in Table 3.6 and one can refer to the literature [80] for more details on the specification. Gear face widths in the planetary stage are all assumed to be the same. The gear material is assumed to be 18CrNiMo7-6 and material properties used in the pitting fatigue model are summarized in Appendix C. The sun gear has the smallest pitch diameter in the planetary stage and it is engaged with three planetary gears at the same time. Therefore, the sun gear is most critical in terms of the contact fatigue failure for this drivetrain [21].

To generate time-domain angular velocity data given to the input main shaft of the drivetrain model, random time-domain wind speed data is generated first using NREL TurbSim and then aero-hydro-servo-elastic simulation of the wind turbine is carried out using NREL FAST. To create the wind turbine model for FAST, rotor blade cross section geometry data and tower properties of the GRC wind turbine summarized in Appendix B are used.

4.5.1 Probabilistic Contact Fatigue Damage

Using the procedure summarized in Fig. 4.3, the 10-minute fatigue damage $D_{10\min}(\mathbf{d}, v_{10}, i_{10})$ at the recess point on the most critical tooth of the sun gear is calculated for each wind load scenario defined by V_{10} and I_{10} as shown in Fig. 4.5. Each length of the bar in this figure indicates the magnitude of 10-minute fatigue damage. It is observed from this figure that the fatigue damage increases with an increase of the mean wind speed since the number of load cycles and contact loads increase as the rotor speed increases. However, the fatigue damage plateaus when the wind speed gets higher than the rated speed of 16 m/s. This is attributed to the fact that the blade pitch control is activated at the rated speed (16 m/s) to maintain constant power generation at a constant rotor speed [99]. The highest value of 10-minute fatigue damage of 3.44E-5 occurs in the mean wind speed range of 17 m/s < V_{10} < 25 m/s.

In general, the fatigue damage increases as the turbulence intensity increases for the same mean wind speed. However, the opposite trend is observed when the blade pitch control is active. This is explained by change in rotor angular velocity of the wind turbine

shown in Fig. 4.6. In this figure, mean wind speed of 11m/s is assumed as an example and time histories of rotor angular velocity for different turbulence intensities from 0.06 to 1 are compared. As observed from this figure, the rotor velocity amplitude increases as the turbulence intensity increases. However, since the pitch control is activated when the wind speed exceed rated speed, maximum rotor speed is bounded, whereas minimum rotor speed is not bounded. For this reason, a larger turbulence intensity wind scenario has smaller minimum rotor speed value, resulting in smaller damage evaluated by the contact fatigue model. If pitch control is off, the maximum rotor speed is not bounded, larger turbulence intensity leads to larger damage value.

The integrand of Eq. 4.16 is calculated as a product of averaged joint PDF of random wind load $\bar{f}_{VI}^{ij}(v_{10}^i, i_{10}^j)$ and 10-minute fatigue damage distribution $D_{10\min}(\mathbf{d}, v_{10}, i_{10})$ as shown in Fig. 4.7. The volume of each bar gives a probabilistic 10-minute fatigue damage with certain design **d** for one wind load range defined for V_{10} and I_{10}. It is observed from this figure that probabilistic damage value for wind condition in the range of 10 m/s < V_{10} < 15 m/s and 0.05 < I_{10} < 0.2 is relatively high, while the probabilistic damage value of the extreme wind condition given in the range of 20 m/s < V_{10} < 25 m/s and 0.4 < I_{10} < 1 is low. Furthermore, the highest probability density of 3.69×10^{-6} occurs at V_{10} = 11 m/s and I_{10} = 0.1, which is different from those of averaged wind load (V_{10} = 7 m/s and I_{10} = 0.1) as shown in Fig. 4.1. It means that the V_{10} and I_{10} giving the highest probability density depends on not only the distribution of random wind load $\bar{f}_{VI}^{ij}(v_{10}^i, i_{10}^j)$, but also the 10-minute fatigue damage distribution $D_{10\min}(\mathbf{d}, v_{10}, i_{10})$.

Furthermore, to discuss the effect of the way to evaluate the cumulative contact fatigue damage, the one-year fatigue damage evaluated using three different fatigue damage evaluation approaches is presented in Table 4.2. The first approach is the Miner's rule as given by Eq. 4.18, while the second and third approaches assume the mean of the maximum contact pressure to evaluate the fatigue damage during 10 minutes as presented by Eq. 4.19 together with Eq. 4.20. In the second approach, the exponent *n* is same as that of the Paris equation, while *n*=1 is assumed in the third approach, leading to the mean of the maximum contact pressure during 10 minutes. It can be seen from this table that one-year fatigue damage values are very similar for this wind uncertainty model. In the

following design optimization study, the Miner's rule approach is used to evaluate the gear contact fatigue damage.

In order to illustrate the effect of wind load variation in a wide spatiotemporal range on one-year fatigue damage, the two sets of (C, k, a, b, τ) that characterize wind load distributions at different location and in different years are selected. They are C =6.00, k = 1.75, a = 2.00, b = 0.20, τ = 0.30, and C =10.00, k = 2.75, a = 4.00, b = 0.40, τ = 0.70, respectively. The corresponding joint PDFs of wind load variation for V_{10} and I_{10} are named as joint PDF 1 and joint PDF 2 and they are shown in Fig 4.8 and Fig. 4.9, respectively. They can represent two extreme cases of different annual wind load variation. It is observed from Fig. 4.8 that a high probability region lies in the low speed range (5 m/s < V_{10} < 10 m/s) and in the low turbulence intensity range (0.0 < I_{10} < 0.1). The highest probability density of 1.22 occurs at V_{10} = 5 m/s and I_{10} = 0.04, where both mean wind speed and turbulence intensity are small.

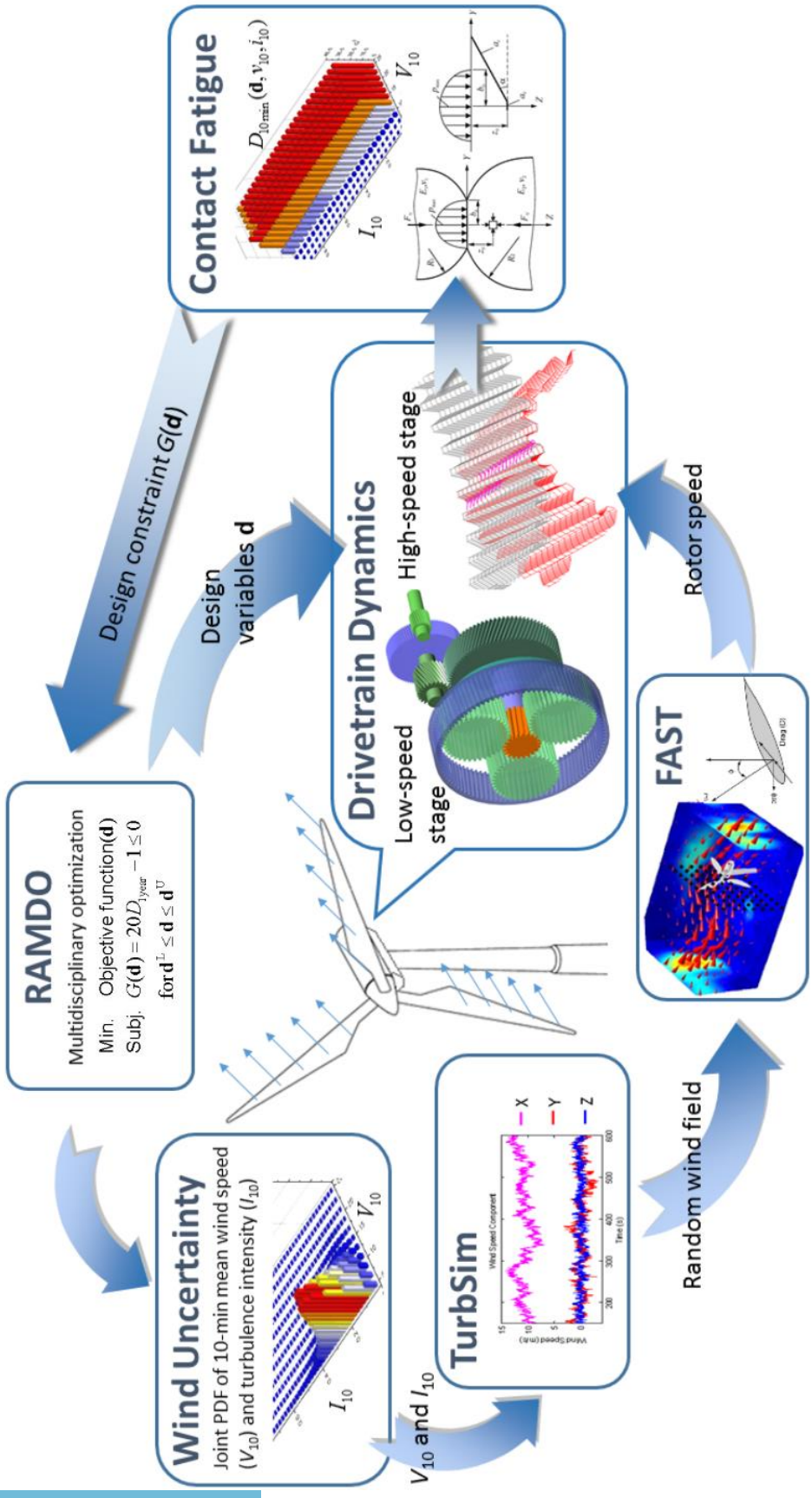

Fig. 4.4 Overview of integrated multibody gear dynamics simulation for wind turbine drivetrain design optimization considering wind load uncertainty

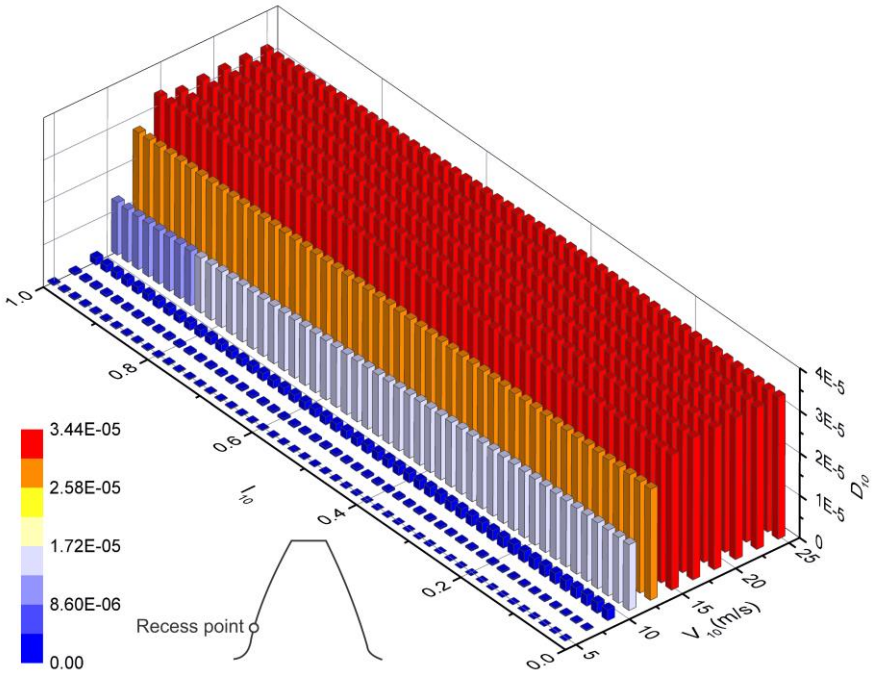

Fig.4.5 10-minute fatigue damage at recess point of sun gear

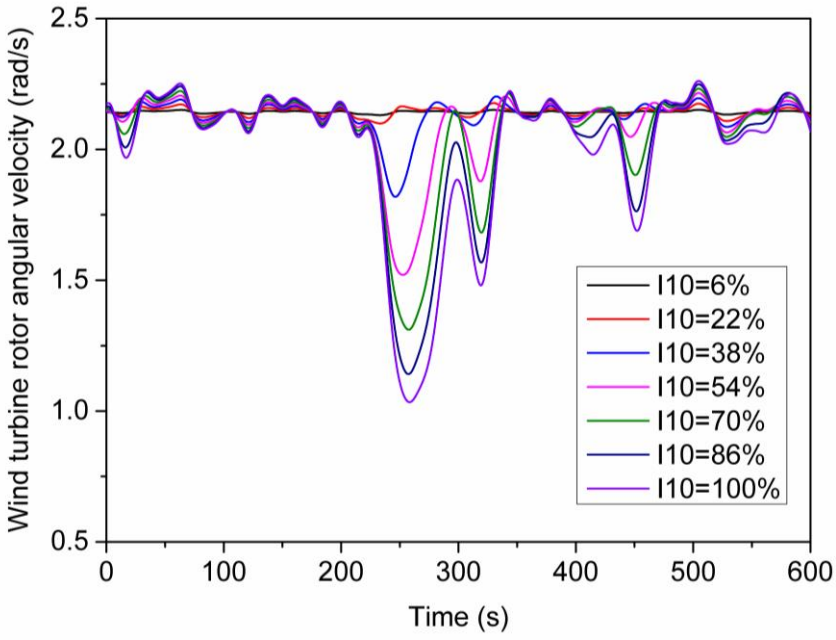

Fig.4.6. 10-minute rotor angular velocity under 11m/s mean wind speed and different turbulence intensity

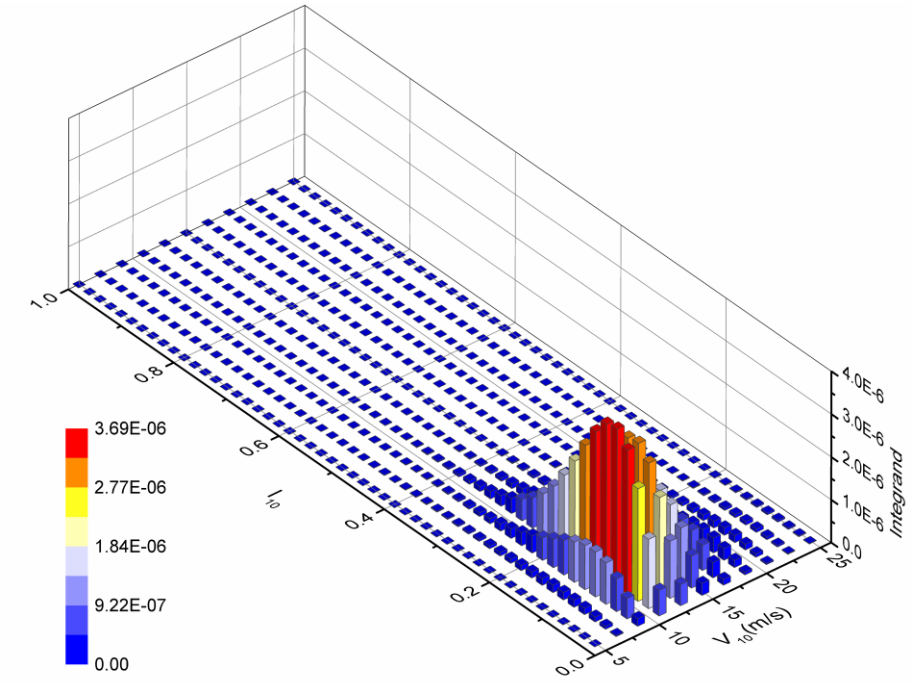

Fig.4.7 The product of averaged joint PDF of wind load and 10-minute fatigue damage distribution

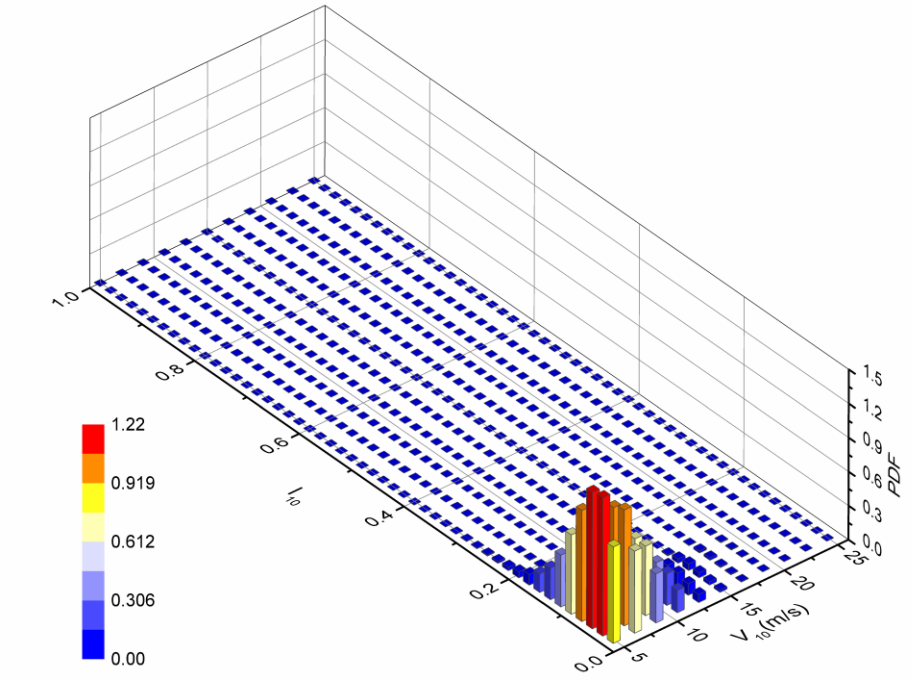

Fig. 4.8 Joint PDF-1 for V_{10} and I_{10}

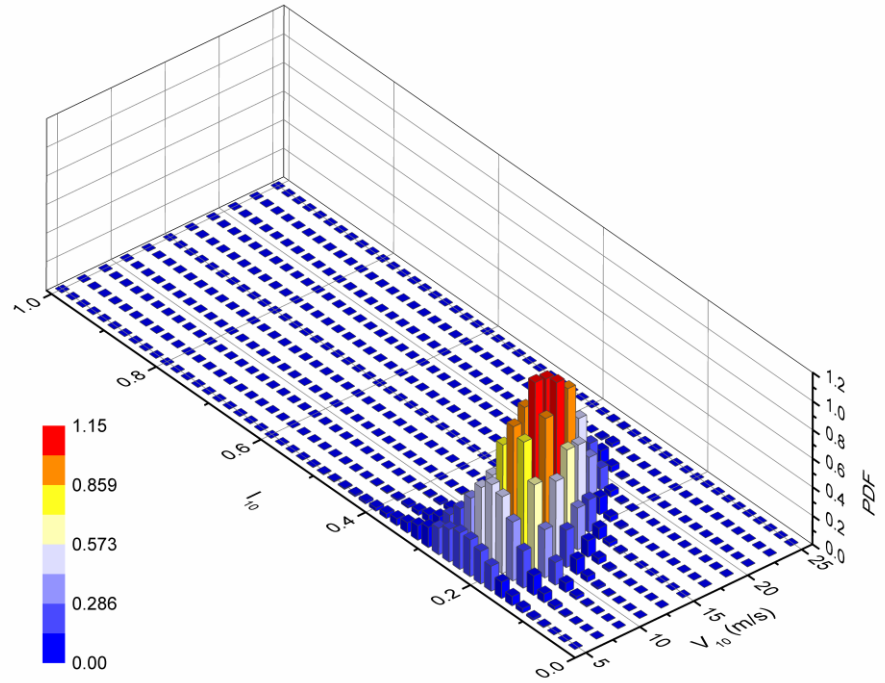

Fig. 4.9 Joint PDF-2 for V_{10} and I_{10}

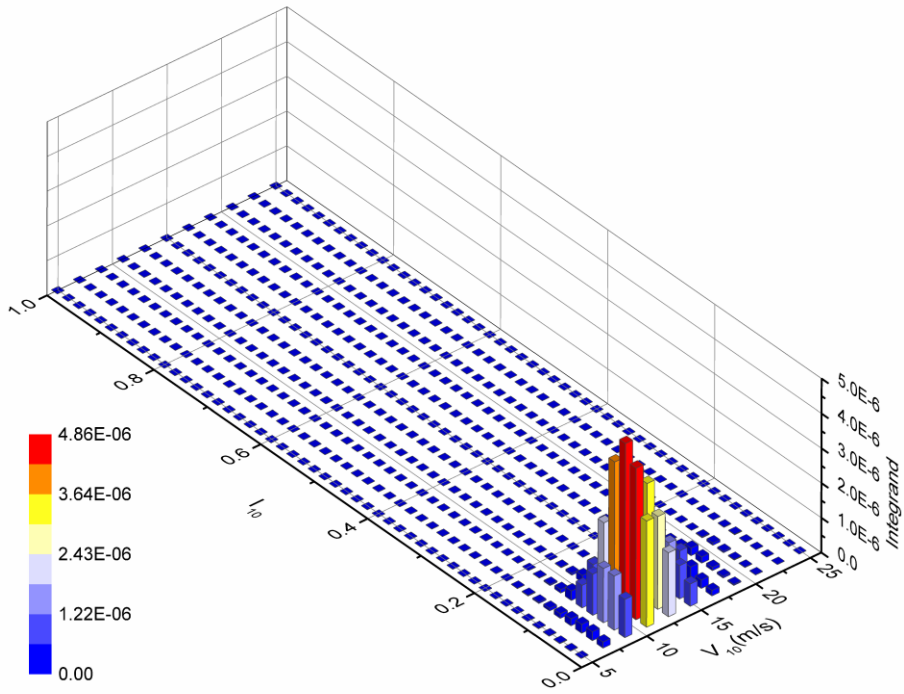

Fig.4.10 The product of joint PDF-1 of wind load and 10-minute fatigue damage distribution

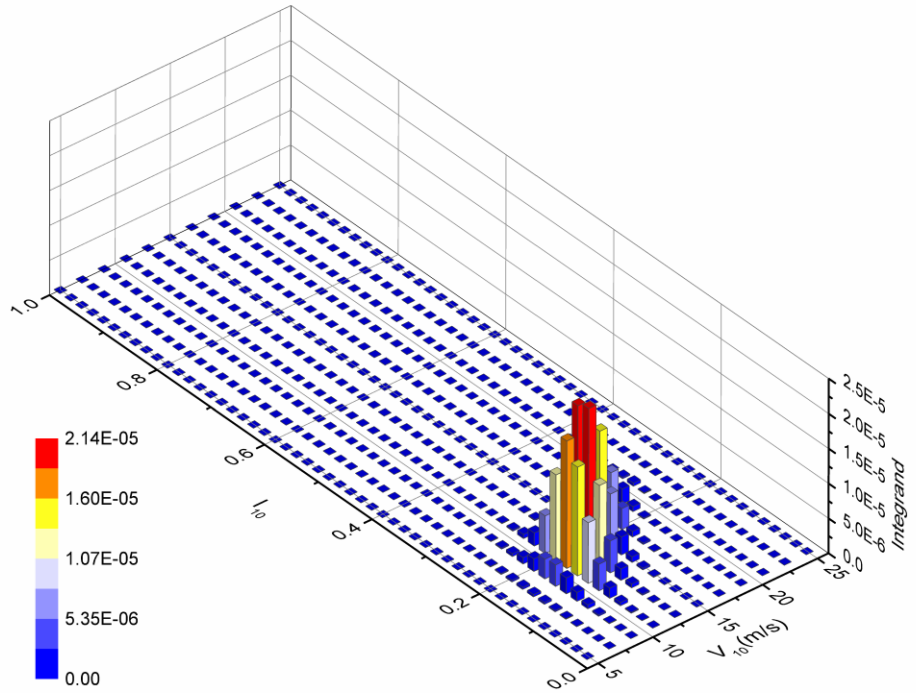

Fig.4.11 The product of joint PDF-2 of wind load and 10-minute fatigue damage distribution

Table 4.2 One-year contact fatigue damage from different evaluation approaches

Approach	One-year fatigue damage
Miner's rule	6.48×10^{-2}
Mean of the maximum contact pressure (n=1)	6.56×10^{-2}
Equivalent maximum contact pressure (n=3.05)	6.57×10^{-2}

Table 4.3 Different wind load PDFs effect on 1-year and 20-year fatigue damage

Wind load PDF	1-year fatigue damage	20-year fatigue damage
Joint PDF 1	3.65×10^{-2}	0.729
Joint PDF 2	1.59×10^{-1}	3.183
Averaged joint PDF	6.48×10^{-2}	1.296

On the other hand, for PDF 2 shown in Fig 4.9, the high probability region lies in the mild speed range (7 m/s < V_{10} < 17 m/s) and in the mild turbulence intensity range (0.1 < I_{10} < 0.3). The highest probability density of 1.21 occurs at V_{10} = 13 m/s and I_{10} = 0.2. The mean wind speed and turbulence intensity are higher than those of PDF 1. To discuss the effect on the contact fatigue damage distribution, the integrands of the product of the joint PDF 1 of random wind load $f_{VI}^{1,ij}(v_{10}^{i}, i_{10}^{j})$ and the corresponding 10-minute fatigue damage distribution $D_{10\min}(\mathbf{d}, v_{10}, i_{10})$ are shown in Fig. 4.10 and that of the joint PDF 2 is shown in Fig. 4.11. It is observed from these figures that the damage distribution and the magnitude differ significantly. The one-year and 20-year fatigue damage values for sun gear calculated using the joint PDF 1, joint PDF 2 and the averaged joint PDF wind load are compared in Table 4.3. It can be seen from this table that contact fatigue damages associated with PDF 1 (small wind load case) and PDF 2 (large wind load case) differ significantly. Furthermore, the averaged PDF obtained using MCS indicates that sun gear fails earlier than 20-year service life. As shown in this example, consideration of wide spatiotemporal wind load distributions (i.e., PDF of the joint PDF parameters (*C, k, a, b,* τ)) is crucial to realistic prediction of the gear tooth contact fatigue life for design optimization of wind turbine drivetrains.

4.5.2 Selection of Design Variables

To improve the pitting fatigue life under the wind load uncertainty, the face width and the amount of the tip relief are defined as design variables for the sun gear. In the initial (reference) design, the face width is 220 mm and no tip relief (i.e., involute profile) is used [80]. To demonstrate the effect of those two design variables on the pitting fatigue life, the maximum contact pressure evaluated at various points on the gear tooth for one mesh cycle is shown in Fig. 4.12 for four different face widths without tip relief. In this figure, the rated mean wind speed of 16m/s and turbulence intensity of 0.14 categorized in the medium range based on ISO standard [100] are assumed as a wind load. It is observed from this figure that the maximum pressure at the recess point P_3 is largest regardless the face width selected and it is clear that larger face width leads to smaller maximum contact pressure over the tooth surface, resulting in smaller damage as shown in Fig 4.13.

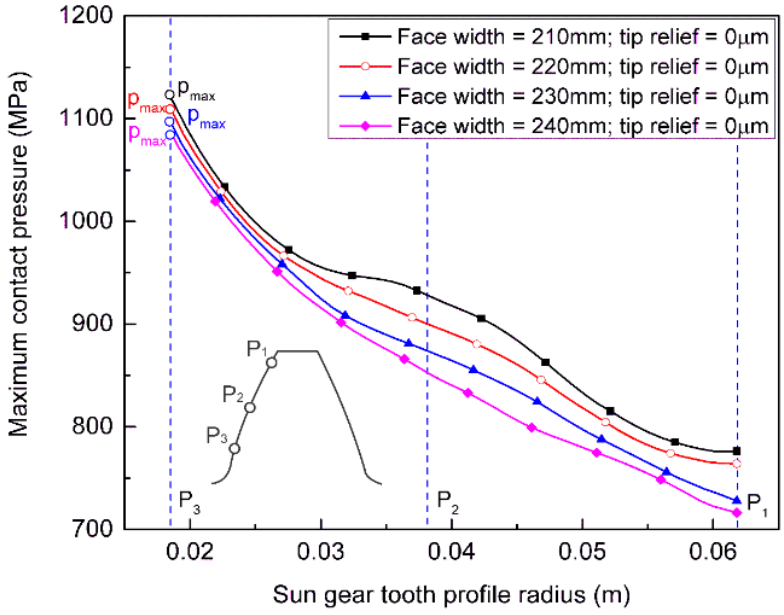

Figure 4.12 Effect of face width on maximum contact pressure

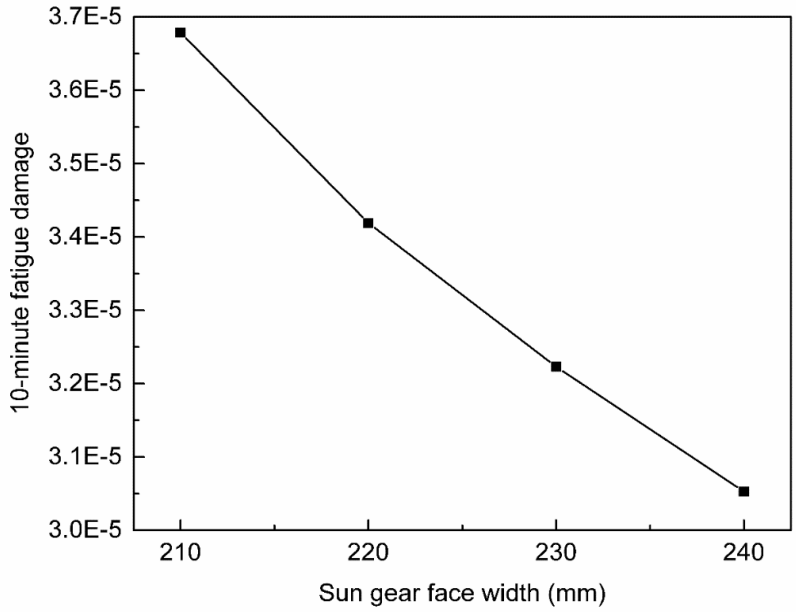

Figure 4.13 Effect of face width on 10-minute fatigue damage

However, increase in face width makes the total weight of the drivetrain larger and it also has an impact on the increase of cost. The other way of altering the contact pressure on the tooth surface is the profile modification. The linear tip relief defined by Eq. 3.1 is considered and the maximum contact pressure for different tip relief amount is shown in Fig. 4.14. In this figure, the face width of 220 mm is assumed and the tip relief start point is the pitch point. It is observed from this figure that the maximum contact pressure over the tooth surface changes in a different way as the tip relief increases and the greatest maximum contact pressure is shifted to the pitch point as the tip relief amount increases.

It is also observed from this figure that the greatest maximum contact pressure can be minimized at a tip relief amount of 55 μm. That is, there exists an optimum tip relief amount that can minimize the greatest maximum contact pressure over the tooth profile as shown in Fig. 4.15 summarizing the 10-minute fatigue damage for different tip relief amount. It is important to emphasize at this point that the optimum value depends on the wind condition defined by the mean wind speed and turbulence intensity. Furthermore, the material removed is in the order of microns, thus the tip relief has almost no effect on the total weight, but has major impact on the fatigue life defined as a constraint.

For this reason, in what follows, design optimization is discussed to find an optimum face width and tip relief that leads to minimization of the total weight of the gear-train under the wind load uncertainty while ensuring the 20-year fatigue life.

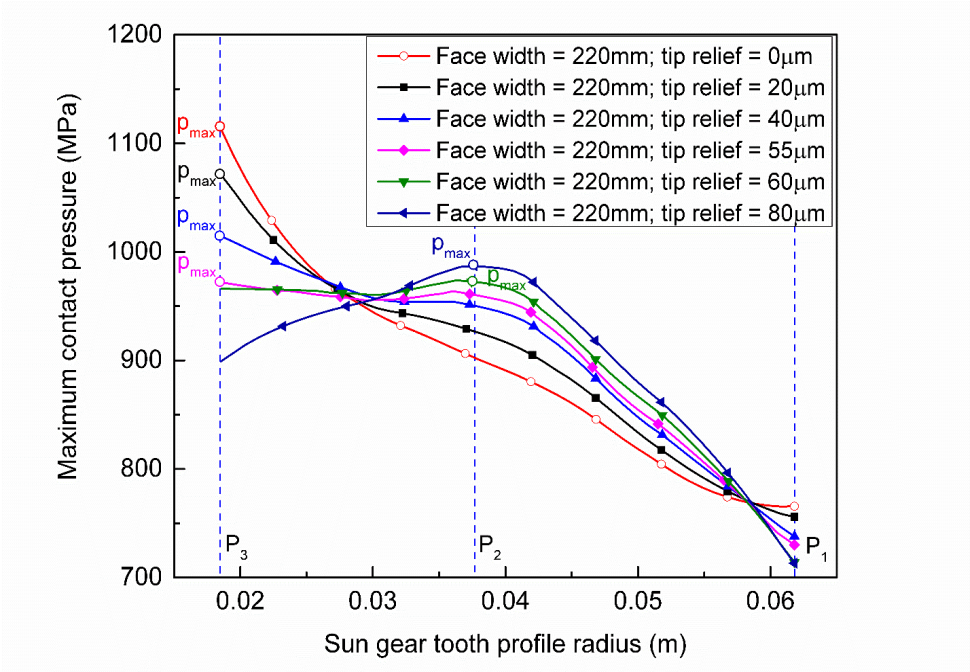

Figure 4.14 Effect of tip relief on maximum contact pressure

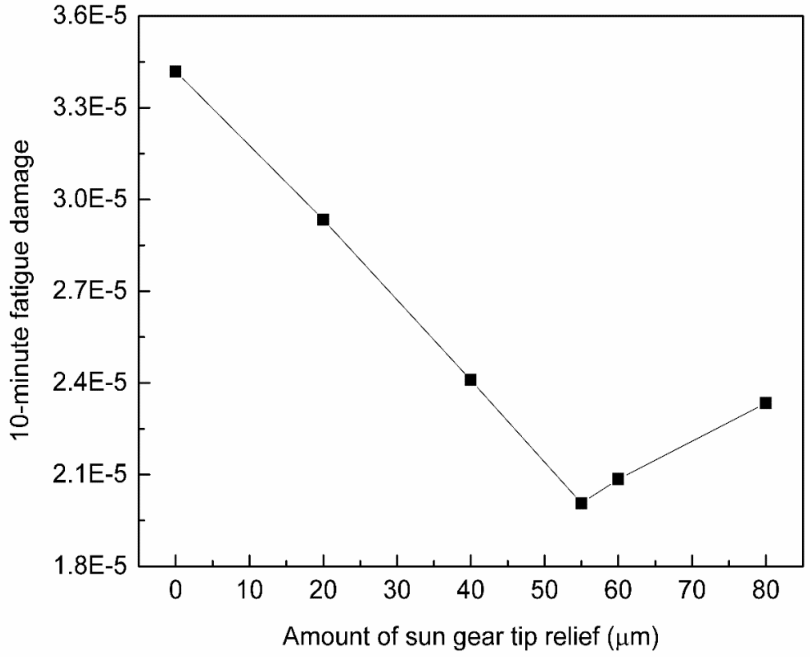

Figure 4.15 Effect of tip relief on 10-minute fatigue damage

4.5.3 DDO Results and Discussion

The following optimization problem is defined:

$$\begin{aligned} &\text{Minimize} \quad J(B) = (M^0_{\text{ring}} + M^0_{\text{sun}} + 3M^0_{\text{planet}})\frac{B}{B^0} \\ &\text{Subject to} \quad G(B,\delta_a) = 20D_{1\text{year}} - 1 \le 0 \\ &\qquad \text{for} \quad B^L \le B \le B^U \quad \text{and} \quad \delta_a^L \le \delta_a \le \delta_a^U \end{aligned} \tag{4.22}$$

where design variables include the face width B and the tip relief amount δ_a of the sun gear defined by $\mathbf{d} = [B \quad \delta_a]^T$; the cost function $J(B)$ is defined as the total mass of the planetary stage gears consisting of a ring gear, a sun gear and three planet gears. The superscript 0 in Eq. 4.22 indicates the value of the initial design $\mathbf{d}^0 = [B^0 \quad \delta_a^0]^T = [220\,\text{mm} \quad 0\,\mu\text{m}]^T$. M^0_{ring}, M^0_{sun} and M^0_{planet} are initial masses of the ring, sun and planet gears, respectively. The constraint is imposed to ensure that the pitting fatigue life is longer than 20 years (i.e., the 20-year fatigue damage is less than 1). The upper and lower bounds of the face width and tip relief amount are assumed as $167.5 \le B \le 272.5$ mm and $0 \le \delta_a \le 100$ μm. The sequential quadratic programming (SQP) method is used for this design optimization in RAMDO software [96]. The design sensitivity is calculated using forward finite difference method (FDM) with 1% perturbation.

By minimizing the cost function and satisfying the constraint, the optimum design is obtained. The results are summarized in Table 4.4. In this table, the optimum solution obtained without considering the tip relief as design variable is also included. As it can be seen from this table, face width of the sun gear is increased to 231 mm from 220 mm in the initial design to satisfy 20-year fatigue life when only face width is included in the design variable. This leads to 4.7 % increase in the normalized mass. On other hand, if the tip relief is introduced to the design variable vector **d**, the optimum face width becomes 202 mm with a tip relief amount of 41 μm. This optimum tip relief allows for minimization of the greatest maximum shear stress on the gear tooth surface without relying heavily on face width widening to meet the 20-year fatigue life constraint and it leads to mass reduction by 8.4%, leading to a more cost-effective design.

Table 4.4 Design optimization results

	Baseline design	Optimum design w/o tip relief	Optimum design w/ tip relief
Face width (mm)	220	231	202
Tip relief (μm)	0	0	41
Pitting fatigue life	15 years	20 years	20 years
Normalized mass	1.000	1.047	0.916

CHAPTER 5
RELIABILITY ANALYSIS OF WIND TURBINE DRIVETRAIN UNDER WIND LOAD UNCERTAINTY

5.1 Introduction

In this chapter, the reliability analysis is carried out for wind turbine drivetrain with gear contact fatigue constraint under wind load and gear tooth manufacturing uncertainties. Formulations and numerical procedure for the reliability analysis to estimate the probability of failure of a wind turbine are explained in Section 5.2, while reliability analysis results are presented in Section 5.3 for the baseline drivetrain design as well as the DDO optimum design obtained in Chapter 4. For each design, effect of the wind load uncertainty, gear tooth manufacturing uncertainty, and both uncertainties on the probability of failure is discussed.

5.2 Reliability Analysis Using Monte Carlo Simulation

In the deterministic design optimization discussed in the previous chapter, wind load uncertainty is incorporated by an averaged joint PDF defined by $\overline{f}_{VI}^{ij}(v_{10}^i, i_{10}^j) = \left(\sum_{l=1}^{N_{VI}} f_{VI}^{ijl}(v_{10}^i, i_{10}^j; \mathbf{y}^l) \right) / N_{VI}$ using Monte Carlo simulation (MCS), where $\mathbf{y} = [C \quad k \quad a \quad b \quad \tau]^T$ characterizes uncertainty of PDF parameters of the joint PDF wind load uncertainty model. That is, 20-year fatigue damage of a gear is approximated as $D_{20\text{year}}(\mathbf{d}) = 20 D_{1\text{year}}(\mathbf{d})$ using the one-year damage $D_{1\text{year}}(\mathbf{d})$ for design variable $\mathbf{d}$. However, in reality, wind variability changes over 20 years, and randomness of PDF parameters $\mathbf{y} = [C \quad k \quad a \quad b \quad \tau]^T$ need to be considered over 20 years. That is, a random vector for PDF parameters $\mathbf{Y}$ for 20 years can defined as [101]

$$\mathbf{Y} = [\mathbf{C}^T \quad \mathbf{k}^T \quad \mathbf{a}^T \quad \mathbf{b}^T \quad \boldsymbol{\tau}^T]^T \tag{5.1}$$

where the preceding vector contains 20 random variables for each parameter as $\mathbf{C} = [C^1 \; C^2 \cdots C^{20}]^T$, $\mathbf{k} = [k^1 \; k^2 \cdots k^{20}]^T$, $\mathbf{a} = [a^1 \; a^2 \cdots a^{20}]^T$, $\mathbf{b} = [b^1 \; b^2 \cdots b^{20}]^T$, and $\boldsymbol{\tau} = [\tau^1 \; \tau^2 \cdots \tau^{20}]^T$. Accordingly, the 20-year gear contact fatigue damage considering wind load and gear manufacturing uncertainties can be defined as

$$D_{20\text{year}}(\mathbf{d},\mathbf{Y}) = 6\times 3000\sum_{l=1}^{20}\sum_{i=1}^{n_v}\sum_{j=1}^{n_i} f_{VI}^{ijl}(v_{10}^i, i_{10}^j; C^l, k^l, a^l, b^l, \tau^l) D_{10\,\min}^{ij}(\mathbf{d}, v_{10}^i, i_{10}^j)\Delta v_{10}\Delta i_{10} \quad (5.2)$$

where $\mathbf{d}$ is a vector of random design variables using normal distribution; $D_{10\,\min}^{ij}(\mathbf{d}, v_{10}^i, i_{10}^j)$ is the 10-minute fatigue damage for random design variable $\mathbf{d}$; and $f_{VI}^{ijl}(v_{10}^i, i_{10}^j; C^l, k^l, a^l, b^l, \tau^l)$ is the joint PDF of annual wind load determined for $(C^l, k^l, a^l, b^l, \tau^l)$ every year for 20 years (i.e., $l = 1,\cdots,20$). Using the preceding equation, the probability of gear contact fatigue failure can be evaluated using sampling-based reliability method as follows [101]:

$$P_F(D_{20\text{year}}(\mathbf{d};\mathbf{Y}) > 1) \cong \frac{1}{NMCS}\sum_{i=1}^{NMCS} I_{\Omega_F}[\mathbf{d}^i, \mathbf{Y}^i] \quad (5.3)$$

where $\mathbf{d}^i$ and $\mathbf{Y}^i$ are, respectively, the *i*-th realization of $\mathbf{d}$ and $\mathbf{y}$ selected randomly from the corresponding PDFs; *NMCS* is the number of realizations for MCS; and Ω_F is the failure domain defined by $D_{20\text{year}}(\mathbf{d};\mathbf{Y}) > 1$; and I_{Ω_F} is an indicator function defined as follows:

$$I_{\Omega_F}(\mathbf{d}^i, \mathbf{Y}^i) = \begin{cases} 1 & \text{for } [\mathbf{d}^i, \mathbf{Y}^i] \in \Omega_F \\ 0 & \text{otherwise} \end{cases} \quad (5.4)$$

It is important to notice here that $D_{20\text{year}} > 1$ indicates that fatigue life is less than 20 years. If the design variables are treated deterministically, the probability of gear contact fatigue failure can be obtained as

$$P_F(D_{20\text{year}}(\mathbf{Y}) > 1) \cong \frac{1}{NMCS}\sum_{i=1}^{NMCS} I_{\Omega_F}[\mathbf{Y}^i] \quad (5.5)$$

On the other hand, if the wind load is treated as an averaged PDF $\overline{f}_{VI}^{ij}(v_{10}^i, i_{10}^j)$ as in the deterministic optimization discussed in Chapter 4, the 20-year gear contact fatigue damage can be approximated as

$$D_{20\text{year}}(\mathbf{d}) = 20 D_{1\text{year}}(\mathbf{d}) \quad (5.6)$$

where the one-year gear contact fatigue damage is defined using Riemann integral as

$$D_{1\text{year}}(\mathbf{d}) = 6\times 3000\sum_{i=1}^{n_v}\sum_{j=1}^{n_i} \overline{f}_{VI}^{ij}(v_{10}^i, i_{10}^j) D_{10\,\min}^{ij}(\mathbf{d}, v_{10}^i, i_{10}^j)\Delta v_{10}\Delta i_{10} \quad (5.7)$$

It is important to notice here that variability of C, k, a, b, and τ over 20 years are approximated using the averaged joint PDF $\bar{f}_{VI}^{ij}(v_{10}^{i}, i_{10}^{j})$ in this special case, while different C, k, a, b, and τ are selected every year in Eq. 5.2 for the sake of generality. Accordingly, the probably of failure considering design variable uncertainty using the averaged joint PDF of wind load can be defined as:

$$P_F(D_{20\text{year}}(\mathbf{d}) > 1) \cong \frac{1}{NMCS} \sum_{i=1}^{NMCS} I_{\Omega_F}[\mathbf{d}^i] \tag{5.8}$$

It is important to notice here that use of MCS requires a lot of computational power since 10-minute dynamics simulations of drivetrains have to be carried out for all the realizations of random design vectors **d** to evaluate 20-year contact fatigue damage using MCS. For this reason, surrogate models are introduced to circumvent time-consuming contact fatigue damage calculation associated with design variable uncertainty. To this end, N realizations of random design vectors are selected from the PDFs of the design variables (N=14 in this study) and the gear dynamic simulation is carried out N times to obtain N sets of 10-minute gear contact fatigue damage. Using the N sets of 10-minute gear contact fatigue damage, surrogate models are generated using dynamic kriging method [102,103] in RAMDO [96]. With the surrogate model, 10-minute gear contact fatigue damages can be obtained for realizations of random design vectors using MCS in the reliability analysis.

5.3 Reliability Analysis Results and Discussion

Using the procedure discussed in Section 5.2, the reliability analysis is carried out for the baseline design and DDO optimum design obtained in Chapter 4. The face width and tip relief of sun gear of low-speed stage planetary gear for both designs are summarized in Table 5.1. Uncertainty of design variables are assumed to be normal distribution. Please notice here that, in the baseline design, the tip relief is not treated as a design variable. Means of the design variables are assumed as shown in Table 5.1, while the standard deviations are estimated from the design tolerances [104-106] as presented in Table 5.2. 50,000 realizations of random design vectors are selected from the PDFs of the design variables for MCS in the reliability analysis and 50,000 10-minute contact fatigue damages $D_{10\,\text{min}}^{ij}(\mathbf{d}, v_{10}^{i}, i_{10}^{j})$ are evaluated using the surrogate model. For wind load uncertainty,

Table 5.1 Baseline and DDO optimum designs

	Baseline design	DDO optimum design
Face width (mm)	220	202
Tip relief (μm)	0	41

Table 5.2 Standard deviations and tolerances of the design variables

	Standard deviation	Tolerance
Face width (mm)	1.2	3.6
Tip relief (μm)	1.5	4.5

Table 5.3 Reliability analysis results

Uncertainties	Probability of failure	
	Baseline design	DDO optimum design
Case 1	91.81 %	49.06 %
Case 2	100.00 %	52.65 %
Case 3	91.70 %	50.49 %

50,000 realizations of random vectors **C**, **k**, **a**, **b** and **τ** are also created for MCS, and each realization contains 20 sets of (C,k,a,b,τ) used to generate 20 annual wind joint PDFs. With this procedure, 50,000 20-year fatigue damages are calculated to find the probability of failure using Eq. 5.3.

The reliability analysis results are shown in Table 5.3 for the baseline and DDO designs. For each design, the following three cases are considered:

Case 1: Wind load uncertainty over 20 years is considered, but design variable uncertainty is not considered, i.e., the probability of failure is evaluated by $P_F(D_{20\text{year}}(\mathbf{Y})>1)$.

Case 2: Wind load uncertainty is considered as an averaged joint PDF, but design variable uncertainty is considered by normal distribution, i.e., the probability of failure is evaluated by $P_F(D_{20\text{year}}(\mathbf{d})>1)$.

Case 3: Wind load uncertainty over 20 years as well as design variable uncertainty are considered, i.e., the probability of failure is evaluated by $P_F(D_{20\text{year}}(\mathbf{d};\mathbf{Y})>1)$.

It is observed from Table 5.3 that the probability of failure of the baseline design is close to 100 % and is much higher than that of the DDO design for all the three cases. In particular, the baseline design under the averaged wind load variation model (Case 2) leads to 100 % probability of failure and the product life is estimated as only 15 years. On the other hand, if the wide spatiotemporal wind load uncertainty over 20 years is considered (Case 1 and 3), the probability of failure during 20-year operation decreases to approximately 92 %. On the other hand, the probability of failure of DDO design is approximately 50% as expected since DDO design is obtained by treating design variables deterministically. Similar to the baseline design results, probability of failure for Case 2 is higher than Case 1 and 3, indicating that use of the averaged joint PDF leads to an underestimation of reliability of design slightly. For this reason, consideration of wind load and design variable (manufacturing error) uncertainties is of crucial importance in not only the reliability analysis, but also the reliability-based design optimization to ensure the target reliability.

CHAPTER 6
RELIABILITY-BASED DESIGN OPTIMIZATION OF WIND TURBINE DRIVETRAIN UNDER WIND LOAD UNCERTAINTY

6.1 Introduction

In this chapter, reliability-based design optimization (RBDO) of a wind turbine drivetrain, under wind load and gear design variable uncertainties, is carried out to achieve an optimum gear design that meets 20-year service life with a target reliability while minimizing the cost (weight). In the deterministic design optimization (DDO) discussed in Chapter 4 and 5, the probability of failure under the spatiotemporal wind load uncertainty as well as the gear design variability turned out to be approximately 50 %. To improve the design reliability (i.e., decrease the probability of failure), a numerical procedure for RBDO of wind turbine drivetrains is developed in this chapter.

6.2 Reliability-Based Design Optimization

The objective of RBDO is to find an optimum design within the feasible design domain defined by the constraint functions considering randomness of input variables. For a two-dimensional design problem given by two design variables X_1 and X_2 as illustrated in Fig. 6.1, a deterministic optimum stays on the limit state line that ensures the constraint equation being zero. The ellipse shown in the figure accounts for the variability of variables X_1 and X_2 within twice of their standard deviations (i.e., two sigma). A part of the ellipse outside the feasible region shown in red area corresponds to the probability of failure, which is approximately 50% for the deterministic design optimization as demonstrated in Chapter 5. On the other hand, in the RBDO, the center of ellipse is shifted toward the feasible region such that the probability of failure can be further reduced while minimizing the objective function. The reliable optimum is obtained such that the target probability of failure is achieved while minimizing the objective function. That is, an RBDO problem is formulated as follows:

$$\begin{aligned} &\text{Minimize} && \text{Obj}(\mathbf{d}) \\ &\text{Subject to} && P[G_j(\mathbf{X}) > 0] \le P_{F_j}^{Tar},\ j = 1,\ldots,N_c \\ &&& \text{for}\quad \mathbf{d}^L \le \mathbf{d} \le \mathbf{d}^U, \mathbf{d} \in \mathbb{R}^{N_{DV}}, \mathbf{X} \in \mathbb{R}^N \end{aligned} \tag{6.1}$$

where **d** is the N_{DV}-dimensional design variable vector; **X** is the N-dimensional random variable vector which includes not only the random design variables, but also the random system parameters; Obj indicates the objective function; G_j is the j-th constraint function; $P[G_j(\mathbf{X})]$ is the probability of failure of the j-th constraint; $P_{F_j}^{Tar}$ is the target probability of failure of the j-th constraint; and N_c is the number of constraint equations. The RBDO process attempts to minimize the objective function while making the probability of failure less than or equal to the target the probability of failure. The RBDO optimum design is obtained when all the convergence criteria are satisfied.

There are two approaches in the reliability analysis (i.e., $P[G_j(\mathbf{X})]$) to calculate the probability of failure for given design: the sensitivity-based reliability analysis and the sampling-based reliability analysis. The sensitivity-based reliability analysis transforms the input random variables into uncorrelated standard Gaussian random variables and approximates the nonlinear performance measure by Taylor series expansion [58, 59]. The Taylor series expansion requires the calculation of the sensitivity of the constraint measure. However, for many engineering applications including the wind turbine drivetrain contact fatigue damage considered in this study, the sensitivity of the constraint function is difficult obtain since the constraint function is an implicit function of design variables. For this reason, the sampling-based reliability analysis approach is selected in this study. In the

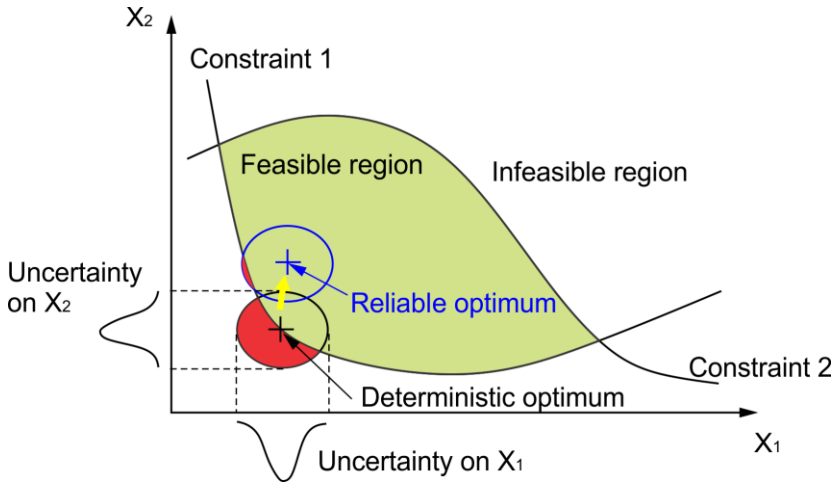

Figure 6.1 Conceptual two-dimensional RBDO problem

sampling-based reliability analysis, the probability of failure is directly calculated using MCS method, which uses MCS samples taken from the joint PDF of input random variables. The probability of gear contact fatigue failure can be calculate using Eq. 5.3 to account for uncertainties of both design variables and wind loads. Equation 5.5 is used if only wind load uncertainty is considered, while Eq. 5.8 is employed if only design variable uncertainty is considered. The accuracy of the calculated probability of failure depends on the number of MCS samples, *NMCS*. The percentage error of the calculated probability of failure can be defined based on the 95% confidence interval as [101]

$$\varepsilon\,\% = \sqrt{\frac{(1-P_F^{Tar})}{NMCS \times P_F^{Tar}}} \times 200\,\% \tag{6.2}$$

where P_F^{Tar} is the target probability of failure. It can be seen from Eq. 6.2 that the error is reduced as *NMCS* increases. Table 6.1 summarizes the *NMCS* required to meet 2 % error for different target probability of failure P_F^{Tar}, indicating that a larger number of MCS samples is needed in the case that a smaller target probably of failure is desired. It is important to notice here that constraint functions need to be evaluated *NMCS* times and use of the large number of MCS samples causes a computational burden, making the RBDO calculation process very computational intensive and practically infeasible in the worst case. In particular, for the wind turbine drivetrain considered in this study, the contact fatigue damage needs to be evaluated at each DOE point using the nonlinear multibody dynamics simulation for various 10-minute wind scenarios. In order to overcome the computational difficulty, surrogate models are used in this study for the sampling-based reliability-based design optimization.

Table 6.1 *NMCS* required to meet 2 % error for different target probability of failure P_F^{Tar}

P_F^{Tar}	ε %	*NMCS*
0.5	2.0	10,000
0.2	2.0	40,000
0.1	2.0	90,000
0.05	2.0	190,000
0.02275	2.0	429,560

6.3 Surrogate Model

A surrogate model, also called a response surface model, meta-model, or emulator, is widely used to obtain approximated responses to input variables in various design optimization problems. A surrogate model is constructed using a data-driven approach for a limited number of design of experiment (DOE) points and their system responses obtained from experiments or simulations. Using this data, the approximated input-output behavior can be constructed. There are a wide variety of surrogate models proposed in the past such as polynomial response surfaces [61], support vector regression and classifiers (SVR, SVC) [62], neural networks [63], radial basis function [64], and kriging predictors [65].

The kriging method has been widely used due to its capability of dealing with highly nonlinear problems [102]. The basic idea of this method is to predict a function value at a given design point by calculating a weighted average of the response values of the function in the neighborhood of a given point based on a Gaussian process governed by prior covariance. For instance, for *n* sample points $\mathbf{x}_s = [\mathbf{x}_1, \mathbf{x}_2, ..., \mathbf{x}_n]^T$, the *n* responses $\mathbf{y}_s = [y(\mathbf{x}_1), y(\mathbf{x}_2), ..., y(\mathbf{x}_n)]^T$ are modeled as [102]:

$$\mathbf{y}_s = \mathbf{F}\boldsymbol{\beta} + \mathbf{e} \tag{6.3}$$

$\mathbf{F}\boldsymbol{\beta}$ is the mean structure of the response, where $\mathbf{F} = [\mathbf{f}(\mathbf{x}_i)]$ $\{\mathbf{f}(\mathbf{x}_s) = [f_k(\mathbf{x}_s)],\ i = 1,...,n,\ \text{and}\ k = 1,...,K\}$ is an $n \times K$ model matrix, and $\mathbf{f}(\mathbf{x}_s)$ represents user-selected basis functions; $\boldsymbol{\beta} = [\beta_1, \beta_2, ..., \beta_K]^T$ is the vector of the regression coefficients; $\mathbf{e} = [e(\mathbf{x}_1), e(\mathbf{x}_2), ..., e(\mathbf{x}_n)]^T$ is a realization of the stochastic process; and $e(\mathbf{x})$ has zero mean and a covariance that is equal to $\sigma^2 R(\boldsymbol{\theta}, \mathbf{x}_i, \mathbf{x}_j)$, where σ^2 is the process variance and $R(\boldsymbol{\theta}, \mathbf{x}_i, \mathbf{x}_j)$ is the correlation function of the stochastic process, $\boldsymbol{\theta} = [\theta_1, \theta_2, ..., \theta_m]^T$ is the process correlation parameter vector of dimension *m*. Having determined $\boldsymbol{\theta}$ through the maximum likelihood estimator (MLE) [102], $\boldsymbol{\beta}$ can be obtained from the generalized least squares regression and then response of a kriging model can be obtained through the interpolation of *n* sample points as

$$\hat{y}(\mathbf{x}) = \mathbf{f}^T\boldsymbol{\beta} + \mathbf{r}^T\mathbf{R}^{-1}(\mathbf{y}_s - \mathbf{F}\boldsymbol{\beta}) \tag{6.4}$$

where $\mathbf{f} = [f_k(\mathbf{x})]^T$ $(k = 1,...,K)$ is the basis-function values evaluated at the point $\mathbf{x}$ and $\mathbf{r} = [R(\boldsymbol{\theta}, \mathbf{x}_1, \mathbf{x}),...,R(\boldsymbol{\theta}, \mathbf{x}_n, \mathbf{x})]^T$. A standard kriging method constructs the mean structure $\mathbf{F}\boldsymbol{\beta}$ using a fixed set of polynomial basis functions, which may not be accurate enough for highly nonlinear problem. The dynamic kriging method proposed in the literature [102], on the other hand, obtains an optimum mean structure using basis functions selected by a genetic algorithm, and an accurate optimum of the correlation parameters $\boldsymbol{\theta} = [\theta_1, \theta_2,..., \theta_m]^T$ are obtained through the generalized pattern search algorithm. Thus, the dynamic kriging method can, in general, create more accurate surrogate model than the conventional kriging method [107]. In this study, the dynamic kriging method is utilized to generate a surrogate model for prediction of the wind turbine gear contact fatigue damage.

The accuracy of a system response predicted by a surrogate model depends not only on the number of sampling points, but also on the location of sampling points. In the wind turbine drivetrain model, the CPU time of the 10-minute dynamic simulation under wind load uncertainty (35 wind scenarios considered) is approximately 12 hours for one DOE point using a server computer (two 3.1GHz Intel Xeon E5-2687W CPUs having 20 cores each, i.e., 40 logical processors, 768GB RAM). In general, a local surrogate model is created at the current design point within the two sigma range of design variables [101]. It is, however, important to notice here that the design point could move to a point beyond the two sigma range in an iterative RBDO process, thus the local surrogate model needs to be generated at each design iteration of RBDO, making the RBDO process very computationally expensive. Suppose that 14 DOE points are used for generating a local surrogate model and 10 design iterations are assumed to be needed to obtain a RBDO optimum design; then the CPU time for RBDO amounts to roughly 1,680 hours (70 days).

To address this fundamental computational issue in wind turbine drivetrain RBDO, an intermediate surrogate model covering the range from the DDO optimum to the expected RBDO optimum is utilized in this study. That is, surrogate models are generated once prior to the RBDO process and used throughout the RBDO iteration process. To ensure its accuracy, 50 DOE points are selected using Latin Centroidal Voronoi Tessellations (LCVT) sampling method with hypercube window and the window size is

selected in the range of twelve sigma as shown in Fig. 6.2. The area of this window covers approximately one ninth of the entire design variable domain. It is important to notice here that the center of the intermediate window is intentionally shifted by three sigma of the face width from the DDO optimum as shown in Fig. 6.2 as "+" point since it is unlikely that the gear face is decreased from the DDO optimum to meet the higher target reliability in RBDO. The window has to be appropriately selected such that the design variables taken in the RBDO iterative process lie within the window to assure the accuracy. Furthermore, the window size has to be small enough to minimize the number of DOE points to reduce the computational cost for the surrogate model generation. The numerical procedure for generating the surrogate model is summarized as follows:

(1) At the DDO optimum design point of the wind turbine drivetrain, 50 DOE points are created using truncated Gaussian sampling (TGS) method with hypercube window in the twelve sigma range.

(2) The wind turbine drivetrain dynamics simulation is carried out for 50 DOE points considering wind load uncertainty to obtain 50 fatigue damage response vectors. Each response vector contains 10-minute gear contact fatigue damages for all 35 wind load cases considered in the wind load uncertainty model. Each wind load scenario needs a surrogate model that predicts the corresponding 10-minute contact fatigue damage for the give design point.

(3) Using the 10-minute fatigue damage response vectors for 50 DOE points, 35 surrogate models associated with 35 wind load scenarios are generated by the dynamic kriging method.

It is imporatant to notice here that since the intermediate surrogate models are generated only once, an estimated CPU time using the above-mensioned server computer is reduced to 25 days if 50 DOE points are used. This leasds to a significant reduction in CPU time as compared to that of local surrogate models. Furthermore, if simulations at all DOE points can run concurrently using computer that has a sufficient number of cores, the CPU time using the intermeduate surrogate models is futher reduced to 12 hours. On thet other hand, CPU time of the local surrogate models is $12 \times N$ hours, where N is the number iterations required to complete the RBDO process.

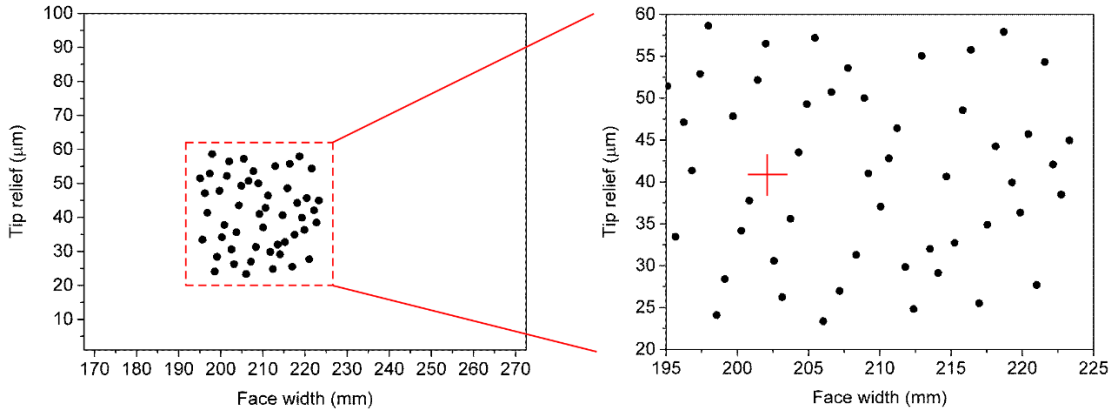

Fig.6.2 Randomly generated 50 DOE ponits for an intemediate surrogate model;
+ : DDO optimum design

6.4 RBDO of Wind Turbine Drivetrain

In this section, a numerical procedure for the RBDO of wind turbine drivetrain under wind load uncertainty and gear manufacturing variability is developed. First, a formulation of wind turbine drivetrain RBDO is presented and then an entire numerical procedure developed for RBDO of wind turbine drivetrains is presented.

6.4.1 Formulation of Wind Turbine Drivetrain RBDO

In reference to Eq. 6.1, RBDO of wind turbine drivetrains is formulated as follows:

$$\begin{aligned} &\text{Minimize} \quad J(\mu_B) = M_{ring}(\mu_B) + M_{sun}(\mu_B) + 3M_{planet}(\mu_B) \\ &\text{Subject to} \quad P[D_{20\,year}(B, \delta_a; \mathbf{Y}) > 1] \le P_F^{Tar} \\ &\qquad \text{for} \quad \mu_B^L \le \mu_B \le \mu_B^U \text{ and } \mu_{\delta_a}^L \le \mu_{\delta_a} \le \mu_{\delta_a}^U \end{aligned} \tag{6.5}$$

where μ_B and μ_{δ_a} are means of the random face width B and the random tip relief amount δ_a of the sun gear, respectively; the lower and upper bounds of the design variables are same as the deterministic design optimization in Chapter 4 (i.e., $167.5 \le \mu_B \le 272.5$ mm and $0 \le \mu_{\delta_a} \le 100\,\mu$m); the cost function $J(\mu_B)$ is defined as the total mass of the planetary stage gears consisting of a ring gear, a sun gear and three planet gears; **y** is the random wind load vector including 20 sets of (C, k, a, b, τ); and $D_{20\,year}(B, \delta_a; \mathbf{Y})$ is the 20-year

contact fatigue damage of the sun gear. For each of the MCS design point, $D_{20\,year}$ is evaluated as follows:

$$D_{20\,year}(\hat{B}^h, \hat{\delta}_a^h; \hat{\mathbf{y}}^h) = 6 \times 3000 \sum_{l=1}^{20} \sum_{i=1}^{n_v} \sum_{j=1}^{n_i} f_{VI}^{ijlh}(v_{10}^i, i_{10}^j; C^{lh}, k^{lh}, a^{lh}, b^{lh}, \tau^{lh}) D_{10\,\min}^{ij}(\hat{B}^h, \hat{\delta}_a^h; v_{10}^i, i_{10}^j) \Delta v_{10} \Delta i_{10}$$

$$\text{for } h = 1, ..., NMCS \tag{6.6}$$

where $\hat{B}^h$ and $\hat{\delta}_a^h$ are realizations of random face width B and tip relief amount δ_a, respectively; and $\hat{\mathbf{y}}^h$ is the realization vector of random wind load parameters. The probabilistic constraint $P[D_{20\,year}(B, \delta_a; \mathbf{Y}) > 1]$ is imposed to ensure that the probability of contact fatigue life being shorter than 20 years is smaller than the target probability of failure P_F^{Tar} .

6.4.2 Numerical Procedure of Wind Turbine Drivetrain RBDO

A numerical procedure of wind turbine drivetrain RBDO using the intermediate surrogate model is summarized as follows:

Step 1: As shown in Fig. 6.3, using the DDO optimum design (face width = 202 mm, tip relief = 41 μm) obtained in Chapter 4, 50 DOE points are randomly generated using the truncated Gaussian sampling (TGS) method with hypercube window in the twelve sigma range. The intermediate surrogate models of the sun gear 10-minute contact fatigue damages are generated using the dynamic kriging method. The numerical procedure for generating the surrogate models is summarized in Fig. 6.4. For each DOE point, the 10-minute fatigue damages for all the wind load conditions (35 scenarios) under consideration are calculated and the obtained 10-minute fatigue damages are inputted to RAMDO software to generate 35 surrogate models associated with 35 wind load conditions using the dynamic kriging method.

Step 2: The RBDO process starts from the DDO optimum design. At every RBDO design, NMCS realizations of designs are created considering the manufacturing variabilities as defined in Table 5.2. The NMCS realizations are inputted to the 35 surrogate models to obtain the NMCS 10-minute fatigue damage tables containing 35 10-minute fatigue damages under 35 wind load conditions.

Step 3: The NMCS realizations of 20 sets of (C, k, a, b, τ) are defined using the PDFs, and NMCS × 20 wind load probability tables are created. Each table contains the probabilities of 35 wind load conditions.

Step 4: The NMCS 20-year fatigue damages are calculated using Eq. 6.6, and then the probabilistic constraint is evaluated inside RAMDO at the current design. If the convergence criteria is met, the RBDO iteration stops and an optimum design is obtained. Otherwise, the design is updated and then continues the RBDO process by repeating Step 2 to 4 until the RBDO optimum design is achieved.

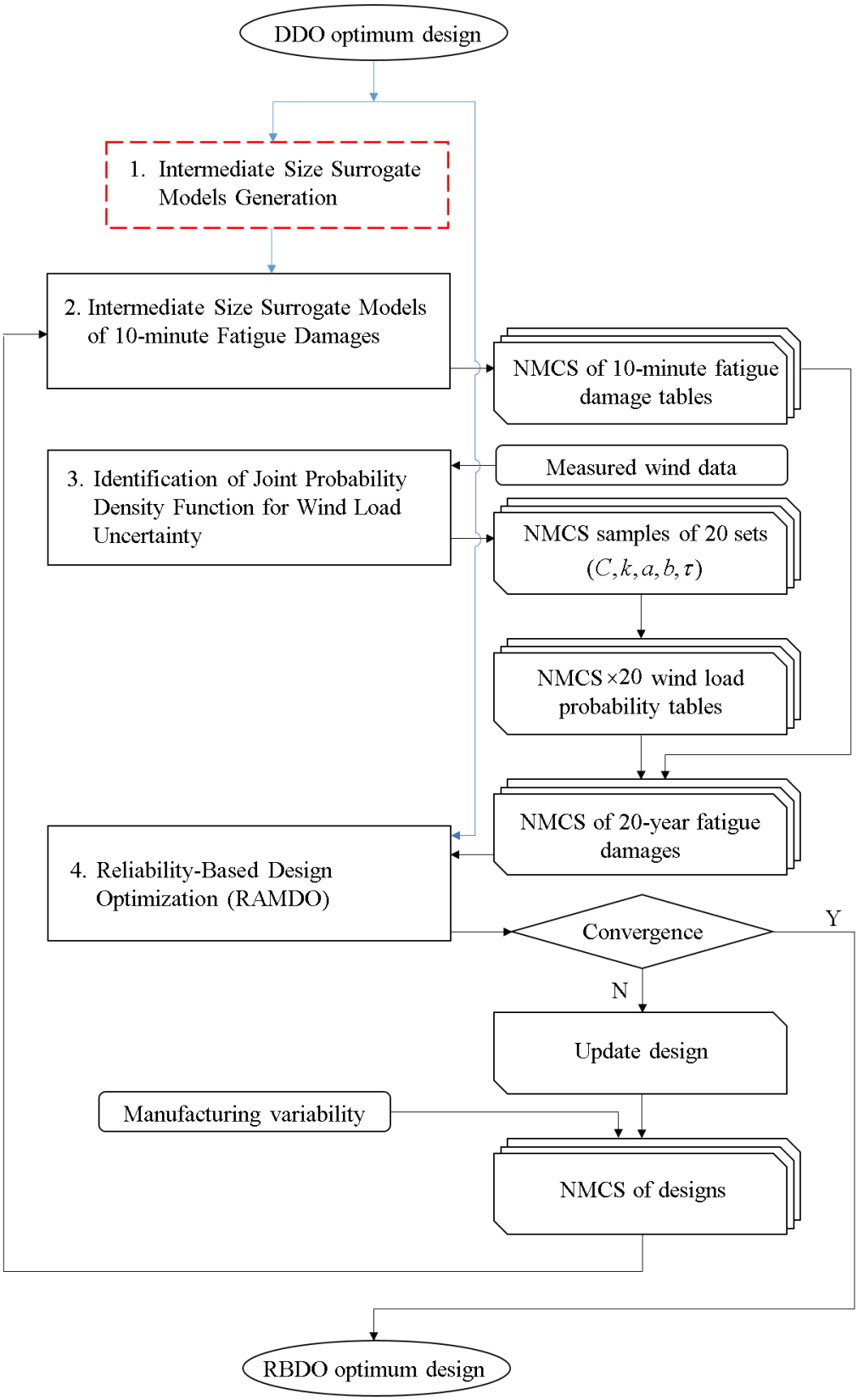

Fig.6.3 Flowchart of the RBDO process

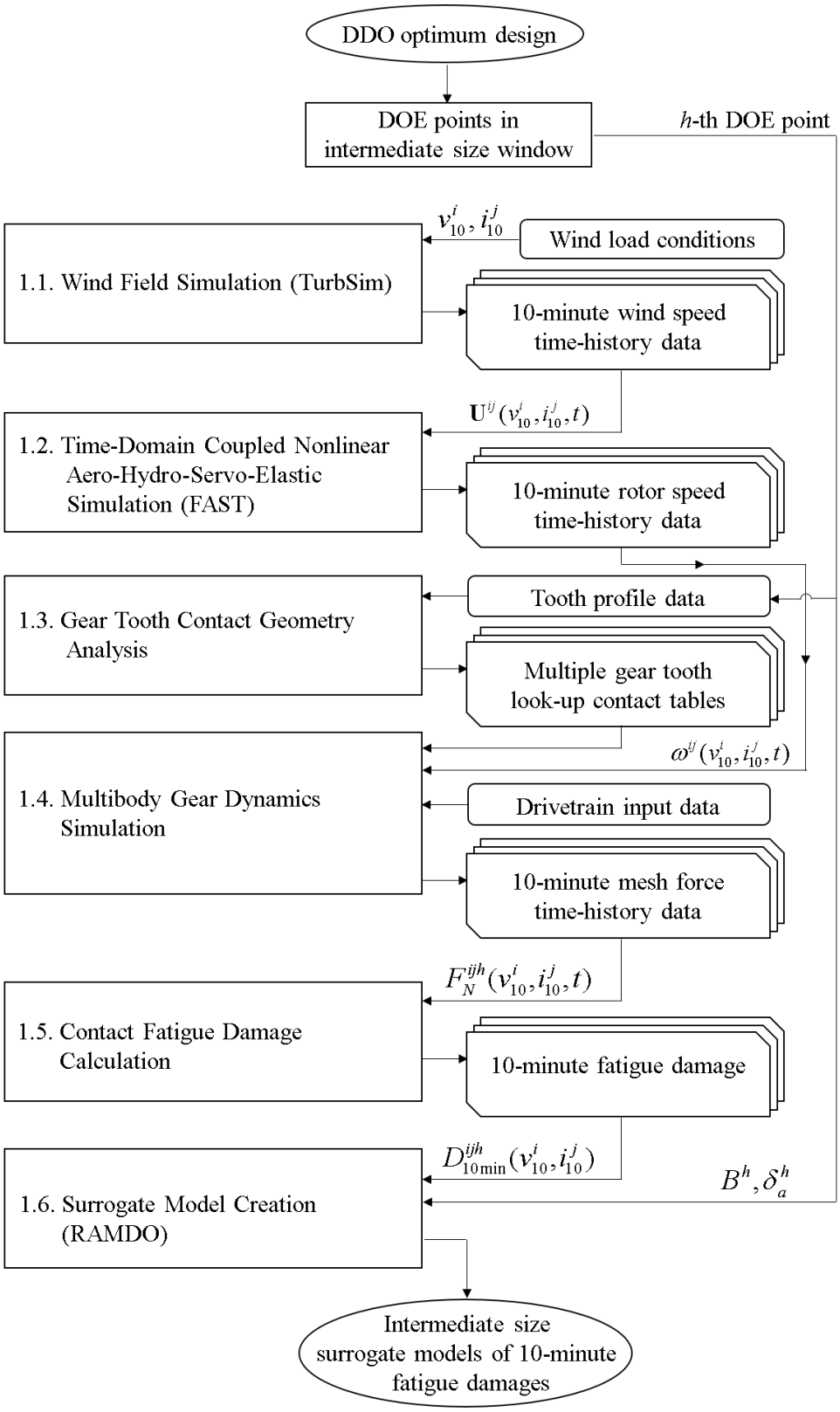

Fig.6.4 Flowchart of surrogate model generation

6.5 RBDO Results and Discussions

Starting from the DDO optimum design (face width = 202 mm, tip relief = 41 μm), the reliability-based design optimization is carried out using RAMDO software on a server computer (two 3.1GHz Intel Xeon E5-2687W CPUs having 20 cores each, i.e., 40 logical processors, 768GB RAM). 500,000 MCS realizations of design points are created based on the joint PDF of the face width B and the tip relief amount δ_a at each design iteration to calculate the probability of failure and design sensitivities of the probabilistic constraints. The standard deviations of B and δ_a are assumed as previously presented in Table 5.2. Three different target probabilities of failure ($P_F^{Tar} = 10\%$, $P_F^{Tar} = 5\%$ and $P_F^{Tar} = 2.275\%$) are considered.

The RBDO results are presented in Table 6.2 and compared with the baseline design as well as the DDO optimum design. It is observed from this table that the face width and tip relief amount increase from the DDO design to meet the target probability of failure. This leads to an increase in weight. However, as compared to the baseline design exhibiting 91.7 % probability of failure (8.3 % reliability), the weight is increased by only 1.4%, while the probability of failure is improved significantly from 91.7 % to 2.275 % (i.e., 97.725 % reliability) in the case of $P_F^{Tar} = 2.275\%$ (two sigma quality level). It is also important to notice that 5 % probability of failure is achieved without increasing the weight

Table 6.2 RBDO result comparison with different P_F^{Tar}

	Baseline design	DDO design w/ tip relief	RBDO design w/ tip relief		
			$P_F^{Tar} = 10\%$	$P_F^{Tar} = 5\%$	$P_F^{Tar} = 2.275\%$
Face width (mm)	220	202	216	220	223
Tip relief (μm)	0	41	51	53	54
Fatigue life	15 yrs	20 yrs	20 yrs	20 yrs	20 yrs
Probability of failure	91.700 %	50.490 %	9.993 %	5.000 %	2.275 %
Normalized mass	1.000	0.916	0.983	1.000	1.014

(i.e., without increase the face width) from the baseline design by an optimum tip relief of 53 μm. These results clearly indicate the importance of incorporating the tip relief as a design variable and justify needs for the gear dynamics simulation capability that accounts for micro-geometry of gear tooth contact. This, however, does not mean that a larger tip relief is always preferred since an optimum tip relief amount depends on stochastic wind loads and an optimum tip relief cannot be found deterministically.

To discuss how the two design variables converge to the RBDO optimum, change in the face width and the tip relief is presented in Fig. 6.5 (a), 6.6 (a) and 6.7 (a) for $P_F^{Tar} =$ 10 %, 5 %, and 2.275 %, respectively. Furthermore, the objective function and the probability of failure are also presented in Fig. 6.5 (b), 6.6 (b) and 6.7 (b) as a function of the iteration step. It is observed from these figures that the face width and the tip relief increase sharply in the first few iterations to meet the target probability of failure. It is important to notice here that an increase in the tip relief prevents a larger increase in the face width that results in a larger increase of the objective function. In the case of $P_F^{Tar} =$ 10 % and 5 %, the face width slightly decreases from the 3rd to 4th iteration to start minimizing the objective function. However, to avoid violating the target probability of failure satisfaction, the tip relief continuously increases to compensate for it. From the 4th to 5th iteration, the tip relief in turn decreases slightly, while the face width increases to find the optimum design. The optimum design variables are found at the 8th iteration. As observed from this convergence curve, these two design variables interplay in the RBDO iteration process to meet the optimum and target reliability conditions.

In order to ensure the accuracy of RBDO optimum obtained using the intermediate surrogate model, the reliability analysis at the RBDO optimum obtained for $P_F^{Tar} = 2.275\%$ is carried out using the local surrogate models. To this end, the following steps are taken:

(1) 50 DOE points are created using the truncated Gaussian sampling (TGS) method with hypersphere local window with the three sigma range as shown in Fig. 6.8. The center of the local window is the RBDO optimum design (face width = 223 mm, tip relief = 54 μm) for $P_F^{Tar} = 2.275\%$.

(2) Local surrogate models are created using the same procedure summarized in Fig. 6.4.

(3) 500,000 MCS design points are created using the joint PDF of the face width and tip relief.

(4) The 500,000 10-minute fatigue damage tables are generated through the local surrogate models and then 500,000 20-year fatigue damages are calculated using Eq. 6.5.

(5) Probability of failure is calculated and compared with the target probability of failure.

The probability of failure calculated using the local surrogate models is 2.5042 %, while the converged value of probability of failure at this RBDO optimum is 2.2748 %. The difference is 0.2294 %, which is small enough, and the RBDO optimum turned out to be on the safer side. This result justifies the use of intermediate surrogate models in the wind turbine drivetrain RBDO involving the high-fidelity gear dynamics simulation. Furthermore, it is demonstrated that the integrated design optimization procedure developed in this study enables the cost effective and reliable design of wind turbines drivetrains.

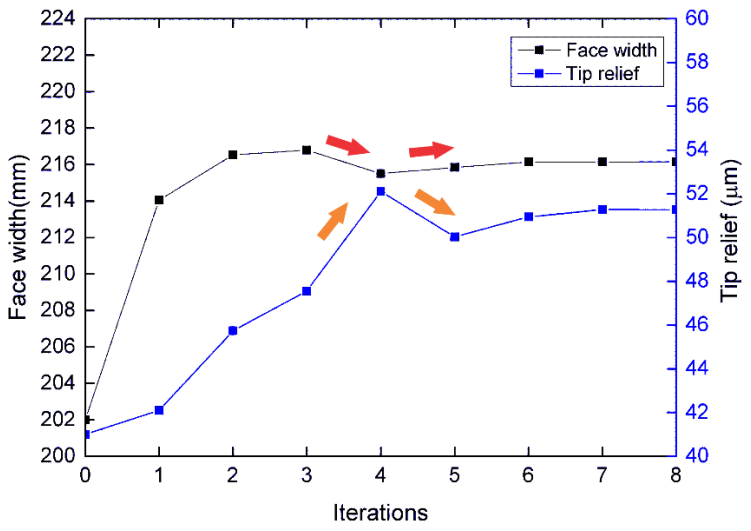

(a) Change of design variables

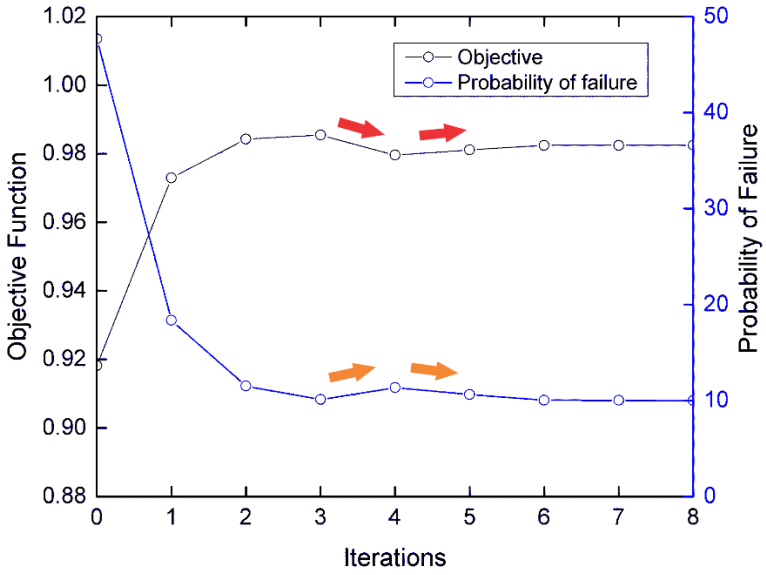

(b) Change of normalized mass and probability of failure

Fig.6.5 RBDO design iteration for $P_F^{Tar} = 10\%$

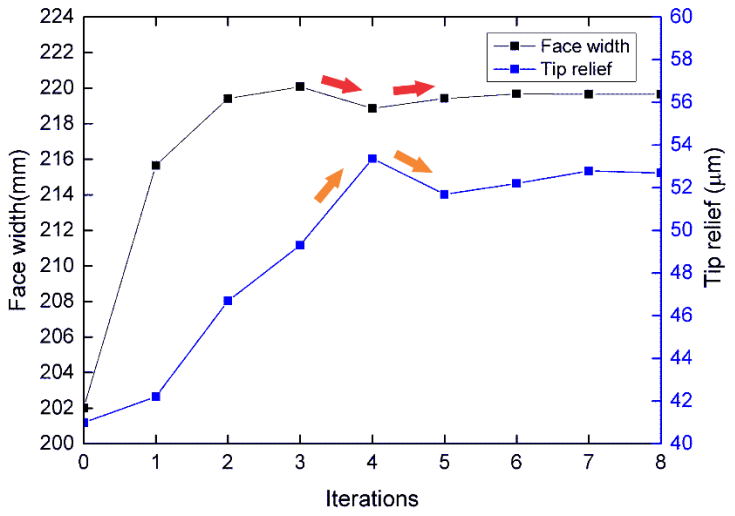

(a) Change of design variables

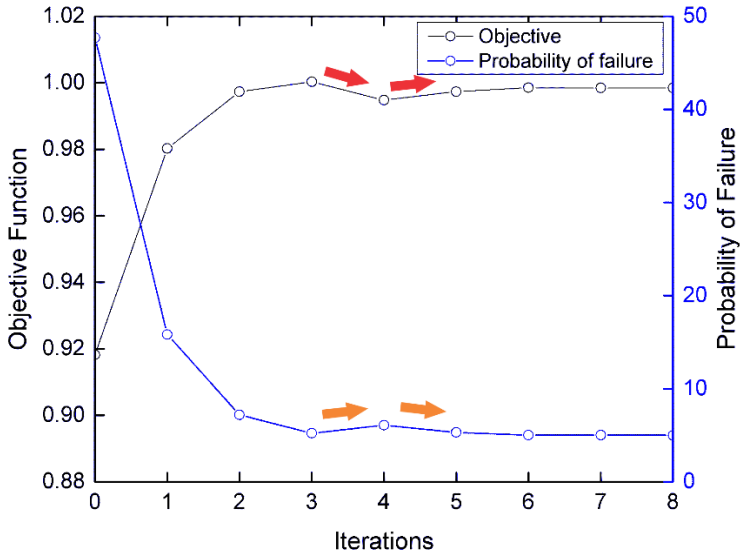

(b) Change of normalized mass and probability of failure

Fig.6.6 RBDO design iteration for $P_F^{Tar} = 5\%$

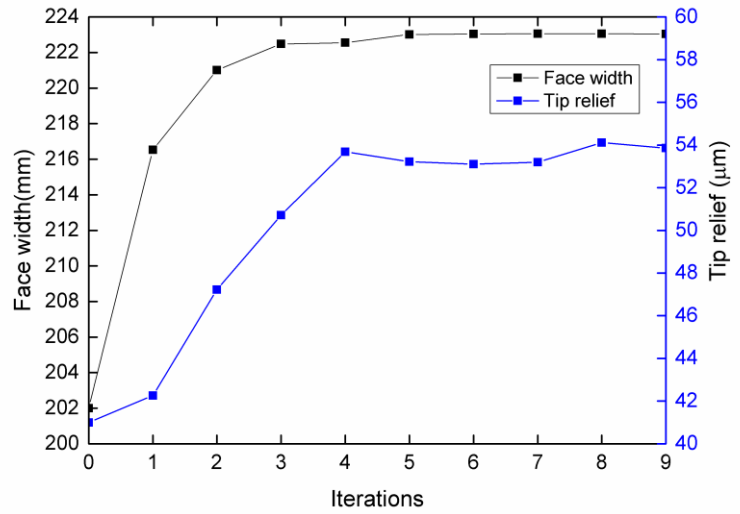

(a) Change of design variables

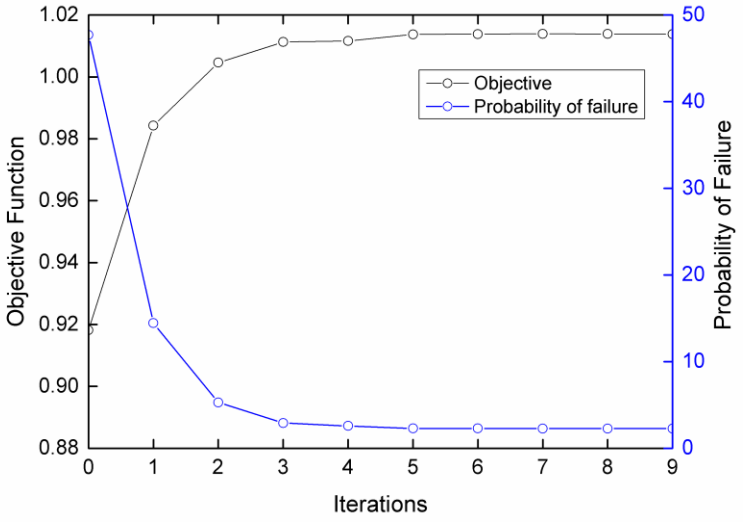

(b) Change of normalized mass and probability of failure

Fig.6.7 RBDO design iteration for $P_F^{Tar} = 2.275\%$

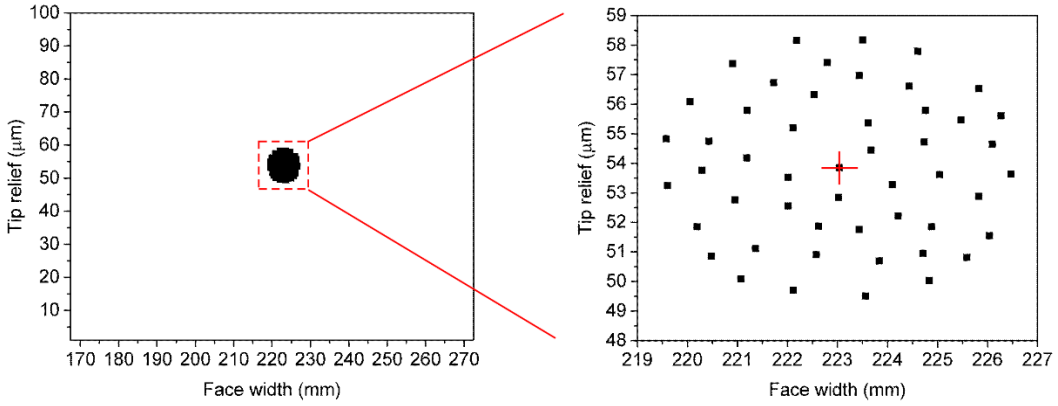

Fig.6.8 Randomly generated 50 DOE ponits in local window at RBDO optimum design;

+ : RBDO optimum design

CHAPTER 7
CONCLUSIONS AND FUTURE WORK

7.1 Summary and Conclusions

Gears in wind turbine drivetrains are subjected to severe cyclical loading due to variable wind loads that are stochastic in nature and the failure rate of drivetrain systems is reported to be relatively higher than the other wind turbine components. For this reason, improving reliability of drivetrain design is one of the key issues to make wind energy more competitive to fossil fuels. However, limited studies have been carried out regarding deterministic and reliability-based design optimization (DDO and RBDO) of wind turbine drivetrains considering wind load as well as manufacturing uncertainties. It requires an extensive numerical procedure involving uncertainty quantification of wind loads as well as manufacturing errors of gears, the contact dynamics of multibody geared systems, probabilistic contact fatigue prediction of gear teeth, and design optimization procedures to meet 20-year service life while minimizing the cost (weight) of drivetrains. This thesis is aimed to develop an integrated multibody dynamics computational framework for the deterministic and reliability-based design optimization of wind turbine drivetrains considering wind load and gear manufacturing uncertainties.

To this end, a numerical procedure for gear dynamics simulation of multibody geared systems is developed first using the tabular contact search method in Chapter 2. Since 10-minute wind data is widely used to characterize the short-term wind speed variability in wind energy industry, 10-minute wind turbine gear dynamic simulations under different wind load conditions are required to evaluate probabilistic contact fatigue life under random wind load. Furthermore, since the tooth contact pressure is sensitive to the gear tooth profile, an accurate description of the tooth profile geometry and precise contact geometry calculation are required and use of a simplified gear contact dynamics model is not suited.

To improve computational efficiency associated with the gear contact dynamics simulation considering precise contact geometry as well as mesh stiffness variations, a tabular contact search algorithm using the combined nodal and non-conformal contact search approach is generalized to gear tooth contact in this study. To predict the jump in contact that can occur for measured tooth profiles with tooth surface imperfections due to

the wear and surface failures, a combined nodal and non-conformal contact search algorithm for gear tooth contact is developed. In this procedure, the nodal search is employed as a global search to provide a rough estimate of the contact point and then the contact point is used as the initial estimate for the non-conformal contact search equations to fulfill the non-conformal contact condition. By doing so, a robust contact search algorithm which allows for detecting an appropriate initial estimate for non-conformal contact search for tooth surfaces with gear geometry imperfections can be achieved.

In the dynamics simulation, the tabular contact search is performed for all the gear teeth positioned in the searching range defined in the look-up table tooth by tooth. This allows for detecting multi-point contact without any iterative procedures. Furthermore, the coordinate transformation between the generalized coordinates and those defined in the look-up table coordinate system introduced in the contact geometry analysis is established. With this transformation, the look-up contact table can be directly applied to any pair of gears in the dynamic simulation. Several numerical examples are presented in Chapter 3 in order to demonstrate the use of the numerical procedure developed in this study. In particular, an accuracy of the mesh stiffness model introduced in this study and the transmission error of gear tooth with tip relief are discussed. A planetary gear model is then introduced to discuss the effect of tooth surface irregularity on mesh force variation. A wind turbine drivetrain model is presented in the last example and is validated against test data provided in the literature.

An integrated numerical procedure for design optimization of wind turbine drivetrains is developed in Chapter 4 using the gear dynamics simulation procedure based on the multi-variable tabular contact search algorithm considering wind load uncertainty. The joint probability density function (PDF) of the 10-minute mean wind speed (V_{10}) and 10-minute turbulence intensity (I_{10}) is introduced to characterize the short-term wind speed variability at a specific location and time. Since the wind load distribution varies at different locations in different years, a wide spatiotemporal variability is considered by identifying PDF of all the joint PDF parameters (C, k, a, b, τ) using 249 sets of wind data and these PDFs are used in the reliability-based design optimization (RBDO). The averaged joint PDF obtained using Monte Carlo simulation (MCS) is used in the deterministic design optimization (DDO). The random time-domain wind speed data is

generated using NREL TurbSim and then inputted into NREL FAST to perform the aero-hydro-servo-elastic simulation of rotor blades under pitch control to predict the transmitted torque and speed of the main shaft of the drivetrain, which are sent to the multibody gear dynamics simulation for contact fatigue prediction.

To account for the wind load uncertainty characterized by the averaged joint PDF of the 10-minute mean wind speed and turbulence intensity, multiple 10-minute drivetrain dynamics simulations are performed. However, multibody drivetrain dynamics simulation becomes a computational burden in the entire design optimization process. In addition, since the tooth contact pressure is sensitive to the gear tooth profile, an accurate description of the tooth profile geometry and precise contact geometry calculation are required, resulting in use of a simplified gear contact dynamics model being not suitable. For this reason, a numerical procedure for the multibody gear dynamics simulation based on the tabular contact search algorithm developed in Chapter 2 is integrated into the gear design optimization procedure considering wind load uncertainty.

The pitting fatigue model based on the Paris equation is then used to predict the contact fatigue life of gear tooth using the maximum contact pressure obtained using the multibody drivetrain dynamics simulation under various 10-minute wind scenarios. Numerical results obtained at different locations and in different years characterized by joint PDF parameters (C, k, a, b, τ) indicate that the predicted contact fatigue life differ significantly and wind load variation plays an important role to realistic estimation of contact fatigue life of wind turbine drivetrain systems.

Using the optimization procedure developed in this study, it is demonstrated for a 750kW GRC wind turbine gearbox model that an optimum tip relief allows for lowering the greatest maximum shear stresses on the tooth surface without relying heavily on face width widening to meet the 20-year fatigue life constraint and it leads to weight reduction by 8.4 %, which leads to more cost-effective design. If only face width is considered as design variable, total weight needs to be increased by 4.7 % to meet the 20-year fatigue life constraint.

Furthermore, the reliability analysis at the DDO optimum design is discussed in Chapter 5 considering the large spatiotemporal wind load uncertainty and gear manufacturing uncertainty. Surrogate models are generated using the dynamic kriging

method in RAMDO software to evaluate the gear contact fatigue damage. One million MCS sets of gear design variables are generated. For each set of design variables, the 10-minute gear contact fatigue damage is obtained from the surrogate models and then twenty sets of (C, k, a, b, τ), which represents uncertain annual wind loads for 20 years, are randomly generated to calculate the probabilistic fatigue damage. The 49.5 % reliability is obtained at the DDO optimum design obtained in Chapter 4, indicating that the probability of failure is 50.5 %, as expected, for DDO design and RBDO is necessary to further improve the reliability of the wind turbine drivetrain. To this end, the sampling-based reliability analysis is carried out to evaluate the probability of failure for each design using the Monte Carlo Simulation (MCS) method. However, use of a large number of MCS sample points required leads to a large number of contact fatigue damage evaluations using the 10-minute multibody drivetrain dynamics simulation, resulting in the RBDO calculation process being very computational intensive.

In order to overcome the computational difficulty resulting from the use of high-fidelity wind turbine drivetrain dynamics simulation, intermediate surrogate models are created once prior to the RBDO process using the dynamic kriging method and used throughout the entire RBDO iteration process. The area of the intermediate window chosen for generating the surrogate model covers approximately one ninth of the entire design variable domain. It is demonstrated that the RBDO optimum obtained ensures the target 97.725 % reliability (two sigma quality level) by only 1.4 % increase in the total weight from the baseline design with 8.3 % reliability. This result clearly indicates the importance of incorporating the tip relief as a design variable that prevents larger increase in the face width causing an increase in weight. This, however, does not mean that a larger tip relief is always preferred since an optimum tip relief amount depends on stochastic wind loads and an optimum tip relief cannot be found deterministically. Furthermore, accuracy of the RBDO optimum obtained using the intermediate surrogate models is justified by the reliability analysis at the RBDO optimum using the local surrogate models. It is demonstrated that the integrated design optimization procedure developed in this study enables the cost effective and reliable design of wind turbines drivetrains.

7.2 Future Work

There are several topics that would be recommended for further study to address the design optimization of wind turbine drivetrains and these topics are summarized as follows:

1. In this study, the time-domain rotor blade speed and the input shaft toque under wind loads are predicted using NREL FAST software, in which a drivetrain is modeled by a simplified lumped mass model. To ensure the consistency between the simplified drivetrain model used in the aerodynamics simulation of rotor blades and the high-fidelity model used in the gear tooth contact fatigue damage evaluation, a coupled multi-physics simulation capability that integrates the high-fidelity computational fluid dynamics (CFD) simulation for rotor blades and the multibody dynamics simulation for drivetrains would be pursued. A co-simulation technique proposed in the literature [108] would be one of the approaches that can be applied to the numerical procedure developed in this study.
2. While gear manufacturing uncertainties associated with the face width as well as the tip relief are considered in this study, the axial misalignment of a gear shaft alters the contact pressure distribution over the gear tooth, causing a significant impact on the contact fatigue life. That is, uncertainty associated with an assembly error would also be considered in RBDO to prevent unexpected failure due to gear assembly errors. Consideration of an axial misalignment requires developing a variable contact stiffness model for misaligned teeth in contact. Furthermore, an axial misalignment has a significant impact on the gear transmission error.
3. Deflection of the overhung main shaft of wind turbines alters the gear mesh phasing in the planetary gear. In particular, bending deflection of the shaft causes a misalignment of gear teeth in contact and the tooth contact pressure distribution may also be altered. Such a structural deformation of wind turbine components should be considered in the future work.
4. Rotor blade pitch control is crucial for achieving high energy production efficiency as well as preventing rotor blades from damages under stochastic wind loads. While an ideal region-3 speed control model is utilized in this study, more study is needed in the

future to shed light on the effect of the pitch control design and parameters on the drivetrain fatigue damages.

APPENDIX

A. The Probability Density Functions

The probability density functions (PDFs) of *C*, *k*, *a*, *b*, and τ are identified as follows:

$$f_c(x) = \frac{\exp\left[\frac{\ln(x) - 1.97164}{0.102395}\right]}{0.102395x\left[1+\exp\left(\frac{\ln(x) - 1.97164}{0.102395}\right)\right]^2} \quad \text{(A1)}$$

$$f_k(x) = \frac{1}{0.253686\sqrt{2\pi}}\exp\left[\frac{-(x-2.19127)^2}{0.128713}\right] \quad \text{(A2)}$$

$$f_a(x) = 1.188768\frac{(0.742993+0.082675x)^{-15.378745}}{\exp[(0.742993+0.082675x)]^{-14.378745}} \quad \text{(A3)}$$

$$f_b(x) = \frac{4.14407}{0.314799}\left(\frac{x}{0.314799}\right)^{3.14407}\exp\left[-\left(\frac{x}{0.314799}\right)^{4.14407}\right] \quad \text{(A4)}$$

$$f_\tau(x) = 0.0954368^{-1}\exp\left(\frac{x-0.552571}{0.0954368}\right)\exp\left[-\exp\left(\frac{x-0.552571}{0.0954368}\right)\right] \quad \text{(A5)}$$

B. 750kW GRC Wind Turbine Specifications

Specification of 750kW GRC wind turbine used in this thesis is summarized in Appendix B. The rotor blade properties are given in Table B.1 through B.3, while properties of the tower are provided in Table B.4 through B.6. These data are used for creating the wind turbine model using NREL FAST.

Table B.1 Twist and chord distribution for the GRC blade [97]

Station	Twist wrt Hub	Chord length	Comments
(m)	(deg)	(mm)	
0.00		1330.00	Large Calipers
3.66	16.00	1845.00	
4.88	18.10	2155.00	
6.10	17.20	2265.00	
7.01	14.70	2205.00	
8.23	12.30	2135.00	
10.06	10.50	2075.00	
10.06	9.00	1984.00	Medium Calipers
10.97	7.80	1909.00	
11.89	7.10	1824.00	
12.80	6.10	1747.00	
13.72	5.20	1667.00	
14.63	4.50	1575.00	
15.54	3.80	1493.00	
16.46	2.90	1389.00	
17.37	2.40	1286.00	
18.29	2.00	1187.50	
19.20	1.30	1156.00	
20.07	1.10	989.00	
20.07	1.10	916.00	
20.80	0.60	834.00	

Table B.1 Continued

20.80	0.80	873.00	Small Calipers
21.72	0.30	752.00	
22.63	-0.70	640.00	

Table B.2 GRC blade structural parameters [97]

Section number	Normalized section location	Mass/length (kg/m)	Flap stiffness (N-m2)	Lag stiffness (N-m2)
1	0.000	1427.29	3.74×10^9	3.74×10^9
2	0.021	200.79	6.12×10^8	6.12×10^8
3	0.053	205.39	5.36×10^8	4.47×10^8
4	0.105	213.15	4.09×10^8	4.09×10^8
5	0.158	221.05	2.82×10^8	3.71×10^8
6	0.211	229.08	1.55×10^8	3.33×10^8
7	0.263	213.27	1.32×10^8	2.89×10^8
8	0.316	196.96	1.08×10^8	2.45×10^8
9	0.368	180.18	8.45×10^7	2.02×10^8
10	0.421	162.91	6.10×10^7	1.58×10^8
11	0.474	145.16	3.77×10^7	1.14×10^8
12	0.526	129.29	3.13×10^7	9.57×10^7
13	0.579	113.00	2.49×10^7	7.75×10^7
14	0.632	96.28	1.84×10^7	5.94×10^7
15	0.684	79.13	1.18×10^7	4.12×10^7
16	0.737	61.56	5.18×10^6	2.31×10^7
17	0.789	52.33	4.28×10^6	1.88×10^7
18	0.842	42.87	3.31×10^6	1.46×10^7
19	0.895	33.18	2.27×10^6	1.03×10^7
20	0.947	23.27	1.18×10^6	6.03×10^6
21	1.000	13.13	6.83×10^4	1.77×10^6

Table B.3 Polynomial approximations of the mode shapes for GRC blade [97]

Mode	Frequency(Hz)	Polynomial terms ---------X^2+---------X^3+---------X^4+---------X^5+---------X^6				
1st flap	1.7217	0.02395	2.2453	-4.1649	5.1454	-2.2498
1st Lag	2.4098	0.69226	1.2286	-2.4026	2.5294	-1.0477
2nd Flap	4.8427	-1.92770	10.168	-34.565	46.353	-19.029

Table B.4 GRC tower dimensions [97]

Section	Distance from tower base	Outside diameter	Wall thickness
	(m)	(m)	(m)
1	0.000	3.026	0.019
2	5.361	2.931	0.019
3	10.723	2.866	0.016
4	16.084	2.853	0.016
5	21.446	2.694	0.016
6	26.807	2.470	0.013
7	32.169	2.278	0.013
8	37.530	2.046	0.013
9	42.891	1.893	0.013
10	48.253	1.740	0.013
11	53.614	1.646	0.013

Table B.5 GRC tower structural properties [97]

Station	Normalized section location	mass	EI	GJ	EA	Iy,Iz
		Kg/m	Nm2	Nm2	GN	Kg-m
1	0.000	1.404×10^{3}	4.206×10^{10}	3.235×10^{10}	3.721×10^{1}	1.586×10^{3}
2	0.098	1.359×10^{3}	3.820×10^{10}	2.938×10^{10}	3.604×10^{1}	1.441×10^{3}
3	0.196	1.109×10^{3}	2.985×10^{10}	2.296×10^{10}	2.939×10^{1}	1.126×10^{3}
4	0.293	1.104×10^{3}	2.945×10^{10}	2.265×10^{10}	2.926×10^{1}	1.111×10^{3}
5	0.391	1.042×10^{3}	2.476×10^{10}	1.905×10^{10}	2.762×10^{1}	9.340×10^{2}
6	0.489	7.647×10^{2}	1.530×10^{10}	1.177×10^{10}	2.027×10^{1}	5.772×10^{2}
7	0.587	7.051×10^{2}	1.200×10^{10}	9.227×10^{9}	1.869×10^{1}	4.524×10^{2}
8	0.685	6.328×10^{2}	8.670×10^{9}	6.669×10^{9}	1.678×10^{1}	3.270×10^{2}
9	0.783	5.852×10^{2}	6.857×10^{9}	5.275×10^{9}	1.551×10^{1}	2.586×10^{2}
10	0.880	5.377×10^{2}	5.319×10^{9}	4.092×10^{9}	1.426×10^{1}	2.006×10^{2}
11	0.978	5.083×10^{2}	4.493×10^{9}	3.456×10^{9}	1.348×10^{1}	1.695×10^{2}

Table B.6 Polynomial approximations of the mode shapes for GRC tower [97]

Mode	Frequency(Hz)	Polynomial terms				
		---------X2+	---------X3+	---------X4+	---------X5+	---------X6
1st side to side	0.4673	1.1445	-0.5231	0.0140	1.0153	-0.6507
1st fore-aft	0.4719	1.1562	-0.5406	0.0423	0.9883	-0.6462
2nd side to side	2.4537	32.4280	-50.238	79.921	-90.890	29.779
2nd fore-aft	2.9071	78.7820	-123.44	192.26	-232.90	86.292

C. Gear Material Properties

Material properties of gears for 750kW GRC wind turbine drivetrain model used in the pitting fatigue calculations are summarized in Appendix C.

Table C.1. Mechanical parameters of 18CrNiMo7-6

E(Mpa)	2.1×10^5
G(Mpa)	0.8×10^5
v	0.3
S_u(Mpa)	1172
σ_y(Mpa)	835
μ	0.04

Table C.2 Fatigue parameters of 18CrNiMo7-6.

C_p	4.87×10^{-16}
m	3.05
$\sigma_f^{'}$ (Mpa)	3470
$\tau_f^{'}$ (Mpa)	2499
b	-0.085
k_t	3
η	0.7
ε	0.11
Hv (HV)	720

Table C.3 Chemical composition of 18CrNiMo7-6.

C(%)	0.150-0.210
Si(%)	0.400
Mn(%)	0.500-0.900
P(%)	0.025
S(%)	0.035
Cr(%)	1.500-1.800
Mo(%)	0.250-0.350
Ni(%)	1.400-1.700

REFERENCES

1. Aydin, E., 2013, "Determination of Best Drive Train Technology for Future Onshore Wind Turbines as a Function of the Output Power", Master Thesis, Eindhoven Technical University.

2. Sheng, S., McDade, M., and Errichello, R., 2011,"Wind Turbine Gearbox Failure Modes-A Brief", *Proceedings of ASME/STLE 2011 International Joint Tribology Conference,* Los Angeles, California, USA

3. Errichello, R. and Muller, J., 2012,"Gearbox Reliability Collaborative Gearbox 1 Failure Analysis Report", *NREL/SR-5000-53062*.

4. Errichello, R., 2000, "Wind Turbine Gearbox Failures", *GEARTECH*.

5. Tallian, T.E., 1983, "Rolling Contact Fatigue", *SKF Ball Bearing Journal*, Vol.217, pp.5-13.

6. Errichello, R. and Muller, J., 2012, "Gearbox Reliability Collaborative Gearbox 1 Failure Analysis Report", *NREL/SR-500-53062*.

7. Milburn, A., 2011, "Wind Turbine Gearbox Wear and Failure Modes and Detection Methods", *NREL Wind Turbine Condition Monitoring Workshop*.

8. Barone, S., Borgianni, L., and Forte, P., 2004, "Evaluation of the Effect of Misalignment and Profile Modification in Face Gear Drive by a Finite Element Meshing Simulation", *ASME Mechanical Design,* Vol. 126, pp. 916- 924.

9. Nejad, A.R., and Moan, T., 2012, "Effect of Geometrical Imperfections of Gears in Large Offshore Wind Turbine Gear Trains: 0.6-10 MW Case Studies", *Proceedings of The Europe Wind Energy Association Conference 2012*, Copenhagen, Denmark.

10. Guo, Y., Bergua, R., Dam, J.V., Jove, J., and Campbell, J., 2015, "Improving Wind Turbine Drivetrain Designs to Minimize the Impacts of Non-torque Loads", *Wind Energy,* Vol. 18, pp. 2199-2222.

11. Choi, Y., and Liu, C.R., 2006, "Rolling Contact Fatigue Life of Finish Hard Machined Surfaces, Part 1. Model Development", *Wear,* Vol. 261, pp.485-491.

12. Keer, L.M., and Bryant, M.D., 1983, "A Pitting Model for Rolling Contact Fatigue", *ASME Tribology,* Vol.105, pp.198-205.

13. Glodez, G., Flasker, J., and Ren, Z., 1997, "A New Model for the Numerical Determination of Pitting Resistance of Gear Teeth Flanks", *Fatigue Fract. Engng. Mater. Struct*. Vol.20.No.1, pp.71-83.

14. Crossland, B., 1970, "The Effect of Pressure on the Fatigue of Metals", *Mechanical Behavior of Materials under Pressure*, pp.299-355.

15. Liu, J., and Zenner, H., 2003, "Fatigue Limit of Ductile Metals under Multiaxial Loading", *Biaxial/multiaxial fatigue and fracture*, Vol. 31. pp.147-164.

16. Dang, V.K., 1973, “Sur La Resistance a La Fatigue des Metaux”, *Science et techniques de L’Armement*. Vol. 47, pp. 647-722.

17. Choi, Y., and Liu, C.R., 2006, “Rolling Contact Fatigue Life of Finish Hard Machined Surfaces, Part 2. Experimental verification”, *Wear*, Vol. 261, pp.492-499.

18. Osman, T. and Velex, Ph., 2011, “A Model for the Simulation of the Interactions between Dynamic Tooth Loads and Contact Fatigue in Spur Gears”, *Tribology International*, Vol. 46, pp.84-96.

19. Choi, Y., and Liu, C.R., 2006, “Rolling Contact Fatigue Life of Finish Hard Machined Surfaces”, *Wear*, Vol. 261, pp.485-491.

20. Jiang, B., Zheng, X. and Wang, M., 1993, “Calculation for Rolling Contact Fatigue Life and Strength of Case-Hardened Gear Materials by Computer”, *Journal of Testing and Evaluation*, Vol. 21, pp.9-13.

21. Dong, W., Xing, Y., Moan, T. and Gao, Z., 2013, “Time Domain-based Gear Contact Fatigue Analysis of A Wind Turbine Drivetrain under Dynamic Conditions”, *International Journal of Fatigue*, Vol. 48, pp.133-146.

22. Ozguven, H. N. and Houser, D. R., 1988, "Mathematical Models Used in Gear Dynamics - A Review", *Journal of Sound and Vibration*, Vol. 121, pp. 383-411.

23. Wang, J., Li, R., Peng, X., 2003, “Survey of Nonlinear Vibration of Gear Transmission Systems”, *ASME Applied Mechanics Review*, Vol. 56, pp. 309-329.

24. Kahraman, A., 1994, “Planetary Gear Train Dynamics”, *ASME Journal of Mechanical Design*, Vol. 116, pp. 71-720.

25. Haug, E. J., 1989, *Computer Aided Kinematics and Dynamics of Mechanical Systems*, Boston: Ally and Bacon.

26. Shabana, A. A., 2010, *Computational Dynamics*, Third Edition, Wiley.

27. Cardona, A., 1997, “Three-Dimensional Gears Modeling in Multibody Systems Analysis”, *International Journal of Numerical Methods in Engineering*, Vol. 40, pp. 357-381.

28. Palermo, A., Mundo, D., Hadjit, R. and Desmet, W, 2013, “Multibody Element for Spur and Helical Gear Meshing Based on Detailed Three-Dimensional Contact Calculations”, *Mechanism and Machine Theory*, Vol. 62, pp. 13-30.

29. Ebrahimi, S. and Eberhard, P., 2006, “Rigid-Elastic Modeling of Meshing Gear Wheels in Multibody Systems”, *Multibody System Dynamics*, Vol.16, pp. 55-71.

30. Lee, C., H., Bae, D., S. and Song, J. S., 2012, “Multibody Approach of Gear Transmission Error Dynamics”, *Proceedings of Asian Conference on Multibody Dynamics*, Shanghai, China.

31. Ziegler, P. and Eberhard, P., 2009, “An Elastic Multibody Model for the Simulation of Impacts on Gear Wheels”, *Proceedings of ECCOMAS Thematic Conference on Multibody Dynamics*, Warsaw, Poland.

32. Vijayakar, S., 1991, "A Combined Surface Integral and Finite Element Solution for a Three-Dimensional Contact Problem", *International Journal for Numerical Methods in Engineering*, Vol.31, pp. 525-545.

33. Parker, R. G., Agashe, V. and Vijayakar, S. M, 2000, "Dynamic Response of a Planetary Gear System Using a Finite Element/Contact Mechanics Model", *ASME Journal of Mechanical Design*, Vol. 122, pp. 305-311.

34. Peeters, J.L.M., Vandepitte, D. and Sas, P., 2005, "Analysis of Internal Drive Train Dynamics in a Wind Turbine", *Wind Energy*, Vol. 9, pp. 141-161.

35. Oyague, F., 2009, "Gearbox Modeling and Load Simulation of a Baseline 750-kW Wind Turbine Using State-of-the-Art Simulation Code", *NREL/TP-500-41160*.

36. Qin, D., Wang, J. and Lin, T.C., 2009, "Flexible Multibody Dynamics Modeling of a Horizontal Wind Turbine Drivetrain System", *ASME Journal of Computational and Nonlinear Dynamics*, Vol. 131, pp. 1-8.

37. Helsen, J., Vanhollebeke, F., Marrantb, B., Vandepitte, D., Desmet, W., 2011, "Multibody Modelling of Varying Complexity for Modal Behaviour Analysis of Wind Turbine Gearboxes", *Renewable Energy*, Vol. 36, pp. 3098–3113.

38. Vanhollebeke, F., Peeters, P., Helsen, J., Lorenzo, E.D., Manzato, S., Peeters, J., Vandepitte, D. and Desmet, W., 2015, "Large Scale Validation of a Flexible Multibody Wind Turbine Gearbox Model", *ASME Journal of Computational and Nonlinear Dynamics*, Vol. 10, pp. 1-12.

39. Alemayehu, F.M. and Osire, S.E., 2015, "Probabilistic Performance of Helical Compound Planetary System in Wind Turbine", *ASME Journal of Computational and Nonlinear Dynamics*, Vol. 10, pp. 1-12.

40. Litvin, F. L. and Fuentes, A, 2004, *Gear Geometry and Applied Theory*, Second Edition, Cambridge University Press.

41. Shabana, A. A., Zaazaa, K. E. and Sugiyama, H., 2008, *Railroad Vehicle Dynamics: Computational Approach*, CRC Press.

42. Vanderplaats, G.N., Chen, X. and Zhang, N.-T., 1988, "Gear Optimization", *NASA CR-4201*, pp. 1-60.

43. Spitas, V., and Spitas, C., 2007, "Optimizing Involute Gear Design for Maximum Bending Strength and Equivalent Pitting Resistance", *Proc. IMechE*. Vol.221, pp. 479-488.

44. Sansalvador, R.L., and Jauregui, J.C., 1993, "Practical Optimization of Helical Gears Using Computer Software", *Gear Technology*, pp.16-21.

45. Kapelevich, A., and Shekhtman, Y., 2009,"Gear Tooth Fillet Profile Optimization", *Gear Solutions*, pp.63-69.

46. Barbieri, M., Scagliarini, G., Bonori, Giorgio., Pellicano, Francesco., and Bertccchi, Gabriele., 2008, "Optimization Methods for Spur Gear Dynamics", *Proceedings of EUROMECH Nonlinear Dynamics Conference*, Saint Petersburg, Russia.

47. Maatar, M., and Velex, P., 1997, "Quasi-Static and Dynamic Analysis of Narrow-Faced Helical Gears with Profile and Lead Modifications", *ASME Mechanical Design*, Vol.119, pp.474-480.

48. Velex, P., Bruyere, J., and Houser, D.R., 2011, "Some Analytical Results on Transmission Errors in Narrow-Faced Spur and Helical Gears: Influence of Profile Modifications", *ASME Journal of Mechanical Design*.Vol.133, pp.1-11.

49. Sundaresan, S., Ishii, K., and Houser, D.R., 1991, "A Procedure Using Manufacturing Variance to Design Gears with Minimum Transmission Error", *ASME Journal of Mechanical Design*, Vol.113, pp.318-324.

50. Yu, C.J., 1998, "Design Optimization for Robustness using Quadrature Factorial Models", *Engineering Optimization*. Vol.30, pp. 203-225.

51. Ghribi, D., Bruyere, J., Velex, P, Octrue, M., and Mohamed, H., 2012, "Robust Optimization of Gear Tooth Modifications Using a Genetic Algorithm", *Springer, Condition Monitoring of Machinery in Non-Stationary Operations*, pp. 589-597.

52. Madhusekhar, D., and Madhava Reddy, K., 2014, "Reliability Based Optimum Design of a Gear Box", *Int. Journal of Engineering Research and Applications*, Vol.4, Issue 10, pp. 1-8.

53. Tu, J. and Choi, K.K., 1999, "A New Study on Reliability Based Design Optimization," *ASME Journal of Mechanical Design*, Vol. 121, No. 4, pp. 557-564.

54. Youn, B.D. and Choi, K.K., 2004, "A New Response Surface Methodology for Reliability-Based Design Optimization," *Computers and Structures*, Vol. 82, Iss. 2-3, pp. 241-256.

55. Lee, I., Choi, K.K., Du, L., and Gorsich, D., 2008, "Dimension Reduction Method for Reliability-Based Robust Design Optimization," *Special Issue of Computer & Structures: Structural and Multidisciplinary Optimization*, Vol. 86, pp. 1550–1562.

56. Noh, Y., Choi, K.K., Lee, I., and Gorsich, D., 2011, "Reliability-based Design Optimization with Confidence Level for Non-Gaussian Distributions Using Bootstrap Method," *ASME Journal of Mechanical Design*, Vol. 133. 1-12.

57. Lee, I., Choi, K.K., and Zhao, L., 2011, "Sampling-Based RBDO Using the Stochastic Sensitivity Analysis and Dynamic Kriging Method," *Structural and Multidisciplinary Optimization*, Vol. 44, pp. 299-317.

58. Tu, J., Choi, K.K., and Park, Y.H., 2001, "Design Potential Method for Robust System Parameter Design," *AIAA Journal*, Vol. 39, No. 4, pp. 667-677.

59. Hohenbichler, M., and Rackwitz, R., 1988, "Improvement of Second-Order Reliability Estimates by Importance Sampling", *Journal of Engineering Mechanics*, Vol.114, No.12, pp.2195-2199.

60. Picheny., V., 2009, "Improving Accuracy and Compensating for Uncertainty in Surrogate Modeling", PhD Thesis, University of Florida.

61. Faravelli, L., 1989, "Response Surface Approach for Reliability Analysis", *Journal of Engineering Mechanics*, Vol.115, pp. 2763-2781.

62. Smola, A.J., and Schölkopf, B., 2004, "A Tutorial on Support Vector Regression", *Statistics and Computing*, Vol.14, pp.199-222.

63. Hurtado, J.E., and Alvarez. D.A., 2001, "Neural-Network-Based Reliability Analysis: A Comparative Study", *Computer Methods in Applied Mechanics and Engineering*, Vol.191, pp.113-132.

64. Park, J., and Sandberg, I., 1993, "Approximation and Radial-Basis-Function Networks", *Neural Computation*, Vol. 5, pp. 305-316.

65. Janusevskis, J., and Riche, R.L., 2013, "Simultaneous Kriging-Based Estimation and Optimization of Mean Response", *Journal of Global Optimization*, Vol. 55, pp.313-336.

66. Hu, W., Choi, K.K., Cho, Hyunkyoo., Gaul, N.J., and Zhupanska, O.I., 2015, "Reliability Based Design Optimization of Wind Turbine Blades for Fatigue Life under Wind Load Uncertainty", *11th World Congress on Structure and Multidisciplinary Optimization*. Sydney, Australia.

67. Piegl, L. A. and Tiller, W., 1996, *The NURBS Book*, Springer.

68. Shikin, E. V. and Plis, A., I., 1995, *Handbook on Splines for the User*, CRC Press.

69. Kin, V., 1994, "Computerized Analysis of Gear Meshing Based on Coordinate Measurement Data", *ASME Journal of Mechanical Design*, Vol. 116, pp. 738-744.

70. Zhang, Y., Litvin, F. L., Maruyama, N., Takeda, R. and Sugimoto, M, 1994, "Computerized Analysis of Meshing and Contact of Gear Real Tooth Surfaces", *ASME Journal of Mechanical Design*, Vol. 116, pp. 738-744.

71. Sugiyama, H., Yada, M., Yamamoto, H., Kurihara, J., Ohbayashi, H., Shimokawa, Y., Mizuno, M. and Tanimoto, M., 2013, "Wheel and Rail Profile Wear on Small Radius Curved Track and its Effect on Vehicle Curving Performance: Measurement and Simulation", *International Journal of Railway Technology*, Vol. 4, pp. 85-98.

72. Sugiyama, H., Sekiguchi, T., Matsumura, R., Yamashita, S. and Suda, Y., 2012, "Wheel/Rail Contact Dynamics in Turnout Negotiations with Combined Nodal and Non-Conformal Contact Approach", *Multibody System Dynamics*, Vol.27, pp. 55-74.

73. Li, H., Terao, A. and Sugiyama, H., 2015, "Application of Tabular Contact Search Method to Multibody Gear Dynamics Simulation with Tooth Surface Imperfections", *IMechE Journal of Multibody Dynamics*, Vol.229, pp. 274-290.

74. Sugiyama, H. and Suda, Y., 2009, "Wheel/Rail Two-Point Contact Geometry with Back-of-Flange Contact", *ASME Journal of Computational and Nonlinear Dynamics*, Vol.4, pp. 1-6.

75. Cornell, R. W., 1981, "Compliance and Stress Intensity of Spur Gear Teeth", *ASME Journal of Mechanical Design*, Vol. 103, pp. 447-459.

76. Tavakoli, M. S. And Houser, D. R, 1986, "Optimum Profile Modifications for the Minimization of Static Transmission Errors of Spur Gears", *ASME Journal of Mechanisms, Transmissions, and Automation in Design*, Vol. 108, pp. 86-94.

77. Sainsot, P. and Velex, P., 2004, "Contribution of Gear Body to Tooth Deflections- A New Bi-dimensional Analytical Formula", *ASME Journal of Mechanical Design*, Vol. 126, pp. 748-752.

78. Mohammadpour, M., Theodossiades, S. and Rahnejat, H., 2014, "Multiphysics Investigations on the Dynamics of Differential Hypoid Gears", *ASME Journal of Vibration and Acoustics*, Vol. 136, pp.1-3.

79. Karagiannis, I., Theodossiades, S. and Rahnejat, H., 2012, "On the Dynamics of Lubricated Hypoid Gears", *Mechanism and Machine Theory*, Vol. 48, pp. 94-120.

80. S. Sheng, 2012 Wind Turbine Gearbox Condition Monitoring Round Robin Study, *NREL/TP-5000-54530*.

81. Houser, D.R., Bolze, V.M. and Graber, J.M.,1996, "A Comparison of Predicted and Measured Dynamic and Static Transmission Error for Spur and Helical Gear Sets", *SEM 14th International Modal Analysis Conference*, Dearborn, MI, USA.

82. Guo, Y.,Keller, J., and LaCava, W., 2012, "Combined Effects of Gravity, Bending Moment, Bearing Clearance, and Input Torque on Wind Turbine Planetary Gear Load Sharing", *NREL/CP-5000-55968*.

83. Guo, Y., LaCava, W., Xing, Y., and Moan, T., 2012, "Determining Wind Turbine Gearbox Model Complexity Using Measurement Validation and Cost Comparison", *NREL/CP-5000-54545*.

84. Veers, P.S. and Winterstein, S.R., 1998, "Application of Measured Loads to Wind Turbine Fatigue and Reliability Analysis", *ASME Journal of Solar Energy Engineering*, Vol. 120, pp. 233-239.

85. Hu, W., Choi, K.K., Zhupanska, O. and Buchholz, J., 2016, "Integrating Variable Wind Load, Aerodynamic, and Structural Analyses towards Accurate Fatigue Life Prediction in Composite Wind Turbine Blades", *Structural and Multidisciplinary Optimization*, Vol.53, pp.375-394.

86. Hu, W., Choi, K.K., Gaul, N. J., Cho, H., Zhupanska, O.I., 2012, "Reliability Analysis of Wind Turbine Blades for Fatigue Life under Wind Load Uncertainty", *Proceedings of 12th AIAA Aviation Technology, Integration, and Operations (ATIO) Conference*, Indiana, USA.

87. Budynas, R., and Nisbett, K., 2008, *Shigley's Mechanical Engineering Design*, 9th edition, McGraw-Hill.

88. Kato, M., Deng, G., Inoue, K. and Takatsu, N., 1993, "Evaluation of the Strength of Carburized Spur Gear Teeth Based on Fracture Mechanics", *Bulletin of the Japan Society of Mechanical Engineers, Series C*, Vol.36, pp. 233-234.

89. Newman, C.J., 1992, "Small-Crack Test Method", *ASTM STP 1149*, pp. 6-33.

90. Straffelini, G., Molinari, A. and Marcupuscas, T., 2000, "Identification of Rolling-Sliding Damage Mechanisms in Porous Alloys", *Metallurgical and Materials Transactions A*, Vol. 31, pp. 3091-3099.

91. Li, H., Sugiyama, H., Cho, H., Choi, K.K., and Gaul, N.J., 2016, "Numerical Procedure for Design Optimization of Wind Turbine Drivetrain Using Multibody Gear Dynamics Simulation Considering Wind Load Uncertainty", *Proceedings of the ASME 2016 IDETC & CIE Conference*, Charlotte, DETC2016-59654.

92. Jonkman, B.J., 2009, "TurbSim User's Guide", *Technical Report NREL/TP-500-46198*.

93. Jonkman, J.M. and Buhl, M.L., 2005, "FAST User's Guide", *Technical Report NREL/TP-500-38230*.

94. Lesmerises, A., and Crowley, D., 2013, "Effect of Different Workscope Strategies on Wind Turbine Gearbox Life Cycle Repair Costs," *International Journal of Prognostics and Health Management*, Vol.17, pp.1-7.

95. Melchers, R.E., 1999, *Structural Reliability Analysis and Prediction*, Wiley.

96. Choi, K.K., and Gaul, N.J., 2016, "The RAMDO Software",www.ramdosolutions.com

97. Girsang, I.P., Dhupia, J. S., Muljadi, E., Singh, M., and Pao, L.Y., 2014, "Gearbox and Drivetrain Models to Study Dynamic Effects of Modern Wind Turbines", *IEEE Transaction of Industry Applications*, Vol. 50, pp. 3777- 3786.

98. Bir, G.S. and Oyague, F., 2007, "Estimation of Blade and Tower Properties for the Gearbox Research Collaborative Wind Turbine", *NREL/TP-500-42250*.

99. Muljadi, E. and Butterfield, C.P., 2000, "Pitch-Controlled Variable-Speed Wind Turbine Generation," *Technical Report NREL/CP-500-27143*.

100. International Organization for Standardization, 2005, "Wind Turbines Part 1: Design Requirements", *IEC 61400-1:2005*, ISO Geneva, Switzerland.

101. Hu, W., 2015, "Reliability Based Design Optimization of Composite Wind Turbine Blades for Fatigue Life under Wind Load Uncertainty", Ph.D Thesis, University of Iowa.

102. Zhao, L., Choi, K.K., and Lee, I., 2011, "Metamodeling Method Using Dynamic Kriging for Design Optimization", *AIAA Journal*, Vol. 49, No.9. pp. 2034-2046.

103. Lee, I., Choi, K.K., Noh, Y., Zhao, L., and Gorsich, D., 2010, "Sampling-Based RBDO Using the Dynamic Kriging (D-Kriging) Method and Stochastic Sensitivity Analysis", *13th AIAA/ISSMO Multidisciplinary Analysis and Optimization Conference*, Fort Worth, Texas.

104.Hazelton, J.L., 2003, "Gear Manufacturers Face Challenges in Growing Wind Energy Industry", *GEAR TECHNOLOGY*.

105.American National Standard, "Gear Classification and Inspection Handbook - Tolerances and Measuring Methods for Unassembled Spur and Helical Gears", *AGMA 2000-A88*.

106.UTS Integrated Gear Software, "External Gear Set Tip Relief-Full Depth Teeth", *Program 60-1111*.

107.Sen, O., Davis, S., Jacobs, G., and Udaykumar, H.S., 2015, "Evaluation of Convergence Behavior of Metamodeling Techniques for Bridging Scales in Multi-scale Multimaterial Simulation", *Journal of Computational Physics*, Vol. 294, pp. 585-604.

108.Li, Y., Castro, A.M., Sinokrot, T., Prescott, W., and Carrica, P.M., 2015, "Coupled Multi-body Dynamics and CFD for Wind Turbine Simulation Including Explicit Wind Turbulence", *Renewable Energy*, Vol. 76, pp. 338- 361.